T.R.
GEBZE TECHNICAL UNIVERSITY
INSTITUTE OF BIOTECHNOLOGY

DEVELOPMENT OF A MICROFLUIDIC CHIP TO SEPARATE CIRCULATING TUMOR CELLS FROM HUMAN BLOOD

CIGDEM BOZ
A THESIS SUBMITTED FOR THE DEGREE OF
MASTER OF SCIENCE
DEPARTMENT OF BIOTECHNOLOGY

GEBZE
2020

T.R.

GEBZE TECHNICAL UNIVERSITY

INSTITUTE OF BIOTECHNOLOGY

DEVELOPMENT OF A MICROFLUIDIC CHIP TO SEPARATE CIRCULATING TUMOR CELLS FROM HUMAN BLOOD

CIGDEM BOZ

A THESIS SUBMITTED FOR THE DEGREE OF

MASTER OF SCIENCE

DEPARTMENT OF BIOTECHNOLOGY

THESIS SUPERVISOR

ASST. PROF. MUHAMMED ENES ORUC

GEBZE

2020

T.C.
GEBZE TEKNİK ÜNİVERSİTESİ
BİYOTEKNOLOJİ ENSTİTÜSÜ

DOLAŞIMDAKİ TÜMÖR HÜCRELERİNİN İNSAN KANINDAN AYRIŞTIRILMASI İÇİN MİKROAKIŞKAN ÇİP GELİŞTİRİLMESİ

ÇİĞDEM BOZ

YÜKSEK LİSANS TEZİ
BİYOTEKNOLOJİ ANABİLİM DALI

DANIŞMANI
DR. ÖĞR. ÜYESİ MUHAMMED ENES ORUÇ

GEBZE
2020

GEBZE TEKNİK ÜNİVERSİTESİ	**YÜKSEK LİSANS JÜRİ ONAY FORMU**

GTÜ Biyoteknoloji Enstitüsü Yönetim Kurulu", nun 23/07/2020 tarih ve 2020/12-02 sayılı kararıyla oluşturulan jüri tarafından 24/07/2020 tarihinde tez savunma sınavı yapılan Çiğdem Boz'un tez çalışması Biyoteknoloji Enstitüsü YÜKSEK LİSANS tezi olarak kabul edilmiştir.

JÜRİ

ÜYE
(TEZ DANIŞMANI) : Dr. Öğr. Üyesi Muhammed Enes ORUÇ

ÜYE : Prof. Dr. Numan Akdoğan

ÜYE : Dr.Öğr.Üyesi Hüseyin ÜVET

ONAY

Gebze Teknik Üniversitesi Biyoteknoloji Enstitüsü Yönetim Kurulu", nun ……/……/…… tarih ve ……/…….. sayılı kararı.

İMZA/MÜHÜR

SUMMARY

The main goal of the thesis is to design and model microfluidic chips to effectively separate the Circulating Tumor Cells (CTCs) from other cells. CTCs are cells that arise from cancerous tumors, and they circulate in the blood vessels for a long time without any action, and all of a sudden, they can initiate tumor formation in other tissues. Their rareness in the blood makes their detection highly challenging. To this end, in this thesis, we used Computational Fluid Dynamics (CFD) simulation to optimize the channel geometry and flow dynamics to maximize the CTC separation. Understanding the control of the physical mechanism of particle trajectories at the microscale is essential. Therefore, in the first step, we tracked particle movement in straight channels under laminar flow to determine the channel cross-section dimensions. In the second step, we focused on the Archimedean spiral channels. The inertial forces, which are acting on particles, are strongly affected by flow rate, so we simulated particle movement at several Reynolds numbers. When the Reynolds number decreased, the drag force on the particles decreased. That situation led to a decrease in particle separation efficiency. The channel length was extended to overcome that loss, and the particles were exposed to the drag force for a more extended period to accrue efficient separation. When the Reynolds number increased in the simulations, drag forces dominated the lift forces. In those simulations, short channels were sufficient to perform the separation of target particles with the increase of inertial forces acting on the particles. Simulations were performed in the presence of sheath flow, and without sheath flow, following the results were compared. In the spiral channel simulations containing sheath flow, the particles focused on producing clusters. As a result, the target particles, representing CTCs separated from others with 100 % efficiency. However, in the sheathless flow simulations, the drag force acting on 1 and 3 μm particles was not sufficient by itself, all of these particles could not be directed, and that a decrease in the separation efficiency was observed. However, sheathless flow can be used effectively, as the particles do not prevent the target cells from being seen due to their small size.

Key Words: Circulating Tumor Cells (CTCs), Computational Fluid Dynamics (CFD),Microfluidics, Inertial focusing

ÖZET

Tezin temel amacı, Dolaşımdaki Tümör Hücrelerini (CTC'ler) diğer hücrelerden etkili bir şekilde ayırmak için mikroakışkan çipleri tasarlamak ve modellemektir. CTC'ler kanserli tümörlerden kaynaklanan hücrelerdir, bu hücreler kan damarlarında uzun süre herhangi bir etki yapmadan dolaşırlar ve aniden diğer dokularda tümör oluşumunu başlatabilirler. Kanda nadir bulunmaları, tespitlerini oldukça zorlaştırır. Bu amaçla, bu tezde, CTC ayrımını en üst düzeye çıkarmak için kanal geometrisini ve akış dinamiklerini optimize etmek için Hesaplamalı Akışkanlar Dinamiği (CFD) simülasyonunu kullandık. Mikro ölçekte parçacık yörüngelerinin fiziksel mekanizmasının kontrolünü anlamak çok önemlidir. Bu nedenle, ilk adımda, kanal kesit boyutlarını belirlemek için laminer akış altında düz kanallarda parçacık hareketini takip ettik. İkinci adımda Arşimet spiral kanallarına odaklandık. Parçacıklara etki eden atalet kuvvetleri akış hızından büyük ölçüde etkilenir, bu nedenle parçacık hareketinin birkaç Reynolds sayısında simülasyonunu gerçekleştirdik. Reynolds sayısı azaldığında, partiküller üzerindeki sürükleme kuvveti azaldı. Bu durum, partikül ayırma verimliliğinde azalttı. Bu kaybın üstesinden gelmek için kanal uzunluğu uzatıldı ve etkili bir ayırma sağlamak için parçacıklar, daha uzun süre sürükleme kuvvetine maruz bırakıldı. Simülasyonlarda Reynolds sayısı arttığında, partiküllere etki eden atalet kuvvetleri arttı ve hedef partiküllerin ayrılmasını gerçekleştirmek için kısa kanallar yeterliyoldu. Simülasyonlarda, kanal geometrisi ve akışkan akış hızı, partiküllerin yüksek verimlilikle ayrılmasında önemli bir role sahiptir. Simülasyonlar kılıf akışı varlığında ve kılıf akışı olmadan yapıldı, sonuçlar karşılaştırıldı. Kılıf akışını içeren spiral kanal simülasyonlarında, parçacıklar kümeler oluşturarak odaklandı. Sonuç olarak, CTC'leri temsil eden hedef parçacıklar % 100 verimlilikle diğerlerinden ayrıldı. Ancak kılıfsız akış simülasyonlarında 1 ve 3 μm partiküllere etki eden sürükleme kuvveti tek başına yeterli olmadı, bu partiküllerin hepsi yönlendirilemedi ve ayırma veriminde düşüş gözlendi. Küçük boyutlarından dolayı partiküller hedef hücrelerin görünmesini engellemediğinden kılıfsız akış etkin bir şekilde kullanılabilir.

Anahtar Kelimeler: Dolaşımdaki Tümör Hücreleri (CTC'ler), Hesaplamalı Akışkanlar Dinamiği (CFD) Mikroakışkanlar, Atalet odaklama

ACKNOWLEDGEMENTS

I would like to express my gratitude to my supervisor, Asst. Prof. Muhammed Enes ORUÇ, who shared his scientific knowledge with me, supported and encouraged me during this research.

I do not want to pass without saying my family's love in this process. My mother, Hayriye, and my father, Bekir, I would like to say I couldn't have accomplished all the things without you.

I want to thank my brother Mustafa and his wife Canan for supporting my education, and their smart daughter Kardelen, who took her book and studied with me. One day, Kardelen said to her mother, "My aunt is studying a lot." I would like yo tell you, Kardelen. Your aunt will study all her life.

My little brother, Emre, I want you to know that we love you very much and that I thank you very much for always being with me.

My friend, Morteza Vafadar supported and helped me during this research and İbrahim Nasuh Yıldıran shared his knowledge and advised me in this work. I want to say that I will never forget their support.

I would like to thank Aysel Gürbüz, Özlem Baltacı, Fadime Arık, Özlem Şentürk, Ayşe Türkan, Sonnur Erdem, Sevde Ömeroğlu and many of my friends, whose names I cannot count.

TABLE of CONTENTS

LIST of ABBREVIATIONS and ACRONYMS

Abbreviations and Acronyms		Explanations
Re	:	Reynolds number
$F_{inertia}$	:	Inertial Forces
$F_{viscous}$	:	Viscous Forces
ρ	:	Density
V	:	The characteristic velocity of the flow
μ	:	Viscosity
D_h	:	The hydraulic diameter of the channel
υ	:	The kinematic viscosity
A	:	The cross-sectional area of the flow
P	:	The wetted perimeter of the cross-section
h	:	Channel height
w	:	Channel width
Re_p	:	Particle Reynolds numbers
a	:	Particle diameter
F_L	:	Lift Forces
F_{WI}	:	Wall induced lift force
F_{SG}	:	Shear gradient lift force.
F_D	:	Secondary-flow drag force.
C_{WI}	:	Lift coefficient for the wall induced lift force.
U_{Max}	:	Maximum flow velocity
C_{SG}	:	Lift coefficient for the shear gradient lift force
F_D	:	Secondary-flow drag force.
U_{SF}	:	Secondary-flow velocity
π	:	Pi number
u	:	The velocity vector
p	:	Pressure
l	:	The unit tensor
K	:	The symmetric deformation tensor
F	:	Body force

T	:	Transpose
U_0	:	The inlet velocity vector
n	:	The outward normal.
p_0	:	The outlet pressure
v	:	The velocity of the particle
v_c	:	The particle velocity when striking the wall
v_0	:	Initial particle velocity
Q	:	The particle position
t	:	Time
t_0	:	Initial time
q_0	:	The initial particle position
m_p	:	The particle mass
F_g	:	Gravity force
F_{ext}	:	External Force
τ_p	:	The particle velocity response time
u_p	:	The velocity of the particle
ρ_p	:	The particle density
d_p	:	The particle diameter
r_p	:	The particle radius
D	:	The distance between the channel walls
s	:	The nondimensionalized distance from the particle to the first parallel boundary
I	:	The identity matrix.
F_{WC}	:	The wall correction force
M	:	The correction factor
$P(n)$	:	The projection operator onto the wall-normal
l_W	:	The diance from the center of the particle to the nearest wall.
Z	:	The aspect ratio
κ	:	The blockage ratio
L_f	:	Length of the channel
CTC	:	Circulating Tumor Cells
RBC	:	Red Blood Cell

WBC	:	White Blood Cell
DEP	:	Dielectrophoresis
CD	:	Compact Disc
DGM	:	Density Gradient Medium
DFF	:	Dean Flow Fractionation
CEA	:	Contraction–Expansion Array
MOFF	:	Multi-Orifice Flow Fractionation
PS-DVB	:	Polystyrene Divinylbenzene
2D	:	Two-Dimensional
3D	:	Three-Dimensional
CFD	:	Computational Fluid Cynamics
EpCAM	:	Epithelial Cellular Adhesion Molecule

LIST of FIGURES

1. INTRODUCTION

Circulating Tumor Cells (CTCs) are cells that arise from cancerous tumors, join the circulatory system, and migrate to distant organs. This phenomenon is defined as metastasis, which resulted in cancer spreading to one organ to others via blood [Gupta et al., 2006]. Ninety percent of cancer deaths are due to metastasis diseases [Dong et al., 2013]. The CTCs' lifetime can vary depending on the type of tumors of origin and the treatment which is applied. Even though the cancer tissue is surgically removed from a patient, a new cancer formation can be observed in the patient again after a few years. One of the reasons is that CTCs can circulate in the blood vessels for a long time without any action, and all of a sudden, they can initiate tumor formation in other tissues. As a result, although cancer in the primary tissue is purged, any CTC remains in the blood may cause tumor formation in the body again in the future.

CTCs are infrequent cells. Common blood cell types exist in tremendous numbers in blood by comparison with CTCs. On average, an adult human has 5 billion red blood cells (RBCs), 270 million platelets and, 7 million white blood cells (WBCs) per ml of blood [Dean L, 2005]. When we assume all CTCs comes from primary tumor tissue keep in the circulatory system, up to 200 CTCs can be collected from one ml of blood of an ordinary patient. That means, four or less of the 100000 cells are CTC in the blood. Their rareness in the blood makes their detection highly challenging.

1.1. Microfluidic Approaches for CTC Separation

Microfluidics is an engineering science that manipulates and controls the fluid at the microscale [Convery et al., 2019]. The sample volume could be in the range of microliters to picoliters in the networks of microchannels [Qin et al., 1998]. Microfluidic systems are used in many fields and offer users fast, practical, and accurate solutions. Particle detection, identification, and separation in fluids are essential for health. For health particle separation, identification from fluids is indispensable. For instance, Microfluidic systems are used in searching for contaminants in the fluids of food, cancer cells in the blood, and detecting pathogens [Fuchs et al., 2019]. When we consider the industry, the need for manipulation of even

a micro-scale particle increases over time. High purity processes are indispensable in the health field since even a small amount of the particles in many areas, such as chemical analyzes, medical diagnoses, and tissue engineering, can cause adverse effects [Brody et al., 1996].

Lots of microfluidic methods have been used worked out, for instance, magnetophoresis, acoustophoresis, dielectrophoresis (DEP) [Antfolk et al., 2017], [Yan, 2016]. However, the centrifugal effect is the most practical method when compared to others.

Employing a centrifugal effect in microfluidic platforms is a commonly used method for particle tracking and separation. The microfluidic platforms, using the centrifugal effect, are separated into two categories. The first one is the centrifugal microfluidic platforms. This category contains passive methods such as sedimentation, separating particles by using their physical properties and their immunoaffinity, or active processes such as dielectrophoresis and the magnetic field for particle tracking. The second category, defined as the inertial microfluidic platforms, utilizes the different structures of microchannel such as channels with sudden expansion-contraction arrays, producing centrifugation flow or spiral channels, generating secondary drag force [Al-Faqheri et al., 2017].

As mentioned, the first subcategory of the field of microfluidics is centrifugal microfluidics, which utilizes centrifugal forces on rotating platforms to drive fluids within fluidic networks. These rotating platforms in the form of a compact disc (CD) are designed to perform specific biological or chemical analyses on a standard benchtop. Centrifugal microfluidic platforms have low production costs, ease of manufacturability, high reliability, and portability [Salar et al., 2013]. These portable and extremely low-cost devices are used in laboratories that are resource-poor [Burger et al., 2012]. In particular, the most used blood separation method on centrifugal passive microfluidic platforms is density-based blood fractionation (sedimentation), which is the segregation of the plasma from the leftover portion of the blood cells. Because the sedimentation technique does not have enough precision for CTC separation after the sedimentation process has occurred, subsequent steps are needed to be completed, such as purified plasma decantation or extraction [Park et al., 2014].

The second centrifugal passive method for the separation of particles is settled on the particles' physical properties, which are geometry-based methods. Generally, in these methods, a diluted blood sample is used with magnetic beads. Cells in the blood are bound the magnetic beads. Since the magnetic forces of CTCs are higher than blood cells, more magnetic beads will be attached to CTCs. Due to the difference in the interaction of the magnetic beads with each cell kinds, different cell kinds will be separated from each other under a magnetic field. Although the separation efficiency is high, it is necessary to remove many pollutants while the magnetic beads are physically separated. That means that an extra step for the separation of contaminants is required. Unfortunately, this could lead to losing valuable CTC [Smith et al., 2016], [Yoo et al., 2016].

Immunoaffinity, the last centrifugal passive method, is can be expressed as the specific chemical affinity between an antibody, or antibody domain, and an antigen. In this way, only specifically targeted cells are captured by particular antigens/antibodies. For instance, a study is made by using magnetic beads with antibody-bound [Casavant et al., 2013]. The usage of antibody and magnetic beads at the same time makes it possible to isolate the targeted cells from heterogeneous mixtures. In most preferred sorting platforms, immunoaffinity is performed together with other sorting mechanisms, for instance, density gradient medium (DGM) [Park et al., 2014]. A fully automated centrifugal microfluidic platform was designed to isolate CTCs from blood samples, consisting of a blood chamber, a DGM chamber, a collection chamber, and a waste chamber. It is fully automated but complicated [Park et al., 2014].

Inertial microfluidics is the second subcategory of the area where the centrifugal effect is used. Inertial microfluidic platforms are classified as multi-hole microfluidics and spiral microfluidics. In general, when CTC isolation is made from high volume samples, inertial microfluidics is more preferred than centrifugal microfluidics.

Microfluidic platforms with non-straight channels have been widely investigated by Khademhosseini A. 2005; Di Carlo D et al., 2007, 2008; Lim E. J. et al. 2012; Bhagat, A. A. S. et al. 2008; Karabacak N. M. et al. 2014; Sun J. 2012; Chen H. 2018; for particle/cell separation. There are two approaches based on inertial focusing particle separation. These are using sheath flow or sheath-less flow for a spiral channel

for the separation of different size particles. For instance, Bhagat et al. (2008) from the Papautsky group used a spiral channel without containing sheath flow to separate particles, which are different sized. The chip, which is proposed by researchers, contains 5-loop and 10-loop spiral channels, and the channel has a rectangular cross-section by height 50 μm of width 100 μm. 7.32 and 1.9 μm particles were separated by using a 5-loop design chip, while 6 μm particles focused on using a 10-loop design chip. The same study was developed to remove polystyrene particles with a diameter of 10, 15, and 20 [Kuntaegowdanahalli et al., 2009].

When sheath buffer is used for the first time in a spiral platform, it was seen that clogging issues were prevented. In that experiment, a high throughput blood separation tool, defined as Dean Flow Fractionation (DFF), was applied to isolate CTCs from the blood [Hou et al., 2013]. The width of the channels is 500 μm, and the height is 155 μm. The design of the same study was replicated and clinically reported in addition to other research [Khoo et al., 2014]. Following the results, a report was prepared on the production and development of multiple spiral microchannels in order to perform CTC isolation [Warkiani et al., 2016].

Until now, many chip designs have been made, but this is not preferred because they are quite complex. For instance, a multiplexed device consist of 40 spirals was produced [Warkiani et al., 2015]. However, it is possible to achieve the aim with fewer channels containing chips. For that reason, a chip with a higher separation efficiency was designed in this thesis based on free from complexity studies. One important aim is that the channels in the chip are as few as possible, and a minimal chip is achieved.

The other method used for inertial focusing is contraction–expansion array (CEA) on both sides of the microchannel, or it is also known as multi-orifice flow fractionation (MOFF) with a series of microchambers, which was the first recommended by the Jung group in 2008. Large circulating tumor cells are isolated and classified by using a microfluidic vortex, occurring contraction, and expansion of the channel [Che et al., 2016]. These designs focus the particles by using the balance between micro vortices and inertial forces formed on each side to focus the particles on a particular path [Park et al., 2009]. In this study, a microchannel with 80 repeated contraction-expansion cycles, reported focusing 7 μm polystyrene divinylbenzene (PS-DVB). The authors claimed that the design is offered for continuous separation of

cells/particles with high efficiency. Although these kinds of platforms are ideal for separating smaller particles, for instance, blood cells among themselves, they are not sufficient for CTC (Park and Jung 2009). But these kinds of the platform not sufficient for CTCs. Tools should be developed to separate larger particles which represent CTCs.

The first chips used size differences between CTCs and blood cells to separate CTCs from blood cells, but they had an intricate design. The complexity made the production and usage of the chips demanding [Sarioglu et al., 2016], [Karabacak et al., 2014]. The alternative chips which contain filters and-or pinched segment in the structure are not preferred because of having a high probability of clogging [Chen et al., 2017], [Yamada et al., 2004]. Active separation methods use actuators or external forces to facilitate the separation of Stokes, magnetic forces, or centrifugal mesh from passive separation methods. In this aspect, active methods are distinguished from passive methods, determined depending on the physical properties or the structure of the particles.

Many techniques, which distinguish using any methods due to mixing, dilution, and measurement performed in Lab-on-a-CD techniques in the laboratory, can be easily applied in many cases in the Lab-on-a-chip approach. That approach operates with different samples, using various flow rates. Researchers preferred to use inertial focusing techniques and turn to hydrodynamic forces over time. These platforms are quite alluring because of providing label-free manipulations, not requiring any complex channel geometry and external force. Besides, they do not inflict any harm to living organisms. Therefore, inertial focusing techniques are the most preferred technique for particle manipulation, separation, and counting in the microfluidic systems.

Before developing these platforms, the forces that cause the particles to focus along their equilibrium trajectories are necessary to determine via computational fluid dynamics (CFD) methods [Liu et al., 2016], [Di Carlo et al., 2009]. Simulations of this kind are called direct numerical simulations and are computationally expensive, so one typically wants to minimize the number of such simulations and use their results in a more computationally efficient way. Benefiting from modeling can be useful for every

project because producing a model before starting wet-lab experience it helps to build the right thing [Parrott, 2017].

Modeling something means to represent the systems in math terms, which allow us to apply physics principles on it as in this project. Modeling makes easier the science usable on the system. Science analysis makes a model useful. Changing or controlling a model prevents lots of undesirable things. Modeling makes it easier to achieve a better solution. That is why we used modeling.

1.2. The objective of the Thesis

The current developments in microfluidic devices increase the people's request to detections of CTCs in human blood. However, each type of CTCs has different physical properties, such as size, deformation capacity, density [Hong et al., 2016]. Therefore, it is highly required to develop and optimize the microfluidic devices for different types of CTCs. To this end, the thesis aims to evolve and optimize a microchip that will separate different kinds of CTCs from the blood cells efficiently based on the various molecular weight and sizes between CTCs and other cells.

When investigating cancer, forensic scientists sometimes use cancer evidence to identify patients. A cell contains more than identifying information, though, like clues to our genetic makeup [Page et al., 2008]. Cell separation is used to take a closer look at the cancer cells, but traditional methods are time-consuming. The thesis aims to investigate the inertial focusing of spherical particles in square or rectangle straight or spiral channels with sheet flow or sheathless flow. Square and rectangle cross-sectional channels are used because manufacturing them accessible to other channels. Straight microchannels are used to show lift forces' effect on particles, and curvature microchannels are used to show both lift forces and drag force. Spherical particles are used because of their similarities to the basic shape of cell shapes.

This study develops a general computational model to achieve CTC separation by optimizing the geometry of the chip channel. For this purpose, boundary conditions, flow rate, and the fluid density and viscosity, corresponding to the liquid, are optimized to achieve the separation of CTCs.

This thesis has reported the development of a prototype device simulation to separate CTCs as a target cell from whole blood samples. In the simulation of the chip, six different CTC types from various tissues were utilized. The diameter of the cells, coming from non-small cell lung cancer is between 30 μm and 40 μm (NCI-H2126, ATCC CCL-256). The diameter of the cells, coming from breast cancer is between 25 μm and 35 μm, (UACC- 1179, ATCC CRL-3127). The diameter of the cells, coming from ovarian cancer is between 15 μm and 35 μm (EFO-27, DSMZ ACC-191). The diameter of the cells, coming from melanoma is between 25 μm and 40 μm (A-375, ATCC CRL-1619). The diameter of the cells, coming from pancreatic adenocarcinoma is between 25 μm and 40 μm (PA- TU-8988S, DSMZ ACC-204). The blood cells are much smaller in diameter CTCs. For instance, the diameter of white blood cells is between 8 μm and 15 μm, the diameter of red blood cells is between 6 μm and 7 μm, and the diameter of platelets between 1 μm and 3 μm.

This work aims to detect CTCs in the blood using microfluidic systems. Leukocytes are the largest cells in the blood cells. Some CTCs' size is equal to the largest leukocytes size, or they are more massive than leukocytes [Vona et al., 2000]. As explained, the smallest ovarian cancer cell we targeted and the largest white blood cell having a diameter of 15 microns, made us think a little. However, the desire to cluster cancer cells within themselves and with other blood cells increases their diameter [Au et al., 2017], [Jiang et al., 2018]. For this reason, we identified the smallest cancer cell in the simulations with a diameter of 25 microns. In the simulation, 11 different particles were used to increase the variety of particles. The particles (the radius of them between 25 and 40 μm) represents CTC kinds, other particles (the radius of them between 1 and 15 μm) means the blood cells in the simulation. The simulation of the particle position changes is shown under the effect of hydrodynamic forces in different shaped microchannels.

Numerical simulations are presented as a useful tool to see how different balances affect the dynamics of particles in a complex system. In this study, three-dimensional spiral channel geometries are modeled using COMSOL (version 5.5) computerized fluid dynamics.

Based on our literature search, many active and passive techniques to perform particle/cell isolation has been shown. It is shown that almost all clinical experiments

to detect CTCs from human blood by using passive techniques are based on immunofluorescence, fixation and permeabilization, staining, flushing, and detection methods. It would take more than one hour to complete this long process. Several hours would be spent to perform additional processing in one clinical experiment in many reports, and it has been suggested that inherent microfluidics containing active techniques instead of traditional methods, including passive methods, are preferred to separate them into blood components.

We can say that inertial microfluidics is chosen because they are superior to conventional microfluidics. Thus, first, the design, production, ease of use, secondly, it can be integrated with other systems, and thirdly, when compared with other systems, the inertial microfluidics are attractive to people because of their efficiency. Because of all the reasons which are explained, people apply to inertial microfluidics to manipulate biological particles.

It is indispensable to produce a microfluidic device to assist these procedures with advanced microtechnology and in order to reach the ideal chip with this consciousness. For that reason, our work aims to model and simulates a microfluidic platform that separates CTCs efficiently from other cells in the blood. In the thesis, sorting is done using inertial forces. Therefore, we do not require any external force. The inertial forces, produced according to flow rate and channel geometry, are dominant in particle orientation. The particle orientation changes are shown by simulations. The chip is environmentally friendly, suitable for every lab, and the chip is easy to use. The chip optimization was carried out to lead experimental studies; thus, the thesis achieved the goal.

1.3. Scope of the Thesis

Chapter 1: A background information is presented about inertial forces and fluid flows, which affect particle orientation. A comparison of methods from past to present microfluidic systems to manipulate CTCs and blood cells to separate them from each other in the literature is discussed.

Chapter 2: The history of inertial microfluidic systems and inertial forces in microfluidics are briefly explained. The parameter affecting particle movement is disclosed to achieve the most efficient CTC separation simulation.

Chapter 3: Computational Model and Chip Designs were made to target CTCs. The chip optimization was carried out to lead experimental studies.

Chapter 4: CTCs are separated from blood cells in the straight and spiral channels by using COMSOL simulation. 2D and 3D simulation images are represented.

Chapter 5: Comparison of the simulation result in that thesis with other simulations and experiments in the literature was conducted. How microfluidic systems can be developed in the future and simulations in the thesis have been explained how can shed light on science. The thesis achieved the goal.

2. MICROSCALE BEHAVIOR OF FLUIDS

The understanding of physics behind fluid flow at the microscale is essential for modeling the miniature systems. Therefore, this part of the thesis aims to explain the physics of the flow at microscale. In the literature, there are several of dimensionless numbers that fully characterize the behavior of fluid underflow. The most essential and critical fluid mechanics among these are the Reynolds number (R_e). Irish scientist Osborne Reynolds discovered this number many years ago, Osborn [Purcell, 1977]. This number is defined as a dimensionless number describing the static and dynamic properties of the fluid flow [Osborne, 1883]. The Reynolds number characterizes the behavior of fluid flow, and it is defined as

$$R_e = \frac{F_{inertia}}{F_{viscous}} = \frac{\rho V D_h}{\mu} = \frac{V D_h}{\upsilon} \tag{2.1}$$

where $\rho(kg/m^3)$, the density of the fluid; $V(SI\ unit: m/s)$, the characteristic velocity of the flow; $D_h(m)$, the hydraulic diameter of the channel; $\mu(Pa \times s)$, the dynamic viscosity of fluid and $\upsilon(m^2/s)$, the kinematic viscosity.

The Reynolds number is defined as the ratio magnitude of inertia forces to viscous forces. The ratio of This force gives us the flow information, which is a laminar or turbulent flow. Turbulent flow is a type of fluid flow in which the fluid undergoes irregular fluctuations and mixing, whereas, in laminar flow, fluid travels smoothly or in regular paths. In turbulent flow, the liquid is exposed to blurring and mixing. However, in laminar flow, the liquid moves on smooth or regular roads. Therefore, laminar flow is differentiated from the turbulent flow with its regularity property. When the fluid moves slowly in the channel, and the channel cross-section is small, laminar flow formation is observed in the channel. For example, let us consider that oil flows through a thin tube. Blood flowing in the capillary is also in the form of laminar flow. In the laminar conditions, two or more layers of fluids flow without any mixing. In laminar flow, particles move between flowlines and are dispersed in the fluid. The fact that parallel flows in laminar flow and particles move by changing the speed between these flow lines provide an excellent opportunity to model cells and

their environment. Microfluidic platforms with particle removal are operated in laminar flow regimes where viscous forces are dominant, and Reynold's number is low.

The value where the Reynolds number is less than 1 refers to the values where the viscous forces are dominant, where the inertia forces are neglected as Reynolds sales increase, the dominance of the inertial forces against the viscose forces increases. At low Reynolds values, the flow is laminar, and the flow rate changes are regular as it moves away from the wall. In high Reynolds numbers, the flow rate changes in a turbulent manner over time as Reynolds numbers increase, the dominance of the inertial forces against the viscose forces increases. At low Reynolds values, the flow is laminar, and the flow rate changes are regular as it moves away from the wall. In high Reynolds numbers, the flow rate changes in a turbulent manner over time.

If the viscous force dominates the inertia force, the Reynolds number is less than one, and no particle migration occurs between the flow lines. In cases where the Reynolds number is greater than 1, the particle tends to shift between the streamlines. The inertial forces the particle migration in opposite directions until the forces bring the particle to the equilibrium position. When the particle reaches the balance position, the magnitudes of these forces are balanced. Thus, the particles are separated from each other and reached to different equilibrium positions.

In this thesis, non-circular channels were used to observe the particle position. The calculation of the channel hydraulic diameter D_h, is defined as

$$D_h = \frac{4A}{P} \tag{2.2}$$

where $A(m^2)$, the cross-sectional area of the flow and $P(m)$, the wetted perimeter of the cross-section.

The hydraulic diameter formula for rectangular duct (filled) defined as

$$D_h = \frac{4hw}{2(h+w)} = \frac{2hw}{h+w} \tag{2.3}$$

where, (m), hight of the channel and $w(m)$, with of the channel. The duct is closed so that the wetted perimeter consists of the four sides of the duct.

Each particle has a particle Reynolds number Re_p, and it is defined as

$$Re_p = Re \times \left(\frac{a}{D_h}\right)^2 = \frac{\rho V a^2}{\mu D_h} \tag{2.4}$$

where $a(m)$, the particle diameter; $D_{\mathrm{h}}(m)$, the hydraulic diameter of the channel; $\rho(kg/m^3)$, the density of the fluid; $V(m/s)$, the characteristic velocity of the flow; $\mu(Pa \times s)$, the dynamic viscosity of the fluid.

The particles are thought to move in line with the flow lines when no external force is applied to the particle. Unlike this drop, however, it was observed that particles contained in the laminar flow migrated, as shown in figure 2.1. When the inertial forces on particles become significant, the migration of the particles between the streamlines happens. For instance, in this thesis, inertial lift forces were manipulated to focus the particles on different streamlines by using circular channels and developing simple prototype systems for high-throughput separations [Di Carlo et al., 2007].

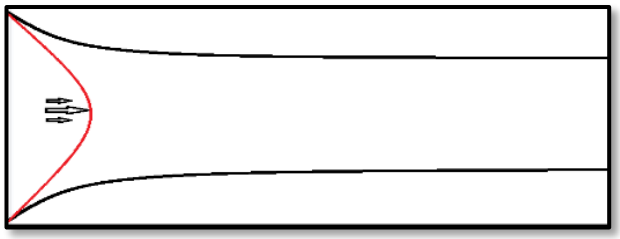

Figure 2.1: The figure shows when the velocities are sufficiently low, the streak of particle extended in a straight line through the tube. Redline leads to flow, arrows show flow direction, and two parabolic parallel line shows particle movement in the flow.

2.1. Microfluidics Flow Theory: Physical laws

Stokes

An expression was derived by George Gabriel in 1851; now, it is known as Stokes' law. In the small Reynolds numbers of the Navier–Stokes equations, by solving the Stokes flow limit, Stokes' law is produced. That means Stokes' law is valid if the flow is laminar, particles are spherical and do not interfere with each other, and the material should have a smooth surface. It is valid under conditions of Stokes law where the motion of the particle does not cause turbulence. George Stokes (1819-1903), who tried to understand the drag force around the sphere in the fluid, ignoring the term inertia, he derived the equation of motion by taking the work of Claude Louis Navier (1785-1836) one step further and stated the Navier-Stokes equation [Quake et al., 2005].

For a given fluid and a given velocity, the resistance is determined as proportional to the sphere's radius, not with the surface area of the sphere. [Stokes et al., 1850]. To make the manner of telling simple; if a sphere with a radius of a micron is taken and put in a quite viscous liquid, such as glycerin, the liquid produces smoothly flow around the ball when it falls, which make a pattern like below [Papanastasiou et al., 2000].

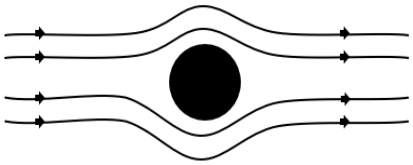

Figure 2.2: The figure illustrates a spherical particle movement and the streamlines around it in the flow. The arrows define the fluid flow direction, as seen. That kind of smooth flow occurs just for the relatively slow motion of the liquid.

Segré & Silberberg

In a tube or channel with a pressure-driven flow, small particles which are spherical are thought to not drift across streamlines. The first explanation of inertial focusing of floating neutral small spherical particle migration across the streamlines of a laminar flow was documented by Segré & Silberberg as [Segré et al., 1962]. The blood corpuscles incline to be distributed non-uniformly in the blood vessels. That increased the motivation of the Segre & Silberberg experiment. Therefore, they performed experiments by observing the movement of the rigid spheres in diluted suspensions in the pipe under the laminar flow regime. They observed that when the particles with 1-mm diameter were randomly dispersed in a flow-through a cylindrical pipe of 1-cm in diameter, those particles migrated an annulus, with a mean of ~0.6 times the pipe radius, were located between the centerline of the pipe and pipe wall as shown in figure 2.3 [Segré et al., 1961], [Segré et al., 1962]. That fact is determined as the tubular pinch effect. The fluid viscosity increases with the presence of the particles. Therefore, the fluid velocity profile gets flattened across the pipe at a particular time. In the experiment, the reason for the use of spherical particles was the mathematics of the viscous drag on irregular shapes is complicated.

For this reason, only the case of a falling sphere was considered in experiments by Segré & Silberberg. The findings lead to investigations by various researchers to this phenomenon. In the later studies, it was shown that large particles could be focused near the center of a straight channel in a reasonable flow rate, leaving smaller particles flowing near the channel wall by the effect of inertial focusing [Martel et al., 2014], [Kuntaegowdanahalli et al., 2009].

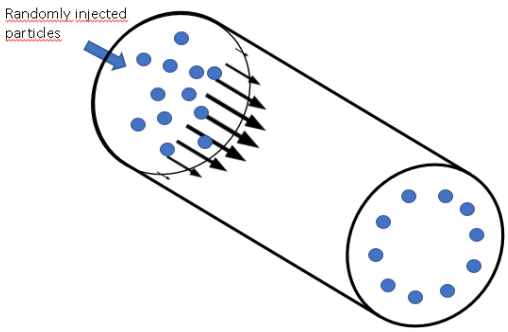

Figure 2.3: Observation of the inertial particle focusing in a pipe on the scheme. The arrows show the flow direction.

Philip Saffman

Philip Saffman showed how fluid inertia leads to particle migration as illustrating the first detailed analysis of particle movement in the presence of the shear flow [Saffman, 1965]. Therefore, Prof. Saffman contributed to the problem of the understanding of how the fluid inertia leads to a lift force that manages particle drift across the streamlines, as shown in figure 2.4. There are some difficulties, such as the calculation of the inertia effect for each particle. Also, the impact of the tube walls on flow should be considered. The walls give the particles to distance information. Because of that, the walls are critical [Stone, 2000].

The essential contributions were made to the lift force calculation on particles when the Reynolds number is small by Philip Saffman. Also, he pointed out explanations of the primary experimental investigation of Segre & Silberberg (1962). The contributed, compressibility effects in low-Reynolds-number flows, and also the speculations on particle motion in rapidly rotating flows. Professor Saffman investigated the structure of viscous boundary layers with Derek Moore, who was a mathematician at Imperial College. Because when particles move in rapidly rotating fluids, the form of boundary layers is crucially important.

As a result of their experiment, they agreed on if there is a pressure gradient on the particle in a parabolic pipe flow, a neutrally floating particle moves relative to the local fluid [Stone, 2000].

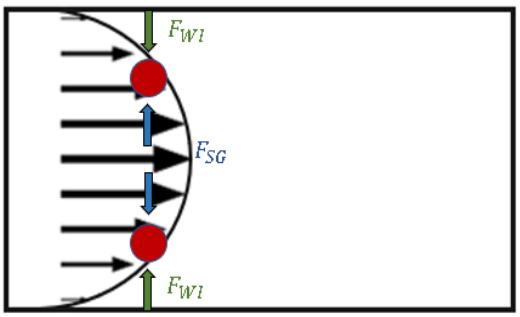

Figure 2.4: Illustration of the lift forces acting on particles in the laminar flow in a straight channel. Black arrows show the flow direction.

2.2. Hydrodynamic Forces

Three different forces affect the particle position in inertial focusing, and each force is respectively defined below. These forces on a spherical particle vary depending on the channel geometry and Reynolds number [Zhou et al., 2017], [Di Carlo et al., 2009]. Therefore, when we change the channel geometry, these forces direct the particles in the channel as we desired [Martel et al., 2014]. In a straight channel under laminar flow, lateral particle migration is directed by two inertial lift forces (F_L), which are perpendicular to the flow direction.

The first force is the wall induced lift force (F_{WI}) which pushes particles from the wall to the middle of the channel and the second force is the shear gradient lift force (F_{SG}) repulses them back towards the channel wall as shown in figure 2.4 [Hur et al., 2010]. These forces are depended on the particle size. Therefore, under those forces, different sized particles settle on the various equilibrium positions during a period in the channel [Karnis et al., 1966].

More inertial force occurs on the most massive particles moving in a straight microchannel, causing the particles to be lined up like wagons of a train. By taking advantage of this difference, large particles are captured by selecting the length of the channel at an ideal length, since more massive particles will be equilibrated into a single row before relatively smaller particles reach an equilibrium [Zhou et al., 2013].

The disfiguring the linearity of the channel and adding curvatures to the channel initiate the Dean vortices, which are secondary vortices [Di Carlo et al., 2007]. Dean vortices have occurred as perpendicular to the main flow stream. Where the Dean flow occurs, the top and bottom flow of the channel leads to the inward of the channel cross-section. However, the flow at the midline of the channel is directed to the walls as produce a curve [Gossett et al., 2009]. Particles are stabilized along the channel centerline cross-section.

However, while the third force, drag force (F_D) occurring by Dean flow acts perpendicular to the flow direction and causes particles to migrate around the cross-section. Therefore, a new equilibrium position occurs from the ratio ofF_L to F_D [Carlo et al., 2007]. Velocity mismatches have occurred between particles, which are near channel walls and those that are closer to the channel center, in the curved channels

[Di Carlo et al., 2009], [Zhang et al., 2016]. The particle near the channel center has high inertia, but the particles near the channel walls are almost stagnant. This causes velocity mismatches and resulted in two symmetrical secondary flows that are perpendicular to the liquid main flow. The platforms use the balance between inertial lift forces and Dean drag force to focus particles close to the spiral channel sidewalls.

Wall Induced Lift Force

If used particles are not incredibly small (behaving not like liquid molecules) or the walls in a channel are not enormously far from the particles, that means the particles which are flow through the channel have interact with the channel wall. This interaction causes two significant effects on the particle. The first effect causes particles to slow down so that the particles move slightly more slowly than the fluid in which they are present. The second effect generates pressure as a result of the liquid compression between the particle and the wall. This pressure causes a force, which is directed from the walls of the channel to the center of the channel. That force is defined as wall induced lift force (F_{WI}), as shown in figure 2.5 [Martel et al., 2014], [Carlo et al., 2007], [Ekanayake et al., 2018], [Zeng et al., 2009].

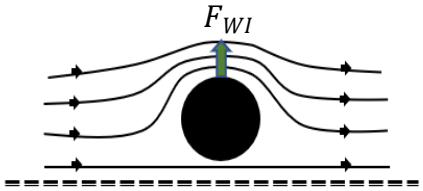

Figure 2.5: Illustration of the wall induced lift force. The fluid moving near the wall accelerates and causes low pressure on the top and higher pressure on the wall side of the particle; as a result of this, the wall induced lift force generates. Black arrows show the flow direction, and the green arrow shows the force direction.

The formula of the wall induced lift force defined as

$$F_{WI} = C_{WI}\rho {U_{Max}}^2 \frac{a^6}{{D_h}^4} \tag{2.5}$$

where, C_{WI}, lift coefficient for the wall interaction force; $\rho(kg/m^3)$, fluid density; $U_{\mathrm{Max}}(m/s)$, the maximum velocity of the fluid; $a(\ m)$, particle diameter. $D_{\mathrm{h}}(m)$, the hydraulic diameter of the channel.

Shear Gradient Lift Force

The velocity profile produces a force on the particles in a flow. A typical microfluidic velocity profile is parabolic, as shown in figure 2.6 [Winer et al., 2014].

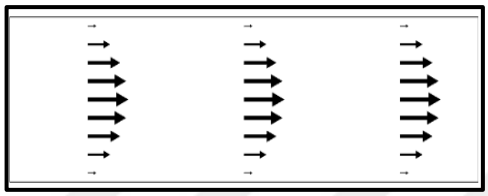

Figure 2.6: Illustration of the velocity profile, which is parabolic of the particles in a two-dimensional display of straight channel. Three different cut lines that are perpendicular to the length of the channel are taken, and the velocity profile is shown by arrows throughout flow direction on these cut planes.

In such laminar flow, the particles have different velocity magnitudes on both sides of the channel [Bruus H.,2006]. This difference is compensated by the fluid flow, which is around the particles. This fluid flow thus forms a force towards the particles, which is Shear gradient lift force [Pnueli et al., 1997]. That force migrates the particles away from the channel center towards the wall, as shown in Figure 2.7 [Carlo et al., 2007], [Thomas et al., 2015].

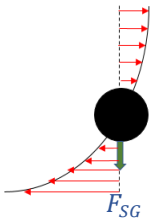

Figure 2.7: Illustration of the shear gradient lift force on a spherical particle in the laminar flow. The difference in velocity of both sides of the particle causes a pressure difference that imparts a force directed toward the higher-relative-velocity (walls of the channel) side of the particle. This pressure creates a shear gradient lift force.

The shear gradient lift force on a moving spherical particle is expressed as

$$F_{SG} = C_{SG}\rho {U_{Max}}^2 \frac{a^3}{D_h} \tag{2.6}$$

where, C_{SG}, lift coefficient for shear gradient lift force; $\rho(kg/m^3)$, fluid density; $U_{\mathrm{Max}}(m/s)$; the maximum velocity of the fluid; $a(m)$, particle diameter. $D_{\mathrm{h}}(\ m)$ the hydraulic diameter of the channel.

Secondary-Flow Drag Force

In the Segré & Silberberg experiment, when all kinds of particles move regardless of time in a proper laminar flow in a straight pipe of sufficient length, these particles will settle in the plan of distant spots ~0.6 times the radius of the channel from the center of the blood. When we change channel geometry from straight to curved, the two effects on suspended particles: not only inertial migration but also secondary flow are observed. Therefore, both inertial forces and secondary forces occur. When different sized particles are randomly dispersed in the inlet and start flowing through a spiral, Dean vortices develop, as shown in figure 2.8. Dean vortices produce drag forces, which cause the particles to follow the direction of these vortices in addition to the main streamflow. Thus, also secondary-flow drag force on particles in addition to wall induced, shear gradient lift forces are observed. Secondary flows manipulate the number of equilibrium position within the channel cross-section [Zhang et al., 2016].

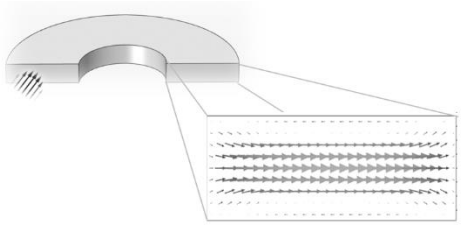

Figure 2.8: Microchannel cross-section illustrating Dean flow. Grey arrows indicate flow direction. The arrows are proportional to the flow velocity. The Dean flow direction in the center of the channel cross-section is through the outer wall of the channel. However, the Dean flow, which is in the up and down section of the channel is in the opposite direction.

In the spiral channels, Dean flow occurs, as shown in figure 2.9. Dean flow accelerates as simulating fluid flow. Therefore, the lateral migration of particles is getting faster. As a result, Dean flow affects the distribution of the equilibrium position of the particles in the vertical cross-section of the channel [Norouzi et al., 2014]. Dean flow arranges particles' balance positions according to their particle diameter [Ault et al., 2015], [Gou et al., 2018].

This thesis shows the particle position changes under the secondary-flow drag force. Particles moving in the flow come to equilibrium after a while under the effect of secondary-drag force. As a result, the same particles are positioned on the same line; the particles of different sizes are placed on a separate line. The drag force occurred by Dean flow shown in figure 2.9.

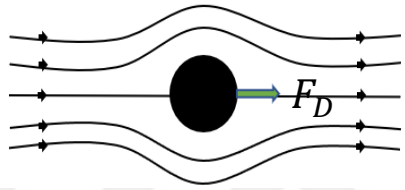

Figure 2.9: The figure illustrates the secondary-flow drag force acting on the spherical particle, moving in the liquid. When the fluid flows past an object or when an object moves through a fluid, the fluid causes the drag force. The elements of the fluid are displaced out of the way of the moving object by the drag force. The force, which is known as Stokes' drag is dependent on the difference between the fluid velocity and the particle velocity. Black arrows show the flow direction, and the green arrow shows the force direction.

The secondary drag force, occurring by dean flow acting on bigger particles more than smaller. So, in a particular time, more massive particles riches their focusing point than smaller particles. The secondary-flow drag force on a moving spherical particle is expressed as

$$F_D = 6\pi\mu a U_{SF} \tag{2.7}$$

Where π, pi number; $\mu(Pa \times s)$, fluid viscosity. $a(\mu m)$, particle diameter; $U_{\mathrm{SF}}(m/s)$, secondary-flow velocity.

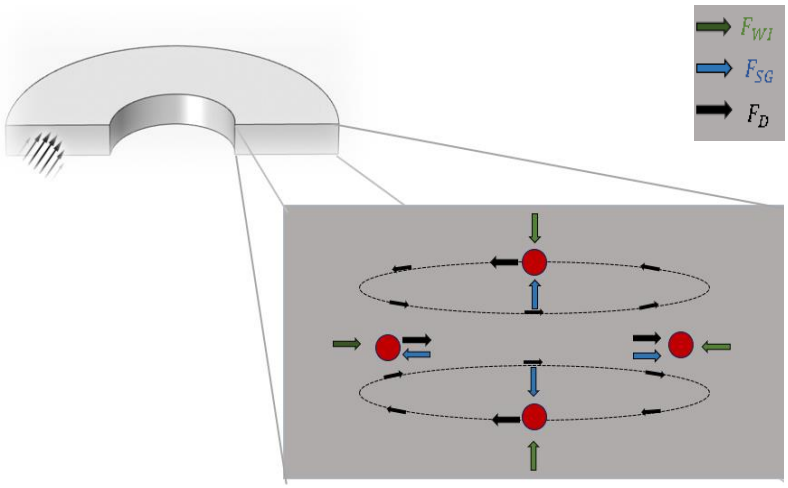

Figure 2.10: The figure illustrates the forces acting on particles at various parts of the vertical channel cross-section. The first one is the wall induced lift force (green) that pushes particles toward the middle of the channel. The second one is the shear gradient lift force (blue), which pushes them back towards the channel wall. The last one is the drag force (black), occurring by Dean flow and causes particles to migrate around the cross-section. Arrows indicate the force directions.

In the spiral channels also secondary-flow drag force on particles in addition to wall induced, shear gradient lift forces are observed, as shown in figure 2.10. The effect of these three forces on particles is dependent on particle mass and particle sizes. In time, the different sized particles settle at different equilibrium positions under those forces. Therefore, the drag force is the ultimate factor used to separate particles.

3. COMPUTATIONAL MODEL and CHIP DESIGN

Computational fluid dynamics (CFD) is a tool that uses numerical simulations to analyze and solve the problems for fluid dynamics. COMSOL is preferable for particle tracking [Bagchi et al., 2005]. It is also used to separate particles by using magnetic forces besides inertial forces [Han et al., 2015]. In our simulations, we tracked the particles (different size cells) for separation based on their sizes by using the particle tracing module in COMSOL Multiphysics. We performed three-dimensional COMSOL simulations in order to model our microchip, to maximizing the CTCs trapping.

The thesis aims to distinguish the CTCs from diluted human blood with the hundred percent yield. For this purpose, we designed chips with different channel sizes and recorded the location of the particles for a particular time in the laminar flow regime. Firstly, the simulations were carried out for straight channels, having several channel aspect ratios to investigate the focusing pattern of different size particles. We defined cross-section areas of the straight channels at the inlet, middle, and outlet, and analyzed how the inertial forces affect particle position through the channel. Then, the simulations were carried out for spiral channels with the optimum channel aspect ratio.

Furthermore, we used different flow rates, consequently, different Reynolds numbers for simulations. In this way, we compared the relationship between the Reynolds number and the focusing efficiency of the spiral channels. As a result, with the help of tracking the particles within the channels, we observed the forces on the particles and determined the channel length for the hundred percent CTCs separation.

3.1. The Statements and Governing Equations of COMSOL

This section explains the assumptions that we made and the governing equations that COMSOL used. We used two modules in COMSOL; the first one is laminar flow, and the second one is the particle tracing module to pursue the particles within the microchannel. In the laminar flow module, we chose incompressible flow as the physical model, and the incompressible Navier-Stokes equations with the general form:

$$\rho(\mathbf{u}\cdot\nabla)\mathbf{u} = \nabla\cdot[-p\mathbf{l} + \mathbf{K}] + \mathbf{F} \quad (3.1)$$

where $\boldsymbol{\rho}$ (kg/m^3), the density; $\mathbf{u}$ (m/s), the velocity vector; $p(Pa)$, the dependent pressure variable from the Navier-Stokes; $\mathbf{l}$ $(dimensionless)$, the unit tensor which is an identity matrix; $\mathbf{K}$ $(dimensionless)$, the symmetric deformation tensor; $\mathbf{F}$ (N/m^3), body force.

The equations of fluid motion in the convective form:

$$\frac{D\rho}{Dt} + \rho\nabla.\mathbf{u} = 0 \quad (3.2)$$

$$\rho\nabla.\mathbf{u} = 0 \quad (3.3)$$

where p (Pa), the pressure; $\boldsymbol{\rho}$ (kg/m^3), the density; $\mathbf{u}$ (m/s), the velocity vector.

The deformation tensor in Equation 3.1 is defined as

$$\boldsymbol{K} = \mu(\nabla\mathbf{u} + (\nabla\mathbf{u})^{\mathrm{T}}) \quad (3.4)$$

where, μ $(Pa \times s)$, fluid viscosity; $\mathbf{u}$ (m/s), the velocity vector.

If the fluid is incompressible, that means the fluid is divergence-free, and the total volume stays the same over time; otherwise, it will shrink or expand. The total derivative is equal to zero since the density does not change.

We selected the no-slip velocity boundary condition. It assumes that the velocity of the fluid layer in direct contact with the wall is equal to the velocity of this wall, which is zero in our case. The no-slip condition was determined as

$$\mathbf{u} = \mathbf{0} \quad (3.5)$$

where, $\mathbf{u}$ (m/s) is the velocity vector.

As inlet condition velocity is defined as

$$\mathbf{u} = -U_0\mathbf{n} \quad (3.6)$$

where, $\mathbf{u}\ (m/s)$, the velocity vector; $U_0\ \ (m/s)$, the inlet velocity vector; n$(dimensionless)$, the outward normal. The normal vector is perpendicular to the entrance of the channel and outwards from the channel. Therefore, it is in the opposite direction with the velocity vector.

As outlet condition pressure is defined as

$$[-p\mathbf{l} + \mathbf{K}]\mathrm{n} = -p_0\boldsymbol{n} \tag{3.7}$$

where, $p\ (Pa)$, the pressure; $\mathbf{l}(dimensionless)$, the unit tensor; $\mathbf{K}(dimensionless)$, the symmetric deformation tensor; $p_0(Pa)$, outlet pressure;

We defined material property inside the channel as the liquid. We assigned 0.001 Pa.s as dynamic fluid viscosity and 1000 kg/m^3 as particle density.

In the Particle Tracing Module, we defined 11 different sized particles, which are 1, 3, 6, 7, 8, 10, 15, 25, 30, 35, and 40 μm-diameter particles. The particle velocity was described as

$$\mathbf{v} = \mathbf{v}_c \tag{3.8}$$

where, $\mathbf{v}\ (m/s)$, the velocity of the particle; $\mathbf{v}_c(m/s)$, the particle velocity when striking the wall.

As inlet boundary conditions:

$$\mathbf{q} = \mathbf{q_0} \tag{3.9}$$

$$\mathbf{v} = \mathbf{v}_0 \tag{3.10}$$

where, $\mathbf{q}\ (m)$, the particle position; $\mathbf{q_0}(m)$, the initial particle position; $\mathbf{v}\ (m/s)$, the velocity of the particle; $\mathbf{v}_0(m/s)$, the initial particle velocity, which is based on the space dimension.

In order to prevent the particle escaping from the outlet and observing their final location within the channel, the freeze option was considered in our simulations.

$$\frac{d(m_{\mathrm{p}}\mathbf{v})}{dt} = \mathbf{F_D} + \mathbf{F_g} + \mathbf{F}_{\mathrm{ext}} \tag{3.11}$$

$$\mathbf{v} = \frac{d\mathbf{q}}{dt} \tag{3.12}$$

where, $m_{\mathrm{p}}\,(kg)$, the particle mass; $\mathbf{v}\,(m/s)$, the particle velocity; $\mathbf{F_D} + \mathbf{F_g} + \mathbf{F}_{\mathrm{ext}}\,(N)$, the drag, gravity, and other forces, respectively; $\mathbf{q}\,(m)$, the particle position.

Drag force acting on particles is defined as

$$\mathbf{F}_{\mathrm{D}} = \frac{1}{\tau_p} m_p(\mathbf{u} - \mathbf{u}_p) \tag{3.13}$$

where, $\tau_p(s)$, the particle velocity response time; $\mathbf{u}_p(m/s)$, particle velocity; $\mathbf{u}\,(m/s)$, the fluid velocity at the particle's position.

Strictly speaking, $\mathbf{u}$ is the value that the fluid velocity would have at the particle's position if no particle were there unless fluid-particle interactions are considered.

In the Stokes drag law, the velocity response time is defined as

$$\tau_p = \frac{\rho_p d_p^2}{18\mu} \tag{3.14}$$

where, $\mu\,(Pa \cdot s)$, the fluid viscosity; $\rho_p(kg/m3)$, particle density; $\mathrm{d}_p(SI\ unit: m)$, the particle diameter.

$$\mathbf{F}_{\mathrm{D}} = 3\pi\mu d_p(\mathbf{u} - \mathbf{v}) = 6\pi\mu r_p(\mathbf{u} - \mathbf{v}) \tag{3.15}$$

where,$\pi\ (dimensionless)$, pi number; $\mu\ (Pa \times s)$, fluid viscosity; $d_p(\mu m)$, particle diameter; $r_p\,(\mathrm{m})$, the particle radius; $\mathbf{u}\,(m/s)$, the fluid velocity at the particle's position, $\mathbf{v}\,(m/s)$, the velocity of the particle.

The Wall induced lift force model is described as the first-order correction to the velocity profile at the channel walls and a second-order correction at the surface of the

particle in order to account for higher-order derivatives of the fluid velocity compared to the Saffman model. It is given by

$$\mathbf{F}_{\mathrm{L}} = \rho \frac{r_p^4}{D^2} \beta(\beta G_1(s) + \gamma G_2(s))\mathbf{n} \tag{3.16}$$

$$\beta = \left| D(\mathbf{n} \cdot \nabla)\mathbf{u}_p \right| \tag{3.17}$$

$$\gamma = \left| \frac{D^2}{2} (\mathbf{n} \cdot \nabla)^2 \mathbf{u}_p \right| \tag{3.18}$$

$$\mathbf{u}_p = (I - \mathbf{n} \otimes \mathbf{n})\mathbf{u} \tag{3.19}$$

where, $\boldsymbol{\rho}$ $(kg/m3)$, the density; $r_p(m)$, the particle radius; D (m), the distance between the channel walls; G1 and G2 are functions of nondimensionalized wall distance; s, is the nondimensionalized distance from the particle to the first parallel boundary, divided by D so that 0 < s < 1 for particles in the channel; $\mathbf{n}$ $(dimensionless)$ is the wall-normal at the nearest point on the reference wall; $\mathbf{u}_p$ (m/s), the particle velocity; I(dimensionless), the identity matrix.

We added wall corrections option in the settings for the Drag Force node, the wall correction force ($\mathbf{F}_{\mathrm{WC}}$) described as

$$\mathbf{F}_{\mathrm{WC}} = \mathrm{M}\mathbf{F}_{\mathrm{D}} \tag{3.20}$$

$$\mathrm{M} = \frac{1}{1 - \frac{9}{16}\mathrm{a} + \frac{1}{8}\mathrm{a}^3 - \frac{45}{256}\mathrm{a}^4 - \frac{1}{16}\mathrm{a}^5}(\mathrm{I} - \mathrm{P}(\mathbf{n})) + \frac{1}{1 - \frac{1}{16}\mathrm{a} + \frac{1}{2}\mathrm{a}^3}\mathrm{P}(\mathbf{n}) \tag{3.21}$$

$$\mathrm{a} = \frac{\mathrm{r_p}}{\mathrm{l_W}} \tag{3.22}$$

where $M(dimensionless)$, the correction factor; $I(dimensionless)$, the identity matrix; $P(\mathbf{n})$ $(dimensionless)$, the projection operator onto the wall-normal, $\mathbf{n}$; $r_p(m)$, the radius of the particle; $l_W(m)$, the distance from the center of the particle to the nearest wall.

The first term in Eq. 3.21 applies to the component of the relative particle velocity parallel to the nearest wall; the second term applies to the component of the

relative velocity normal to this wall. The correction factors become more prominent as the wall distance becomes comparable to the particle radius.

While meshing the geometry, we chose physical-controlled mesh and modified element size changes from simulation to simulation. The main reason is that if we choose the mesh extremely fine in 3D simulations, the memory of the computer is not enough to complete the process. We defined two steps for the study module. The first one is a stationary study, which solves laminar flow physics, so in this part, we chose laminar flow as the physical interface. The second one is the time-dependent study, which solves particle tracing for fluid flow. Therefore, in this part, we chose just particle tracing for fluid flow as the physical interface. We set the time interval for the program to run.

3.2. Practical Channel Design Rules for Inertial Focusing

In the literature review, factors that will increase the focusing of the particles in the straight channels and determines the equilibrium positions of particles in the channel cross-section have been established and formulated. We designed the chips based on these factors. Thus, we obtained favorable results in particle separation. The First one is the aspect ratio (AR), the second one is the blockage ratio (κ), and the last one is, and the last one is the required channel length(L_f).

The aspect ratio defined as

$$AR = \frac{w}{h} \tag{3.23}$$

where, $h(m)$ is the height and $w(m)$ is the width of the channel cross-section.

The channel aspect ratio informs us about the positioning of the particle according to the shape of the channel. We studied the straight channel aspect ratio of one, more significant than one, and less than one, respectively. The second factor is in this context is the blockage ratio κ, which is defined as

$$\kappa = \frac{d_p}{h} \tag{3.24}$$

where, $d_p(m)$ is the diameter of the particle, and $h(m)$ is the height of the channel cross-section.

According to the given equation, If the used particle diameter increases, the diameter of the channel be increased in the same proportion to prevent blockage within the channel. The last factor is the channel length required to achieve focused particles on equilibrium positions. The required channel length to reach equilibrium positions of particles in inertial focusing is established upon the magnitudes of described forces. The adjustment for curved channels is less precise than straight channels, owing to the complex variation in behavior, but in general, the length required is shorter for curved channels because the secondary drag force effect the particles and makes inertial focusing accessible [Di Carlo et al., 2009], [Martel et al., 2014]. Thus, a channel length estimated using the linear channel approximation above should be sufficient for curved channels. The channel length required for effective particle separation is inversely proportional to the size of the particle. Therefore, more prolonged channels are required to separate smaller particles. While determining the length of the channel, we determined the length of the channel according to the smallest CTC cell kind.

The required channel length for linear channels is defined as

$$L_f \cong \frac{\pi \mu {D_h}^2}{C_{SG} \rho U_{Max} a^2} \tag{3.25}$$

where, π $(dimensionless)$, pi number; μ $(Pa \times s)$, the dynamic viscosity of fluid; $D_{\mathrm{h}}(m)$, the hydraulic diameter of the channel; C_{SG}, lift coefficient for shear gradient lift force; ρ (kg/m^3), the density of the fluid; U_{Max} (m/s), the maximum velocity of the fluid; a (μm), particle diameter.

3.3. Simulation Geometry

Firstly, we performed simulations for straight channels to determine the parameters that will determine the separation of particles, and then we worked on circular channels using these parameters.

3.3.1. Straight channels

Considering the cell density in the blood, we gave all the particles to the channel at the same time. So we would like to capture the particle density at a given moment. In the straight channels, in order to get a better picture of spatial particle distribution, 11 different sized particles were released from the channel inlet with a projected plane grid and random distribution in each simulation, respectively. In a projected plane grid distribution, particles of different sizes were released from 16 specific points simultaneously. Therefore, we observed how the particles were displaced according to their different sizes. We took vertical cross-sections of the inlet, the middle, and the outlet of the chip channel. Particles with the same size allowed us to answer the question of whether they are moving towards the same equilibrium position regardless of the entrance point of the channel. Also, the particles were injected into the inlets randomly, which was a step towards experimental studies.

Straight channels with AR 1

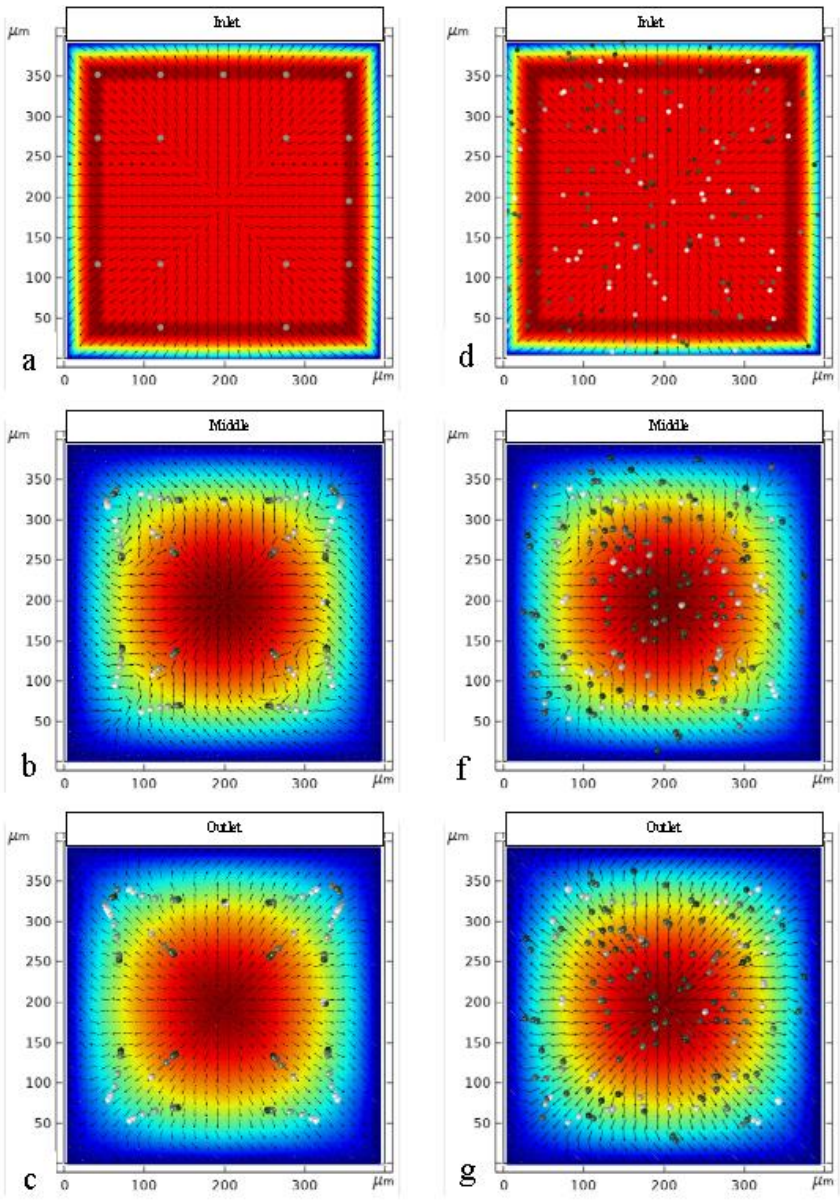

Figure 3.1: 3.1a, 3.1b, and 3.1c) Particle distribution at the inlet, the middle, and the outlet. The projected plane grid distribution option was used as inlet position. 3.1d, 3.1e, and 3.1f) Particle distribution at the inlet, the middle, and the outlet. The random distribution option was used as inlet position. 11 different size particles and 16 from each (a total of 176 particles) were simulated. White particles represent the CTCs (40, 35, 30, 25 μm); dark green particles represent blood cells (15, 10, 8, 7, 6, 3, 1 μm). The channel height, width, and length are 400 μm 400 μm and 40 cm, respectively. Aspect ratio, 1; flow rate, 3.2 ml/min; inlet velocity, 0.33 m/s; Reynolds number, 133.33; the blockage ratio is between 0.025 and 0.1. The x-axis and y-axis represent the width and height of the channel, respectively. The black arrows show the direction of the Dean flow that makes the particles move. The arrow size of the velocity vector in the figure is normalized.

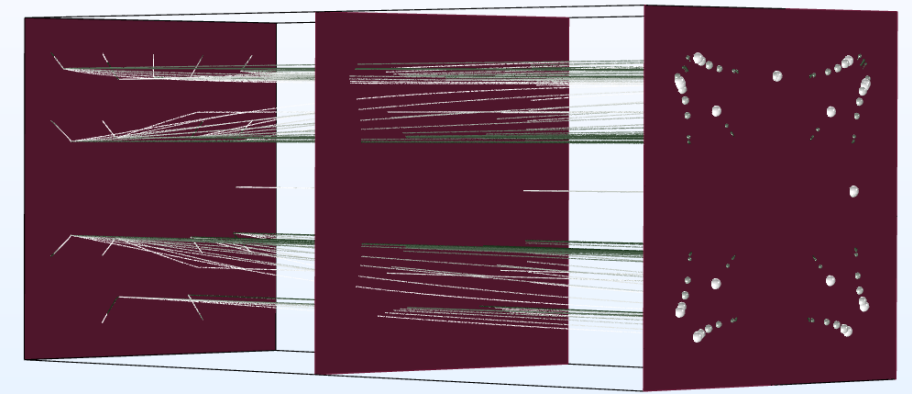

Figure 3.2: The figure shows the particle movement on vertical sections at the inlet, middle, and outlet of the channel in the channel whose aspect ratio is equal to 1. In the figure, the streamlines from the inlet(left) to the outlet(right) of the channel indicate the paths of the particles.

We used the projected plane grid distribution as a particle position in the inlet to compare the motion of particles of different sizes with each other and random particle distribution in the inlet to observe whether the particle inlet position affects the particle outlet position in our simulations. As seen in Fig.3.2, the particles representing the blood cells (green) followed a straight streamline along the channel. However, the particles representing the cancer cells (white) follow a parabolic streamline through the channel as they are strongly affected by the physical forces to direct their movements. Because of that reason, we can say that particles with a diameter of 15 microns and larger can move independently from their initial position and reach where it should be at the outlet in this simulation. However, particles with a diameter of 10 microns and smaller are dependent on their initial position. We observed that lift forces' effect on the particles was not enough to move them on the x-axis and y-axis through the channel. As can be seen, when the channel aspect ratio is equal to 1, the particle focusing power in the x-axis and y-axis of the channel outlet is the same as seen in Fig.3.1. Particle distributions at the outlet show us; larger particles focused much more than smaller particles due to the higher inertial lift force acting on more massive particles.

Straight channels with AR 0.3

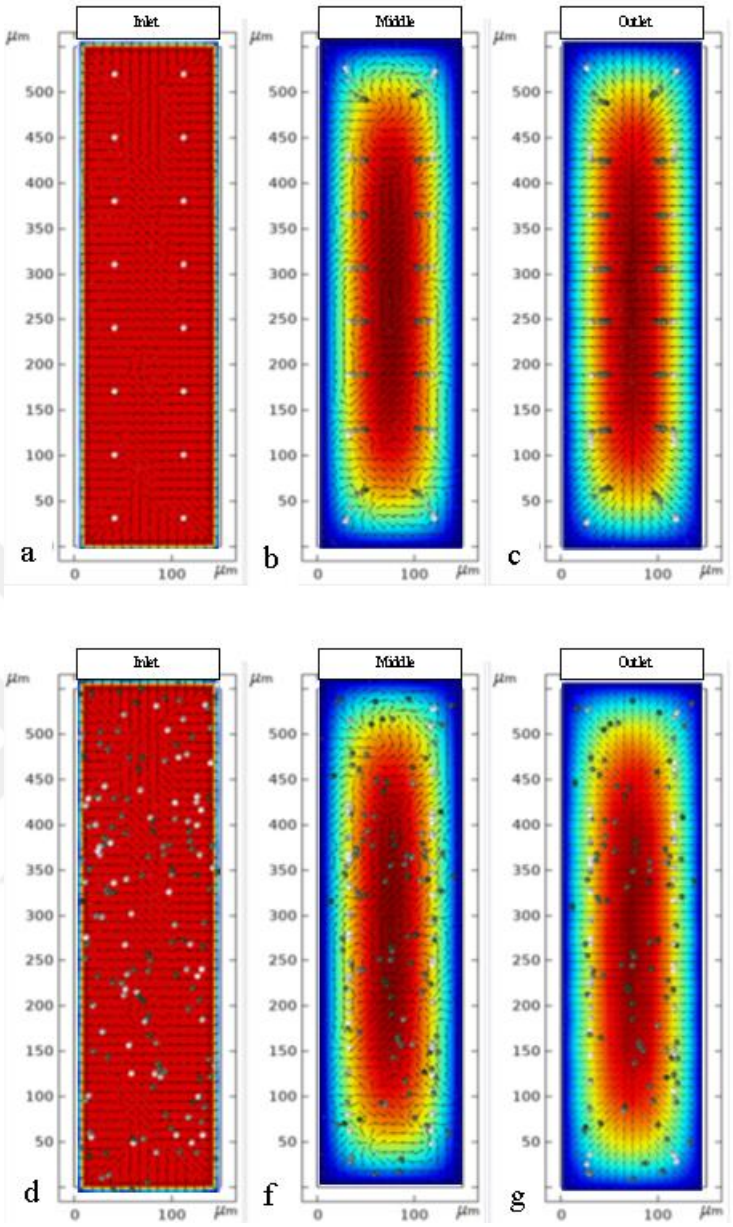

Figure 3.31: 3.3a, 3.3b, and 3.3c) Particle distribution at the inlet, the middle, and the outlet. The projected plane grid distribution option was used as inlet position. 3.3d, 3.3e, and 3.3f) Particle distribution at the inlet, the middle, and the outlet. The random distribution option was used as inlet position. 11 different size particles and 16 from each (a total of 176 particles) were simulated. White particles represent the CTCs (40, 35, 30, 25 μm); dark green particles represent blood cells (15, 10, 8, 7, 6, 3, 1 μm). The channel height, width, and length are 550 μm 150 μm and 15 cm, respectively. Aspect ratio, 0.3; flow rate, 1.65 ml/min; inlet velocity, 0.33 m/s; Reynolds number, 78.57; the blockage ratio is between 0.0018 and 0.072. The x-axis and y-axis represent the width and height of the channel, respectively. The black arrows show the direction of the Dean flow that makes the particles move. The arrow size of the velocity vector in the figure is normalized.

When we reduced the aspect ratio of the channel to less than one, we observed that particles focused on two different lines parallel to the y-axis, as shown in figure 3.3. The particles with a diameter of 10 microns focused on the equilibrium positions like the particles with diameters of 15 microns and larger, unlike its first and second simulations of the chip_1 due to the reduction of the vertical cross-sectional area of the channel. As an outcome of the first and second simulations of the chip_2, in outlets, the particles reached two stable parallel positions in the x-axis quickly and migrated slowly in the y-axis towards discrete equilibrium positions.

Straight channels with AR 3.66

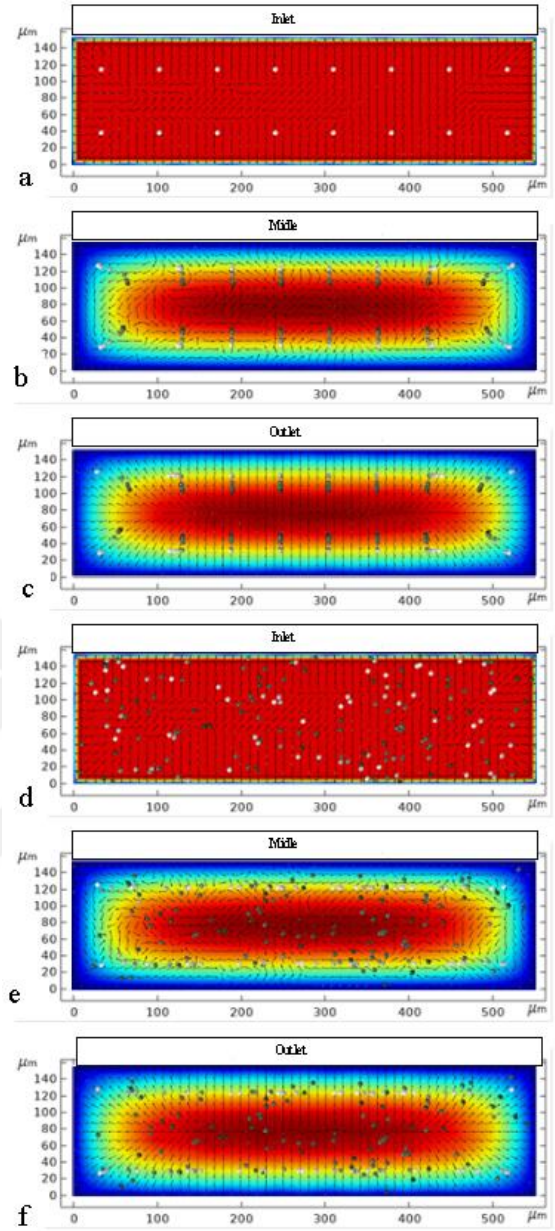

Figure 3.4: 3.4a, 3.4b, and 3.4c) Particle distribution at the inlet, the middle, and the outlet. The projected plane grid distribution option was used as inlet position. 3.4d, 3.4e, and 3.4f) Particle distribution at the inlet, the middle, and the outlet. The random distribution option was used as inlet position. 11 different size particles and 16 from each (a total of 176 particles) were simulated. White particles represent the CTCs (40, 35, 30, 25 μm); dark green particles represent blood cells (15, 10, 8, 7, 6, 3, 1 μm). The channel height, width, and length are 150 μm 550 μm and 15 cm, respectively. Aspect ratio, 3.66; flow rate, 3.2 ml/min; inlet velocity, 0.33 m/s; the Reynolds number, 78.57; the blockage ratio is between 0.006 and 0.26. The x-axis and y-axis represent the width and height of the channel, respectively. The black arrows show the direction of the Dean flow that makes the particles move. The arrow size of the velocity vector in the figure is normalized.

When we exceed the aspect ratio above 1, we observed that particles focus on two different lines parallel to the x-axis, as shown in figure 3.4. When we shrunk the channel cross-section area, we observed that also particles of 10-microns focus on the equilibrium position like the larger particles as in the third and fourth simulation. In outlets, the particles will reach two stable parallel positions in the y-axis quickly, and possibly migrate slowly in the x-axis towards discrete equilibrium positions

The particles representing CTCs located close to the center of the channel inlet moved away from the center towards the wall under the influence of shear gradient lift force in time. CTCs located near the wall of the channel inlet moved away from the wall towards the center under the influence of wall induced lift force. However, such an apparent displacement in all blood cells has not been observed.

3.3.2. Archimedian Spiral

Drag force is the dominant force in the spiral channels, so it is the leading force in the positioning of particles. In order to take advantage of this force, we examined the motion of the particles in the spiral channel. We applied sheath flow to increase particle separation. Sheath flow enhances the effect of drag force, providing the particles of different sizes to separate from each other in a shorter time and the particles of the same size to come together to focus on the specific streamlines. We designed several types of microdevices containing various length spiral channels and simulated them in order to examine the separation performance of different sized particles for each microchannel geometry. The devices' channels consist of a semicircle arc locating in the middle, an Archimedean spiral by adjoining to the semicircle arc, a line segment that directs the particle to outlets, and prism blocks for two inlets (sheath flow), and two outlets. The fact that the channel's aspect ratio is different from 1 has enabled the particles to focus on the long sides of the channel. We decided that the aspect ratio of the spiral channel should be greater than 1 since the duct geometry makes it easier for us to focus the particles on two sides, not on the four sides of the channel. As the channel's aspect ratio is higher than 1, the width of the channel gets easier for us to have two outlets on the channel. Thus, it allows us to easily collect particles representing CTCs from one outlet and particles representing blood cells from the other outlet. Therefore, we decided that the aspect ratio of the channel should be greater than 1. We observed that the focusing streamlines of the particles changed when we changed the flow rate while designing the channels of the chip. We decided on a standard geometry for chips, but when we changed the flow rate, we also changed the channel length to collect the CTCs with 100% efficiency. After the first optimization, we used the same geometry for the inlets and outlets of the chips. However, in the simulations, we observed that focusing positions of particles are changed when the flow rate of the inlets was changed. So, we optimized the number of turns for each simulation. We designed six chips, three of them containing sheath flow as shown in figures 3.5, 3.6, and 3.7, three of them not as shown in figures 3.8, 3.9, and 3.10. The number of turns optimized to increase separation efficiency. As the first chip, we described the chip, which has the most extended channel because the particle motion is better observed in each turn of the channel.

3.3.2.1. Spiral Channel (8 Turns, 492.165 mm) Containing Sheath Flow (Re=13.13)

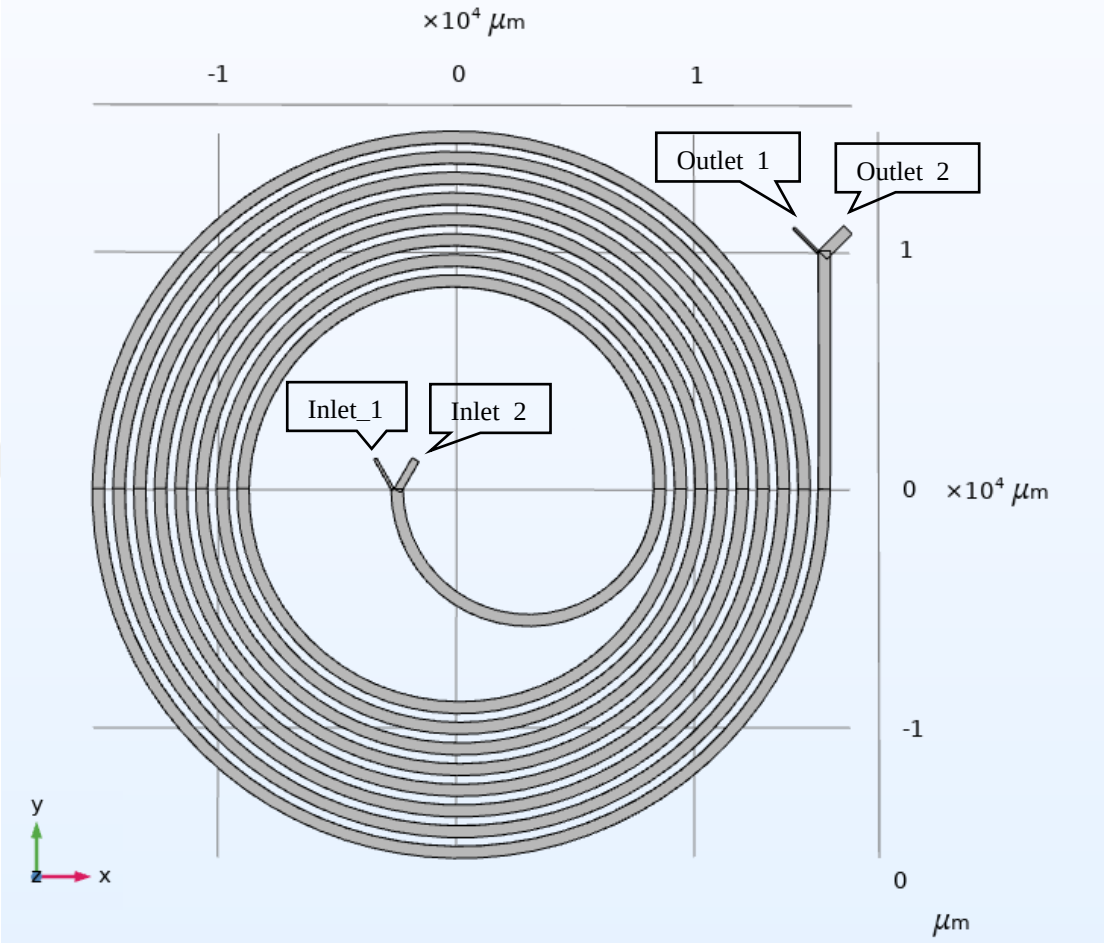

Figure 3.5: Schematic representation of the geometry of chip_4. The geometry consists of a semicircle, an Archimedean spiral, a line segment, and four rectangular prism blocks. Semicircular arc length, 15705 μm; parametric curve has seven turns, and it is length, 468460 μm; line segment length, 8000 μm ; channel length, 492.165 mm; the length of the distance between two spiral channel, 547.66 μm; the channel width 500 μm; the height of inlets and outlets, 150 μm; the length of inlets and outlets, 1500 μm; width of the inlet_1, 125 μm; width of the inlet_2, 330 μm; the angle of the inlets with the y-axis, 30 degrees; width of the outlet_1, 100 μm, width of the outlet_2, 500 μm; the angle of the outlets with the y-axis, 45 degrees; semicircular arc radius, 500 μm; initial spiral radius, 7000 μm; final spiral radius, 14300; initial angle, 0; final angle, 43.982; the growth rate of spiral, 165.98; volume, 3.7198E10 μm^3; surface area, 6.452E8 μm^2; x minimum, -14029 μm; x maximum, 15550 μm; y minimum: -14290 μm; y maximum, 13768 μm; z minimum, -75 μm; z maximum, 75 μm.

3.3.2.2. Spiral Channel (3 Turns, 209.046 mm,) Containing Sheath Flow (Re=39.23)

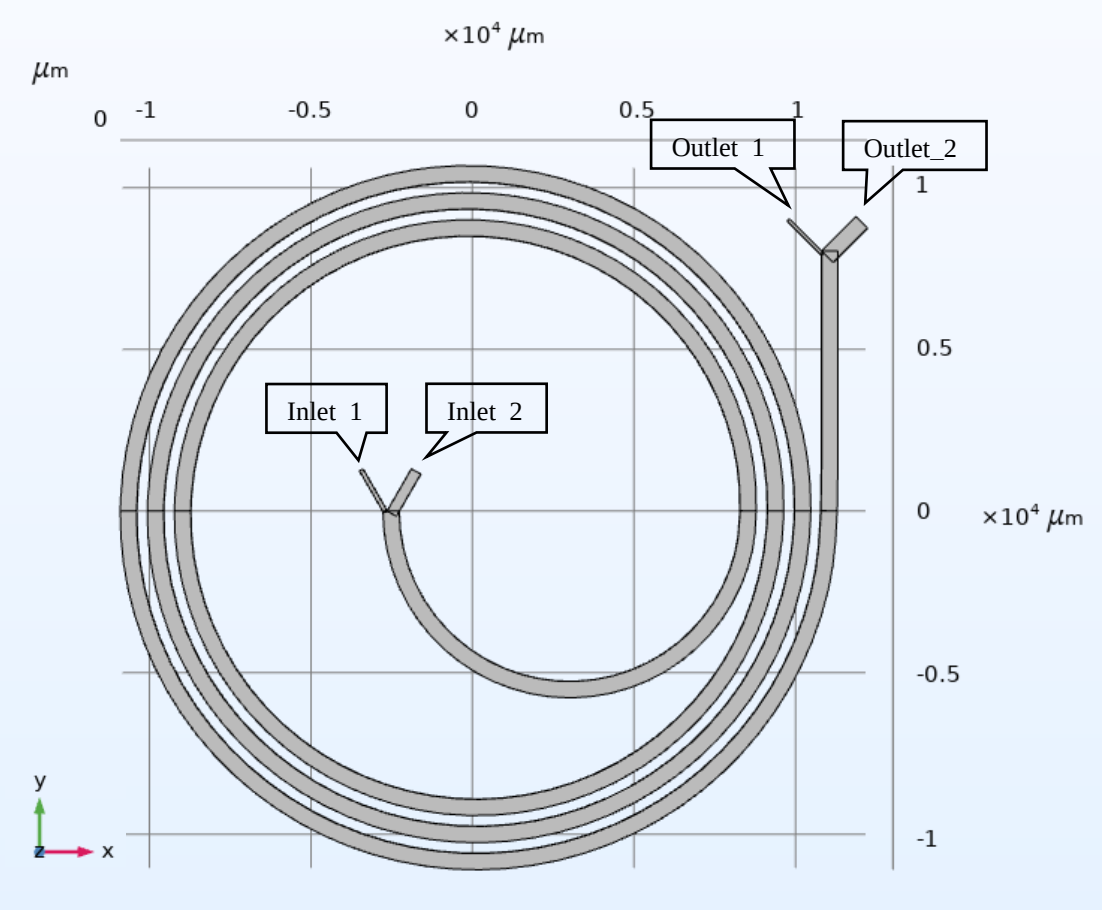

Figure 3.6: Schematic representation of the geometry of chip_5. The geometry consists of a semicircle, an Archimedean spiral, a line segment, and four rectangular prism blocks. Semicircular arc length, 17256 μm; parametric curve has three turns, and it is length,183790 μm; line segment length, 8000 μm; channel length, 209.046 mm; the length of the distance between two spiral channel, 333 μm; channel width 500 μm; the height of cannel inlet and outlets, 150 μm; the length of inlets and outlets, 1500 μm; width of the inlet_1, 125 μm; width of the inlet_2, 330 μm; the angle of the inlets with the y-axis, 30 degrees; width of the outlet_1, 100 μm, width of the outlet_2, 500 μm; the angle of the outlets with the y-axis, 45 degrees; semicircular arc radius, 5500 μm; initial spiral radius, 8500 μm; final spiral radius, 11000; initial angle, 0; final angle, 18.85; the growth rate of spiral, 132.63; volume, 1.5894e10 μm^3 ; surface area, 2.7646e8 μm^2; x minimum, -10833 μm; x maximum, 12165. μm; y minimum: -11042 μm; y maximum, 10626 μm; z minimum, -75 μm; z maximum, 75 μm.

3.3.2.3. Spiral Channel (1 Turn, 81.171 mm), Containing Sheath Flow (Re=108.46)

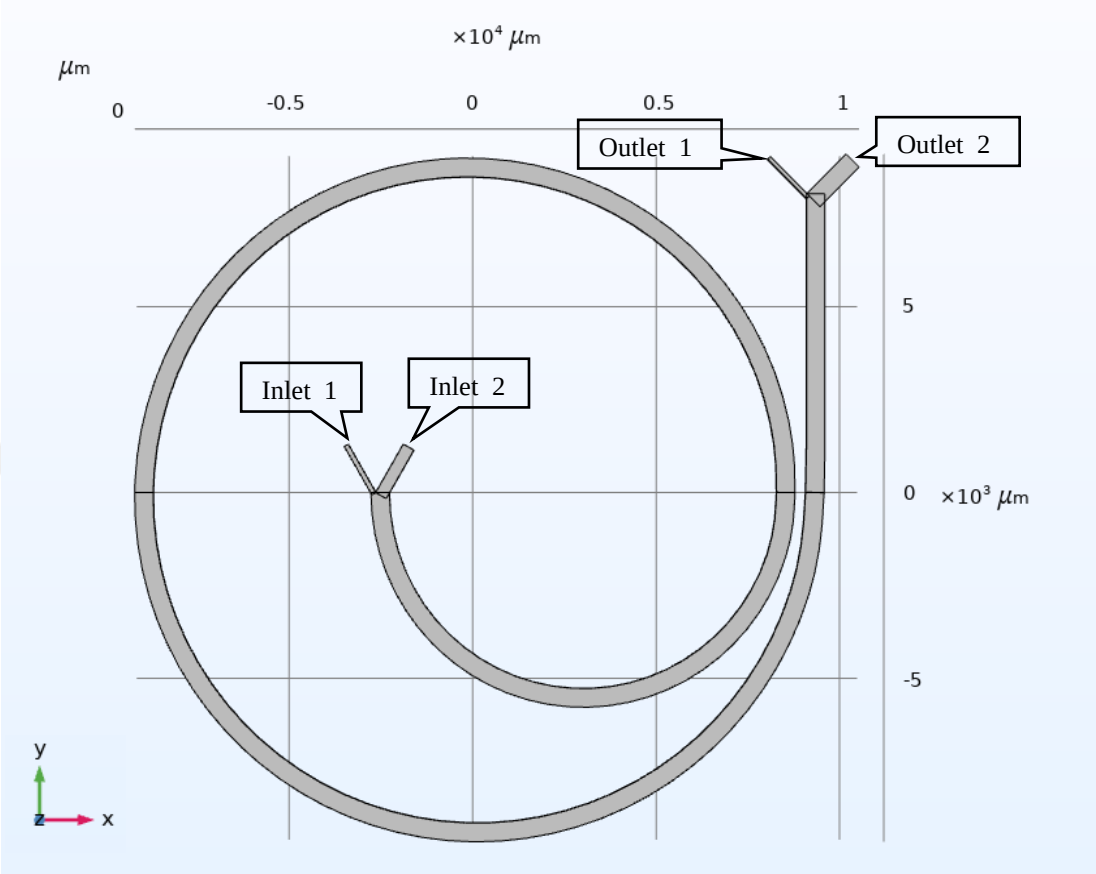

Figure 3.7: Schematic representation of the geometry of chip_6. The geometry consists of a semicircle, an Archimedean spiral, a line segment, and four rectangular prism blocks. Semicircular arc length, 17256 μm; parametric curve has a turn, and it is length, 55915 μm; line segment length, 8000 μm; channel length, 81.171 mm; the length of the distance between two spiral channel, 287.85 μm; channel width 500 μm; the height of the channel inlets and outlets, 150 μm; length of inlets and outlets, 1500 μm; width of the inlet_1, 125 μm; width of the inlet_2, 330 μm; the angle of the inlets with the y-axis, 30 degrees; width of the outlet_1, 100 μm, width of the outlet_2, 500 μm; the angle of the outlets with the y-axis, 45 degrees; semicircular arc radius, 5500 μm; initial spiral radius, 8500 μm; final spiral radius, 93000; initial angle, 0; final angle, 6.2832; the growth rate of spiral, 127.32; volume, 6.3049E9 μm^3; surface area, 1.1024E8 μm^2; x minimum, -9150 μm; x maximum, 10475 μm; y minimum: -9349.7 μm; y maximum, 9060.1 μm; z minimum, -75 μm; z maximum, 75 μm.

3.3.2.4. Spiral Channel (10 Turns, 748.305 mm, Re=13.13)

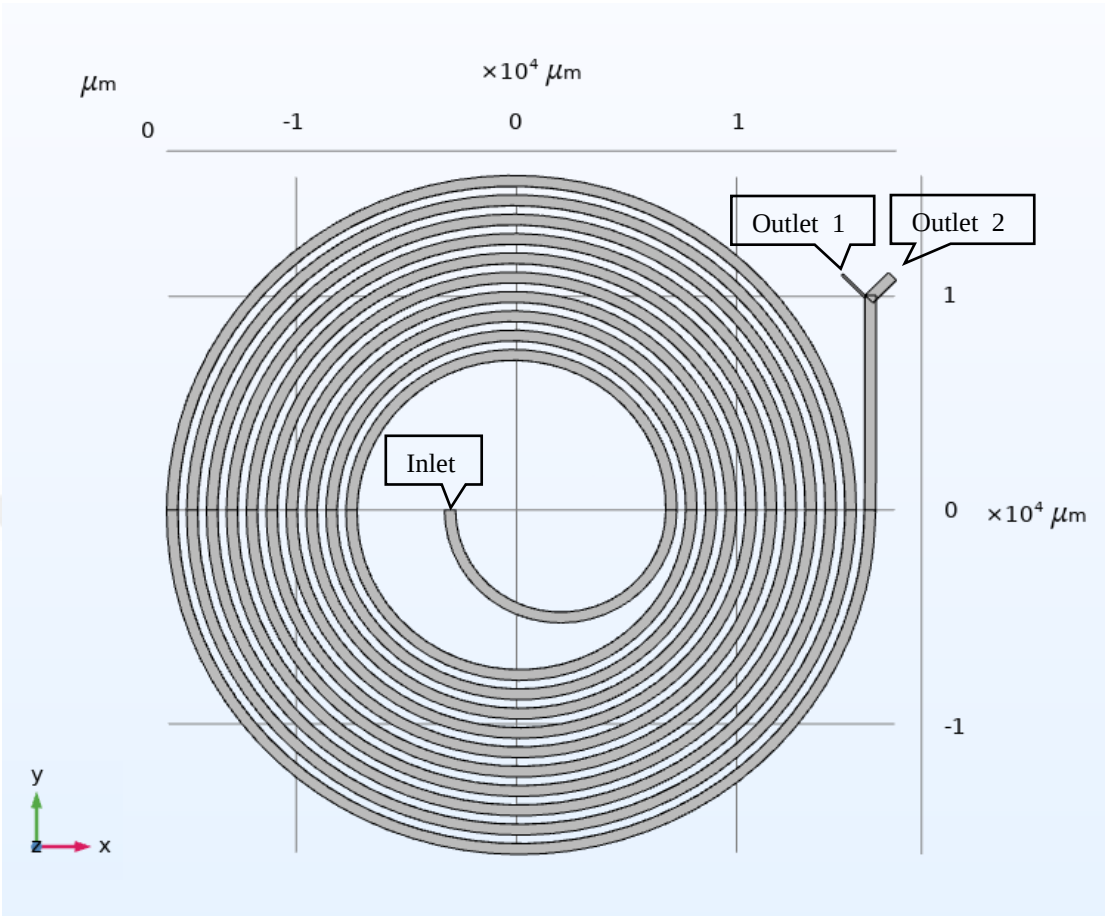

Figure 3.8: Schematic representation of the geometry of chip_7. The geometry consists of a semicircle, an Archimedean spiral, a line segment, and two rectangular prism blocks. Semicircular arc length, 15705 μm; parametric curve has ten turns, and it is length, 722600 μm; line segment length, 10000 μm; channel length, 748305 μm; the length of the distance between two spiral channel, 405.157 μm; channel width, 500 μm; the height of inlets and outlets, 150 μm; the length of inlets and outlets, 1500 μm; width of the inlet 500 μm; width of the outlet_1, 150 μm, width of the outlet_2, 500 μm; the angle of the outlets with the y-axis, 45 degrees; semicircular arc radius, 5000 μm; initial spiral radius, 7000 μm; final spiral radius, 16000; initial angle, 0; final angle, 62.832; the growth rate of spiral, 143.24; volume, 5.6236E10 μm^3; surface area, 9.7527E8 μm^2; x minimum, -15800 μm; x maximum, 17166 μm; y minimum: -16024 μm; y maximum, 15575 μm; z minimum, -75 μm; z maximum, 75 μm.

3.3.2.5. Spiral Channel (3 Turns, 177.885 mm, Re=69.23)

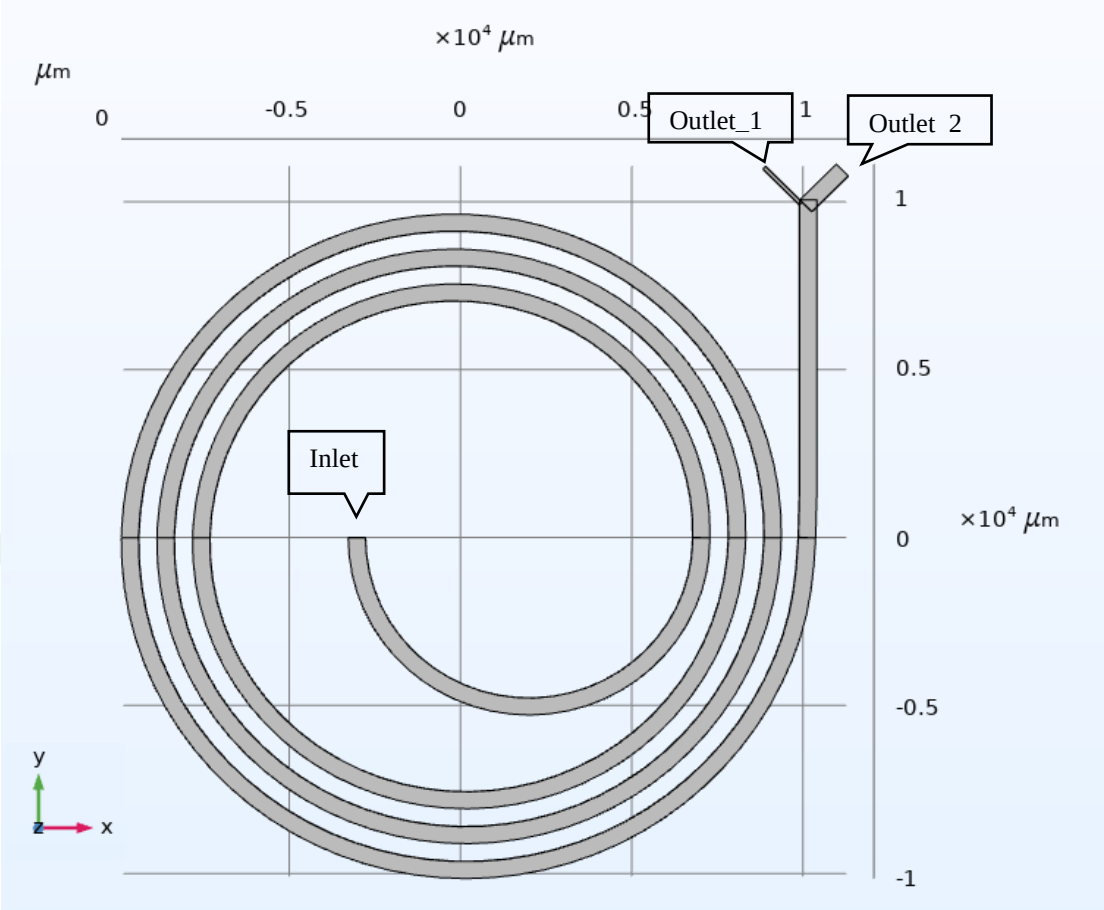

Figure 3.9: Schematic representation of the geometry of chip_8. The geometry consists of a semicircle, an Archimedean spiral, a line segment, and two rectangular prism blocks. Semicircular arc length, 15705 μm; parametric curve has three turns, and it is length, 161180 μm; line segment length, 10000 μm; channel length, 177885 mm; the length of the distance between two spiral channel, 538.217 μm; channel width 500 μm; the height of inlets and outlets, 150 μm; the length of inlets and outlets, 1500 μm; width of the inlet 500 μm; width of the outlet_1, 100 μm, width of the outlet_2, 500 μm; the angle of the outlets with the y-axis, 45 degrees; semicircular arc radius, 500 μm; initial spiral radius, 7000 μm; final spiral radius, 10100; initial angle, 0; final angle, 18.85; the growth rate of spiral, 164.46; volume, 1.4134E10 μm^3; surface area, 2.4549E8 μm^2; x minimum, -9833.4 μm; x maximum, 11264 μm; y minimum: -10092 μm; y maximum, 11060 μm; z minimum, -75 μm; z maximum, 75 μm.

3.3.2.6. Spiral Channel (3 Turns, 177.885 mm, Re=108.46)

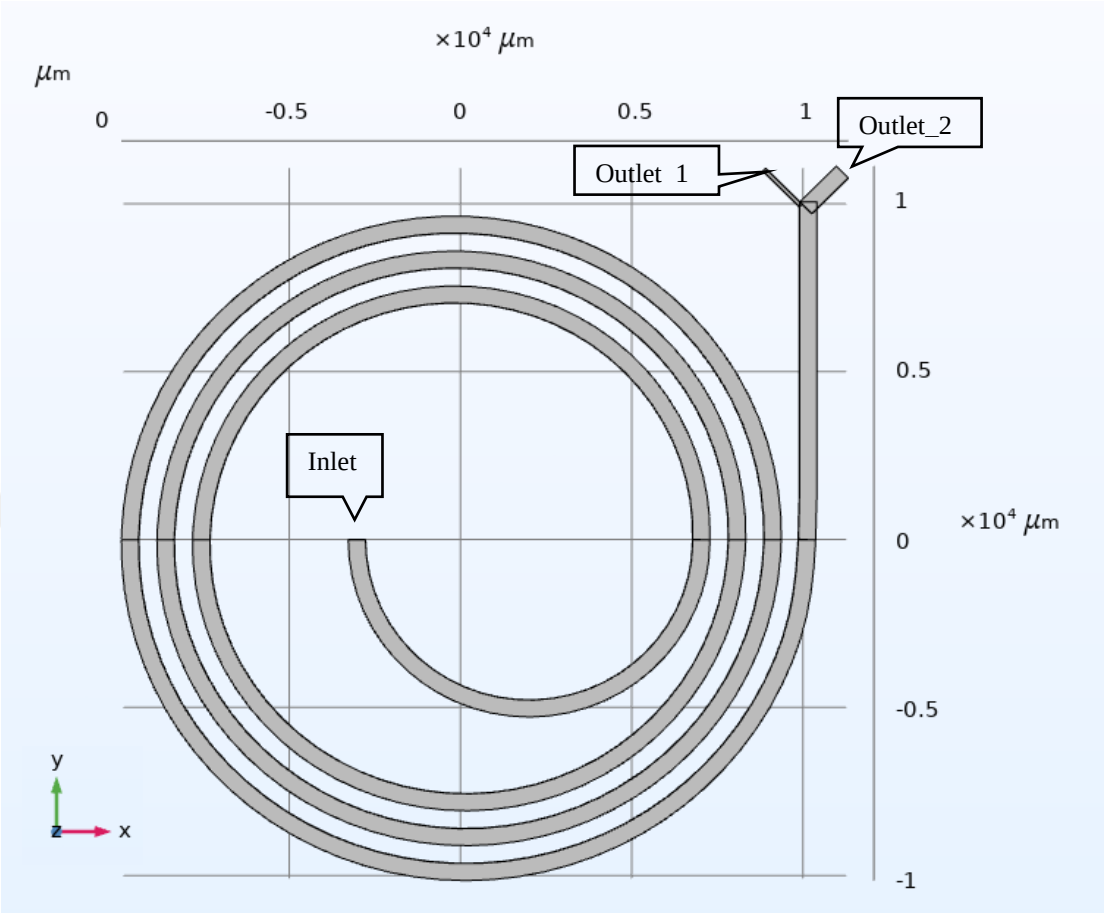

Figure 3.10: Schematic representation of the geometry of chip_9. The geometry consists of a semicircle, an Archimedean spiral, a line segment, and two rectangular prism blocks. Semicircular arc length, 15705 μm; parametric curve has three turns, and it is length, 161180 μm; line segment length, 10000 μm; channel length, 177885 mm; the length of the distance between two spiral channel, 538.217 μm; channel width 500 μm; the height of inlets and outlets, 150 μm; the length of inlets and outlets, 1500 μm; width of the inlet 500 μm; width of the outlet_1, 100 μm, width of the outlet_2, 500 μm; the angle of the outlets with the y-axis, 45 degrees; semicircular arc radius, 500 μm; initial spiral radius, 7000 μm; final spiral radius, 10100; initial angle, 0; final angle, 18.85; the growth rate of spiral, 164.46; volume, 1.4134E10 μm^3; surface area, 2.4549E8 μm^2; x minimum, -9833.4 μm; x maximum, 11264 μm; y minimum: -10092 μm; y maximum, 11060 μm; z minimum, -75 μm; z maximum, 75 μm.

4. RESULTS and DISCUSSION

This section of the thesis represents the results of the particle tracing simulations. The flow field was simulated by using COMSOL Multiphysics. A computational model was developed, and the results were compared with the literature. The migration of the particles within the channel is the result of the inertial lift force and Dean drag force in the flow field. The streamlines of the particles on the top view of the six chips are shown to observe the difference between these two forces., respectively. Dean flow patterns of several cross-sections in six different spiral channels were conducted and compared with each other to decide which chips are efficient to separate target particles from others.

4.1. Spiral Channel (8 Turns, 492.165 mm) Containing Sheath Flow (Re=13.13)

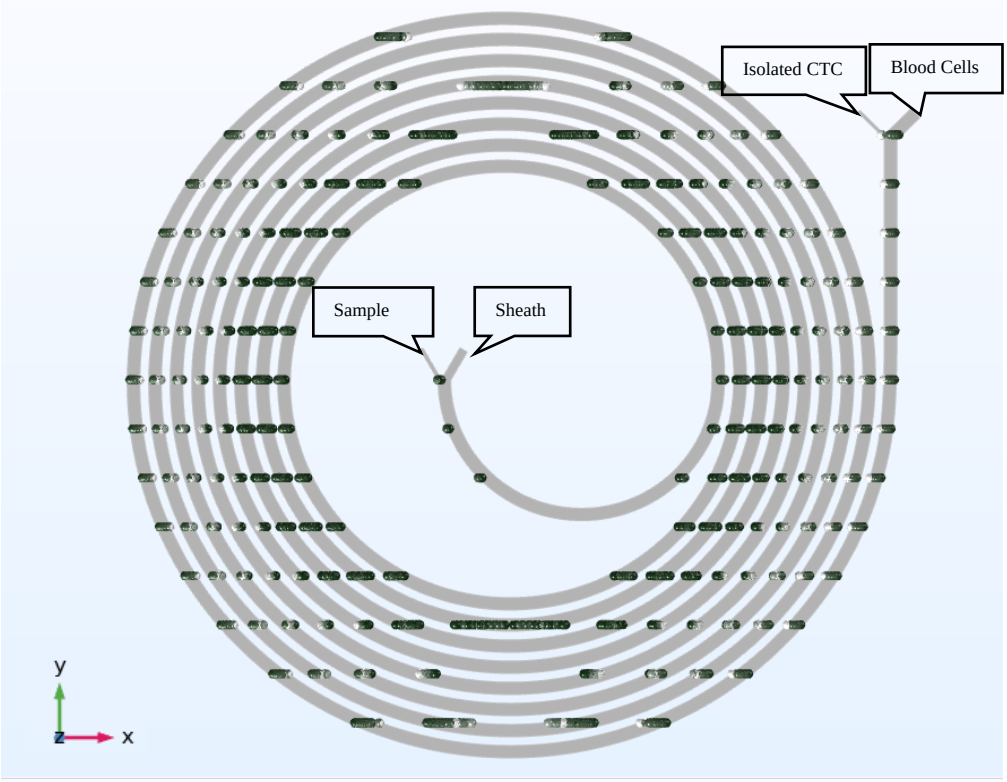

Figure 4.1: View of the particles from the top surface of the chip_4. The particles located on the cutting planes determined with 2000 μm intervals on the x-axis and y-axis, which represent the width and height of the channel, respectively.

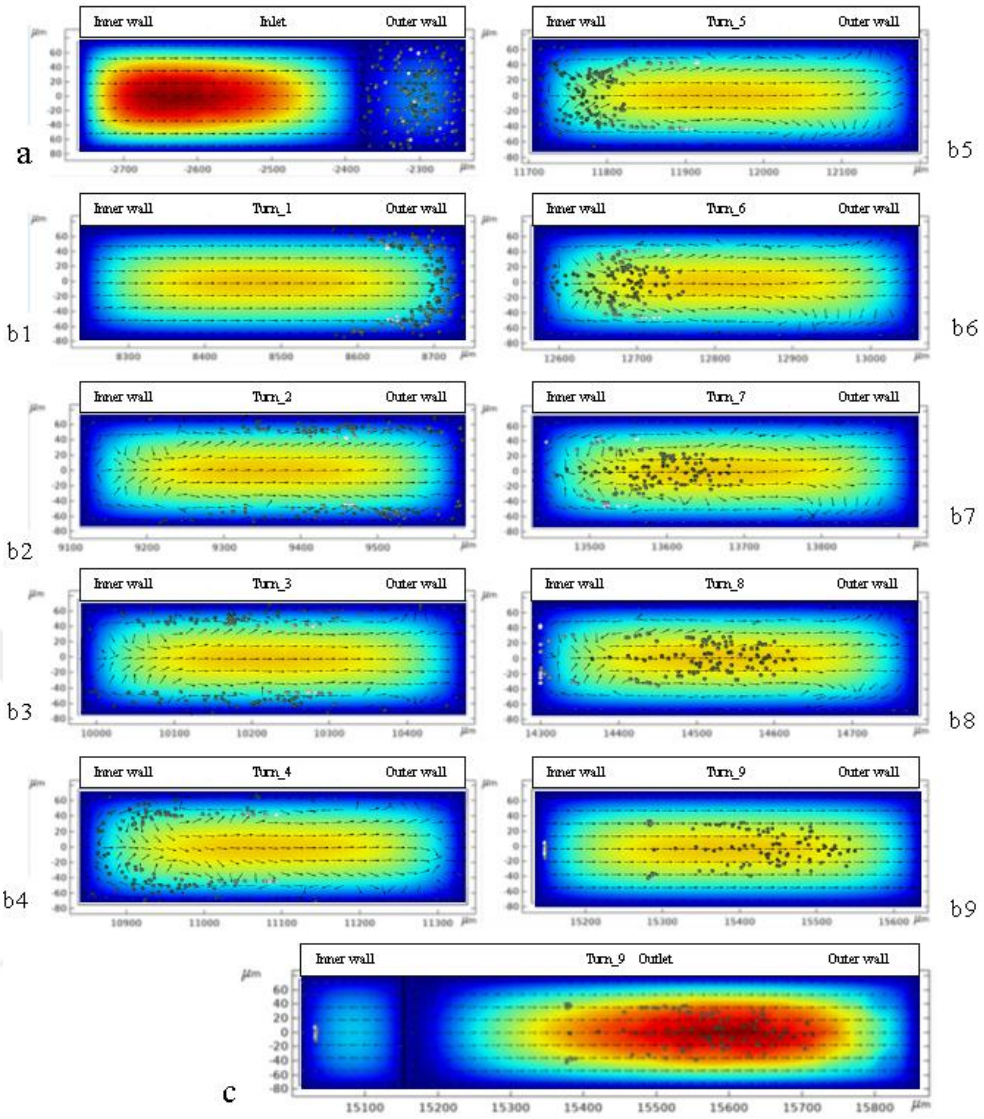

4.2: 4.2a). A close-up view of randomly dispersed particles in the inlet. 4.2b_1, 4.2b_2, 4.2b_3, 4.2b_4, 4.2b_5, 4.2b_6, 4.2b_7,4.2b_8, and 4.2b_9). A close-up view of particles on the cut planes, which are 130 μm away from the center of the channel through the y-axis, represented in each channel turn was shown respectively. 4.2c) A close-up view of the focused particles in the outlet. The random distribution option was used as the inlet position. 11different sized particles, two particles for each different sized CTC, and 20 particles for each different sized blood cells (a total of 148 particles) were simulated. White particles represent the CTCs (40, 35, 30, 25 μm); dark green particle represent blood cells (15, 10, 8, 7, 6, 3, 1 μm). All particles were released into inlet_1, at the same time. The buffer is injected into inlet_2. Flow velocity for inlet_1, 0.01 m/s so flow rate for inlet_1, 0.11 ml/min; flow velocity for inlet_2, 0.04 m/s, so flow rate for inlet_2, 0.12 ml/min. The simulated channel Reynolds number, 13.13. The first color legend_1 demonstrates particle size scale at the micrometer level. The black arrows show the direction of the Dean flow that makes the particles move. The arrow size of the velocity vector in the figure is normalized.

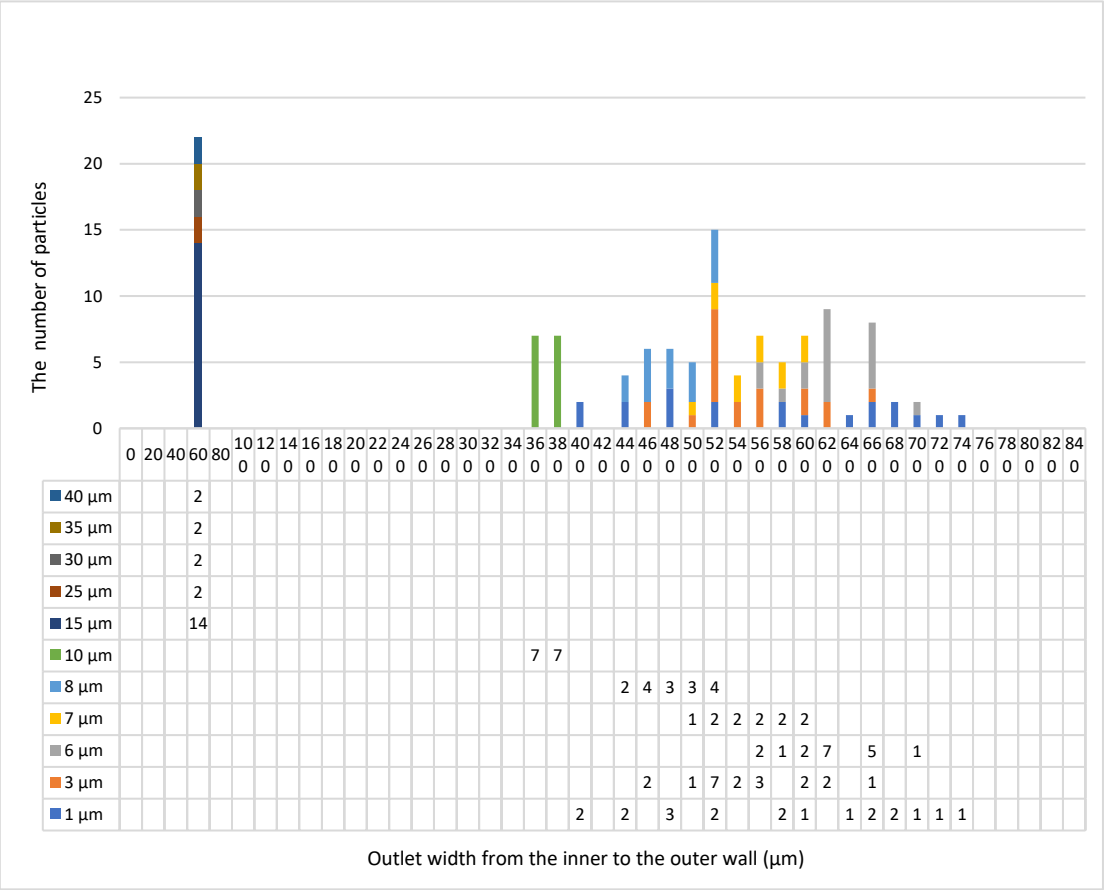

Figure 4.3: Particle distribution at the outlet in the width direction for the spiral channel, containing sheath flow with Reynolds number 13.13.

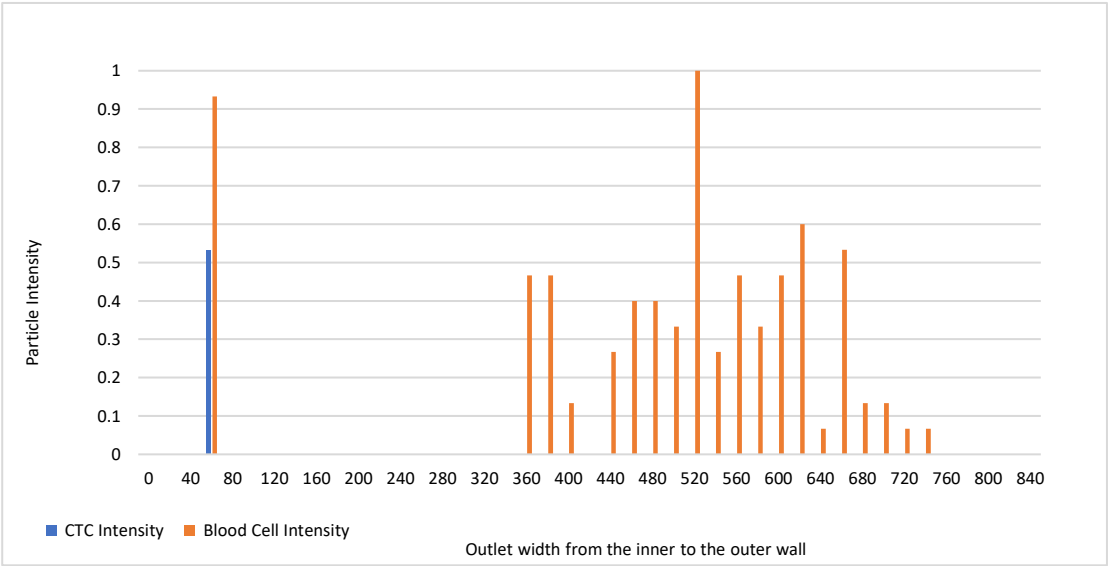

Figure 4.4: Column-scan is indicating the normalized distribution of CTCs and blood cells at the outlet for the spiral channel, containing sheath flow with Reynolds number 13.13.

The purpose of this simulation is to show how the sheath flow affects the Dean flow. Dean flow occurs due to the spiral of the channel and affects the particle movement within the channel. The real-time computing we assigned to the program for separation was 50 seconds. The collected particle in outlets remained the same amount after the ~ 49.7th second. That shows us the minimum time for simulation. As a result of the simulation, we showed the movement of the particles by the top view of the channel in figures 4.2. According to simulation results, the blood cells with a diameter of 10 microns and smaller turned to outlet_2 and came out, and all of CTCs focused and came out of outlet_1. 15 μm particles, which are the largest white blood cells, moved together with 25 μm particles and focused on the same streamlines than come from outlet_1, as shown in figure 4.2.

The flow rate at the inlet_2 is approximately ten times higher than at the inlet_1. Therefore, sheath flow coming from inlet_2 pushed the particles to the walls of the channel, as shown in figure 4.2b_1, describing the first turn of the channel. In the second turn, the sheath flow penetrated well among the particles, allowing the particles to have been positioned on the upper and lower surfaces of the channel. Besides, sheath flow pushed the particles, providing them with the effect of the Dean flow direction. As shown in figure 4.2b_2, small (dark green) particles are more affected by sheath flow due to their low mass, so we can say that they were less resistant to this flow.
When we looked at the 4.2b_3, 4.2b_4, and 4.2b_5, sheath flow continued to push small(green) particles more and compressed them through the inner wall, at the same time, more massive (white) particles were also pushed by sheath flow but, they were slightly affected. They were positioned just in the middle of the lower and upper surfaces of the channel until the moment. When we looked at the figure, 4.2b_6, 4.2b_7, 4.2b_8, and 4.2b_9, sheath flow pushed the particles, which are 10 microns and smaller than 10 microns, into the center of the channel, following Dean flow direction. Larger particles migrate more slowly because of applying more resistance to the sheath flow so, and they traveled towards the inner wall of the channel during the simulation. The line determines the separation line of the two outlets determined in figure 4.2c.

Figure 4.3 shows us the approximate positions of the particles at the end of the channel. The particles with a diameter of 40, 35, 30, 25, and 15 microns have come

out of outlet_1, focusing on a single point. The particles with a diameter of 10, 8, 7, 6, 3, 1-microns particles have come out of the outlet_2. In the outlet_2, all particles were lined up from large to small, from the inner wall to the outer wall. However, the particles with a diameter of one-micron were located randomly in the center of the channel.

In general, when we examined the motion of particles by looking at the vertical cross-section of the channel, we realized that there was a specific path where the particles fallowed. Since small particles were significantly affected by sheath flow, they completed this path faster. As the radius of the particle is reduced, the effect of the sheath flow on particles has increased. Our goal was to collect 40, 35, 30, and 25-micron particles together. As shown in figure 4.4, which describes particle intensity, it prevented us from achieving our goal by acting with these particles in 15-micron particles. Particles with a diameter of 15 can prevent the appearance of cancer cells due to their size and amount. Therefore, we continued our simulations by increasing the flow rate and shortening the channel.

4.2. Spiral Channel (3 Turns, 209.046 mm) Containing Sheath Flow (Re=39.23)

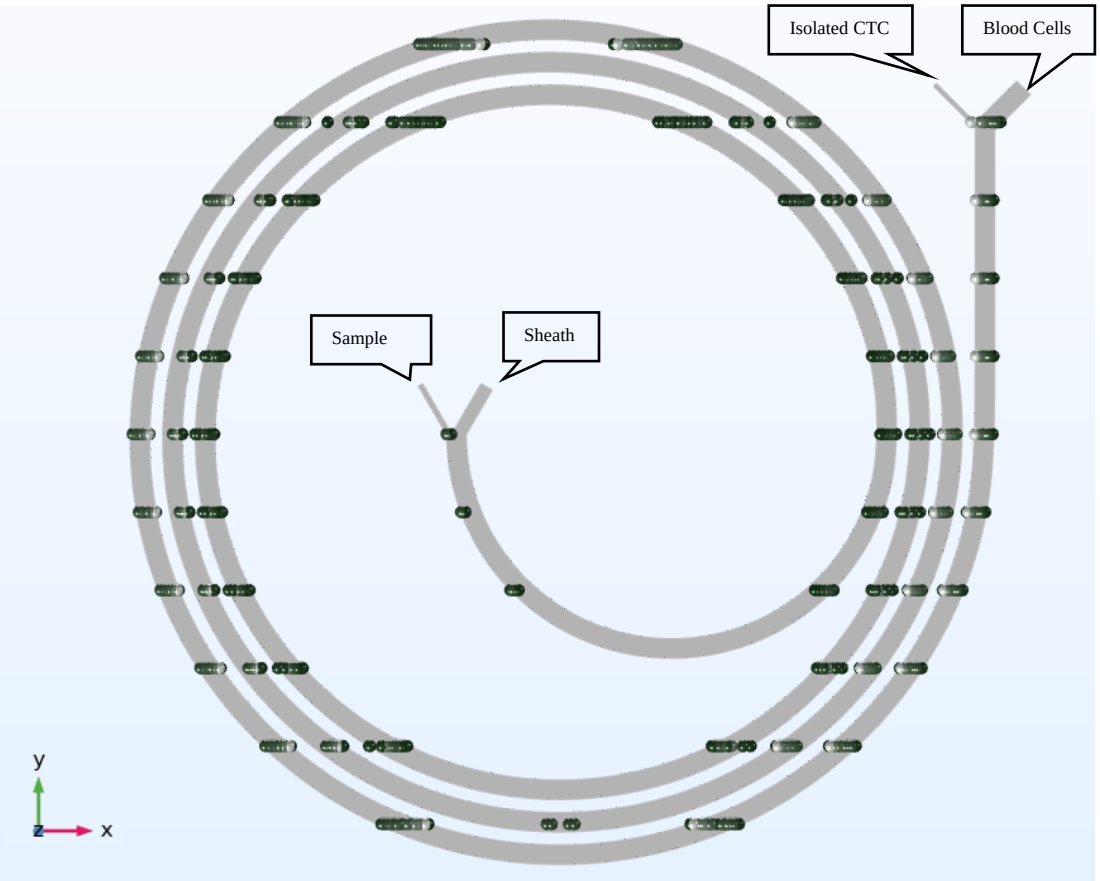

Figure 4.5: View of the particles from the top surface of the chip_5. The particles located on the cutting planes determined with 2000 μm intervals on the x-axis and y-axis, which represent the width and height of the channel, respectively. 11different sized particles, two particles for each different sized CTC, and 20 particles for each different sized blood cells (a total of 148 particles) were simulated. White particles represent the CTCs (40, 35, 30, 25 μm); dark green particles represent blood cells (15, 10, 8, 7, 6, 3, 1 μm). All particles were released into inlet_1, at the same time. The buffer is injected into inlet_2. Flow velocity for inlet_1, 0.06 m/s so flow rate for inlet_1, 0.067 ml/min; flow velocity for inlet_2, 0.24 m/s so flow rate for inlet_2, 0.71 ml/min . The simulated channel Reynolds number, 39.23

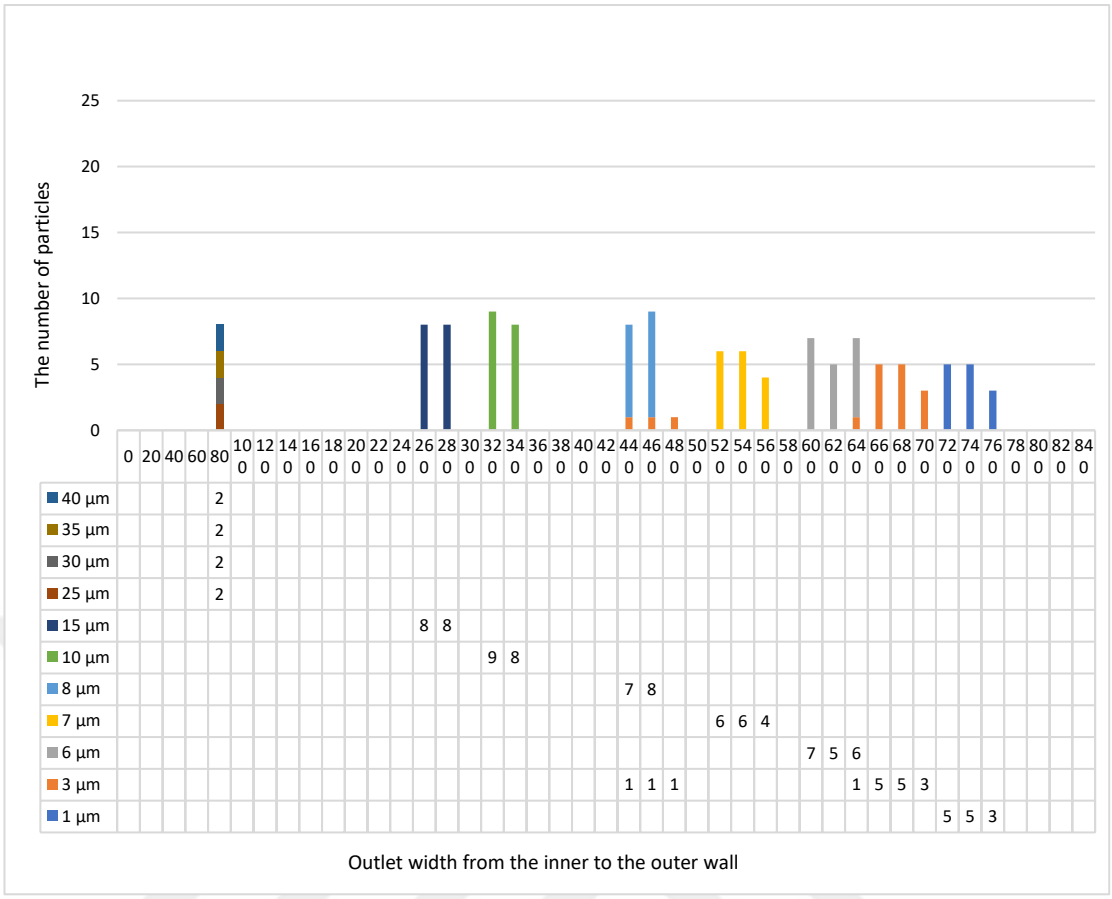

Figure 4.6: Particle distribution at the outlet in the width direction for the spiral channel, containing sheath flow with Reynolds number 39.23.

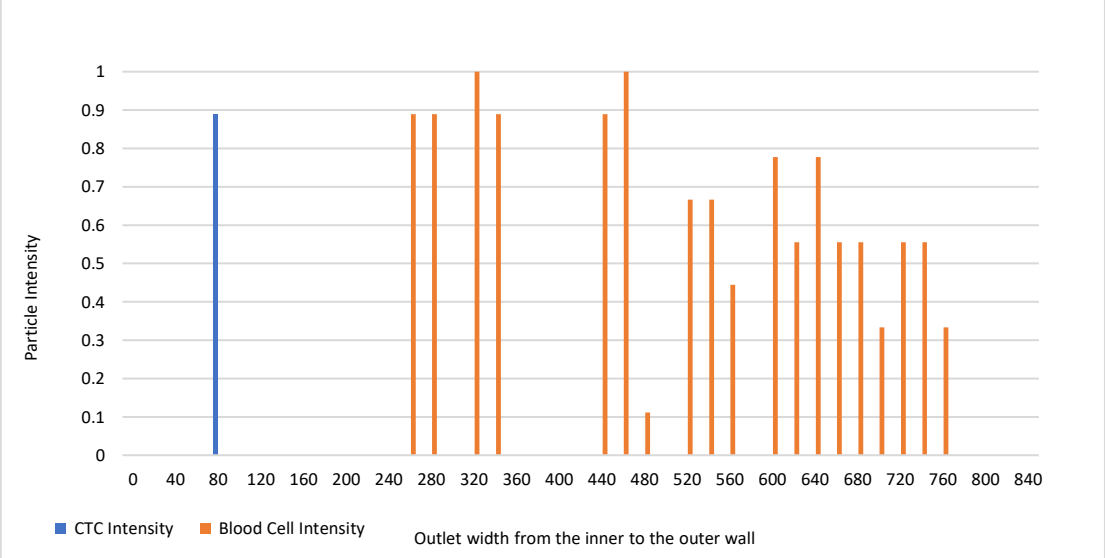

Figure 4.7: Column-scan is indicating the normalized distribution of CTCs and blood cells at the outlet for the spiral channel, containing sheath flow with Reynolds number 39.23.

This simulation was made based on the result of the simulation shown in figure 4.3. In this simulation, the separation of particles with a diameter of 15 microns and a small diameter of 25 microns and a field of large diameter is aimed. The time we assigned to the program for the separation of 148 particles according to the size difference was 5 seconds. The particle number come out from outlets remained the same after the 3.29th second. At the end of the simulation, the blood cells with a diameter of 15 microns and smaller came out from outlet_2. All of CTCs focused and came out of outlet_1.

When we increased the Reynolds number from 13.13 to 39.23 in this simulation, we observed that the pathway that the particles should follow could take place in a shorter channel. In the simulation, particles moved with being three groups. When we followed the channel turns in figure 4.5, respectively, we observed that particles with a diameter of 40, 35, 30, 25 microns move together, particles with a diameter of 15-micron acted alone. The smaller (dark green) particles were more affected by sheath flow. Thus, they easily controlled by sheath flow and went far away from larger particles. In the first turn, the dark green particles were pushed towards the surface of the channel easily by sheath flow. Therefore, they moved more closer to the surface of the channel, as expected. After that, with sheath flow kept going to push the particles, all particles moved harmoniously with the Dean flow direction. After the small particles moved from the surface of the channel and reached the inner wall, they turned upside down, moved to the center of the channel, and moved to the outer surface of the channel with following Dean flow, respectively. At that time, large particles have just reached to the inner surface of the channel; this moment is suitable for separating the particles. All CTCs were focused, and the distance between CTCs and blood cells was sufficient for segregation with a yield of 100 at the last turn.

Figure 4.6 shows us the approximate positions of the particles at the end of the channel from the inner wall to the other wall. The particle distribution at the outlet of the channel shown in figure 4.6 was made based on the simulation results. The intensity of CTCs and blood cells at the outlet of the channel shown in figure 4.7 was made based on figure 4.6. As shown in figures 4.6 and 4.7, the particles with a diameter of 40, 35, 30, and 25 microns have come out from outlet_1 by focusing on a single

point. The particles with a diameter of 15, 10, 8, 7, 6, 3, 1-microns particles have come out from the outlet_2.

4.3. Spiral Channel (1 Turn, 81.171 mm), Containing Sheath Flow (Re= 108.46)

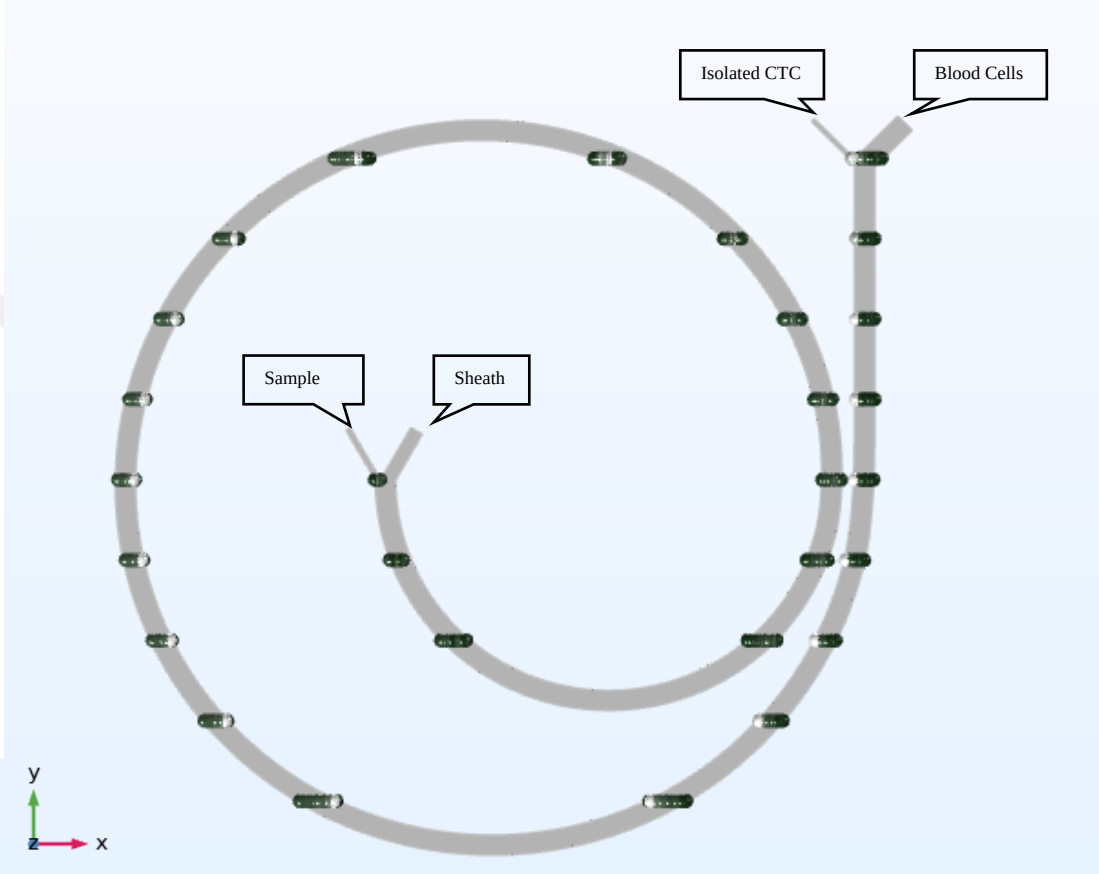

Figure 4.8: View of the particles from the top surface of the chip_6. The particles located on the cutting planes determined with 2000 µm intervals on the x-axis and y-axis, which represent the width and height of the channel, respectively.11different sized particles, two particles for each different sized CTC, and 20 particles for each different sized blood cells (a total of 148 particles) were simulated. White particles represent the CTCs (40, 35, 30, 25 µm); dark green particles represent blood cells (15, 10, 8, 7, 6, 3, 1 µm). All particles were released into the inlet_1, at the same time. The buffer is injected into inlet_2. Flow velocity for inlet_1, 0.15 m/s so flow rate for inlet_1, 0.17 ml/min; flow velocity for inlet_2, 0.65 m/s so flow rate for inlet_2, 1.91 ml/min. The simulated channel Reynolds number, 108.46.

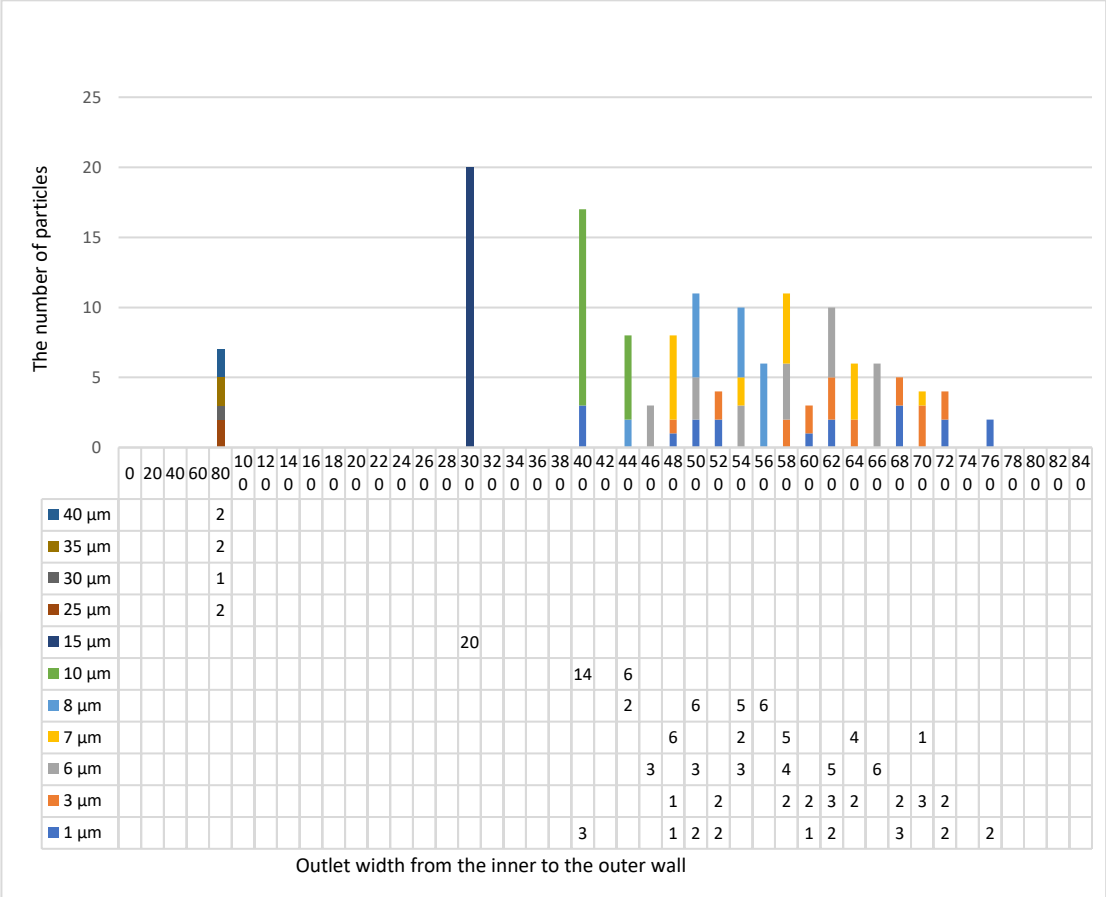

Figure 4.9: Particle distribution at the outlet in the width direction for the spiral channel, containing sheath flow with Reynolds number 108.46.

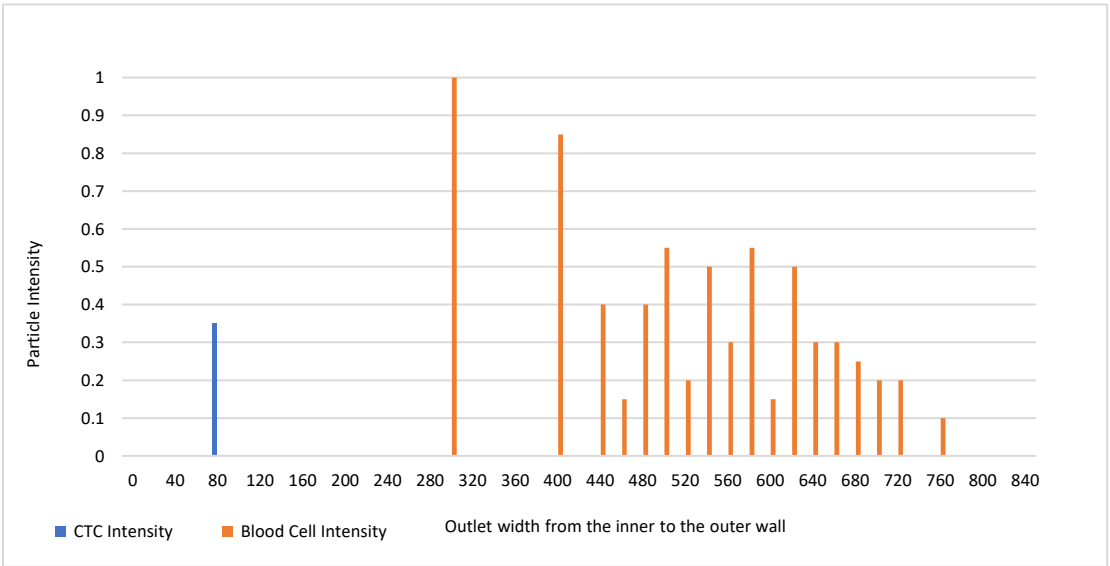

Figure 4.10: Column-scan is indicating the normalized distribution of CTCs and blood cells at the outlet for the spiral channel, containing sheath flow with Reynolds number 108.46.

This simulation is the simulation with the largest Reynolds number with a value of 108.4 among simulations containing sheath flow, as shown in figure 4.8. In this simulation, we examined the effect of Reynolds number around 100 on particle separation. The time we assigned to the program for the separation of 148 particles according to the size difference was 1 second. The particle number come out from outlets remained the same after the 0.73rd second. When we compare three simulations containing sheath flow, this was the simulation that achieved particle focusing in the shortest time thanks to had the largest Reynolds number. Besides, a turn length of the spiral was sufficient for the separation of particles. Figure 4.9 shows each particle distribution at the outlet, created by taking a vertical section at the outlet of the channel. Figure 4.10 allowed us to classify the particles precisely by type. As seen in figure 4.10, no particles representing any blood cells have emerged from the channel where the particles representing the cancer cells come out. At the same time, no particles representing any cancer cells emerged from the channel where the particles representing blood cells came out, and the particles were separated from each other by one hundred percent purity.

4.4. Spiral Channel (10 Turns, 748.305 mm, Re=13.13)

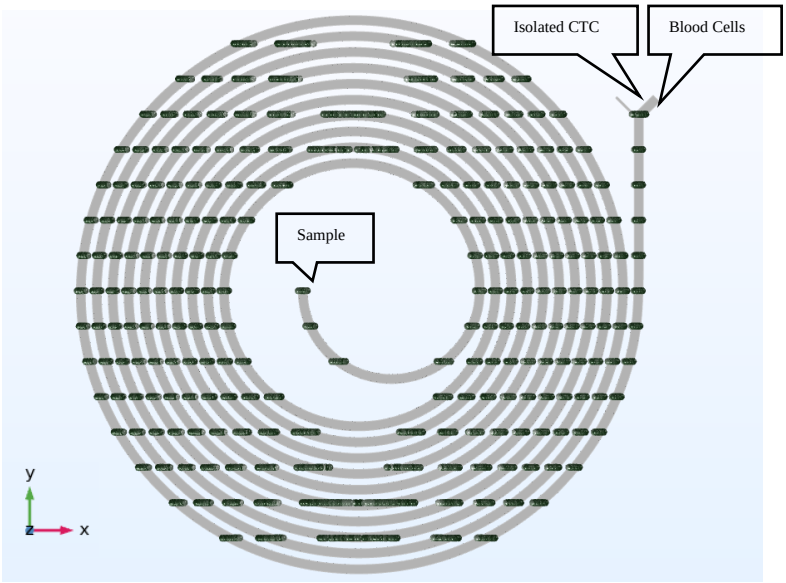

Figure 4.11: View of the particles from the top surface of the chip_7. The particles located on the cutting planes determined with 2000 intervals on the x-axis and y-axis, which represent the width and height of the channel, respectively.

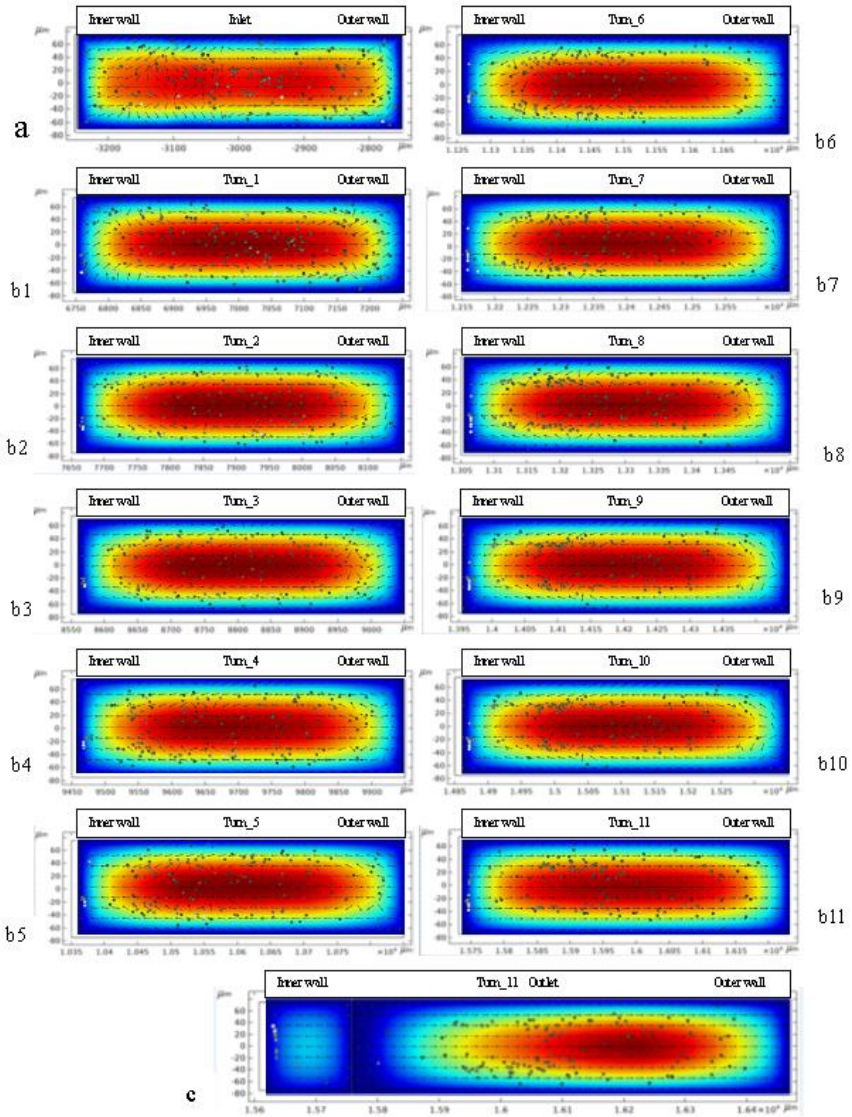

4.12: 4.12a) A close-up view of randomly dispersed particles on the cut plane, which 50 μm away from the inlet of the channel through the (-) y-axis in the inlet. 4.12b_1, 4.12b_2, 4.12b_3, 4.12b_4, 4.12b_5, 4.12b_6, 4.12b_7, 4.12b_8, 4.12b_9, 4.12b_10, 4.12b_11) A close-up view of particles on the cut planes, which are 145 μm away from the center of the channel through the y-axis, in each channel turn, respectively. 4.12c) A close-up view of the focused particles in the outlets. The random distribution option was used as the inlet position. 11different sized particles, two particles for each different sized CTC, and 20 particles for each different sized blood cells (a total of 148 particles) were simulated. White particles represent the CTCs (40, 35, 30, 25 μm); dark green particles represent blood cells (15, 10, 8, 7, 6, 3, 1 μm). All particles were released into the inlet at the same time. The flow velocity for inlet, 0.057 m/s, so the flow rate for inlet, 0.256 ml/min. The simulated channel Reynolds number, 13.13. The first color legend_1 demonstrates particle size scale at the micrometer level. The black arrows show the direction of the Dean flow that makes the particles move. The arrow size of the velocity vector in the figure is normalized.

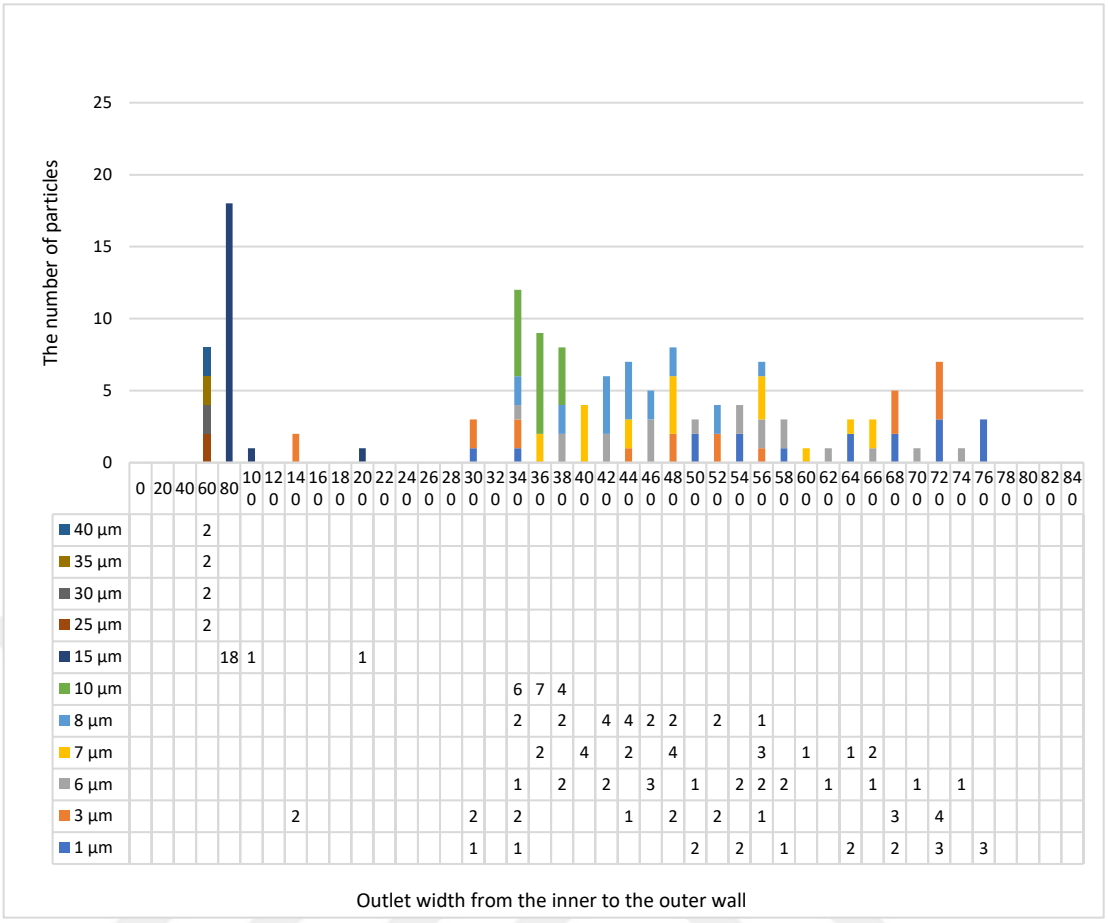

Figure 4.13: Particle distribution at the outlet in the width direction for the spiral channel, with Reynolds number 13.13.

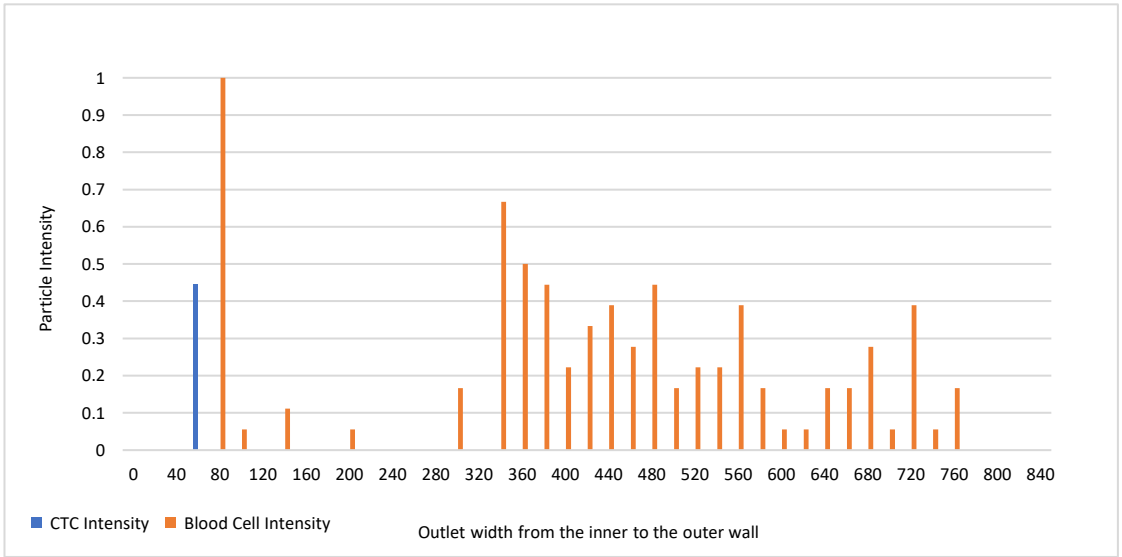

Figure 4.14: Column-scan is indicating the normalized distribution of CTCs and blood cells at the outlet for the spiral channel, with Reynolds number 13.13.

The purpose of this simulation is to show how the Dean flow due to the spiral of the channel affects the particle movement within the channel. The time we assigned to the program for simulation was 60 seconds. The particle number that comes out from outlets remained the same after the 50.20^{th} second. That shows us the minimum time for simulation. As a result of the simulation, we showed the movement of the particles by the top view of the channel in figures 4.11. According to results, the blood cells with a diameter of 10 microns and smaller came out of outlet_2, and all of CTCs focused and came out of outlet_1. 15 μm particles, which are larger white blood cells, moved together with 25 μm particles and focused on the same streamlines, and all of the 15 μm particles except one came out from otlet_1.

Also, two blood cells with a diameter of 1 micron came with CTCs to outlet_1, as shown in figure 4.13. If we first analyzed the movement of particles with a diameter of 15 microns and larger from inlet to outlet. When we fallow the figures from figure 4.12a to figure 4.12c, After the particles entered the channel, in time, they proceeded in the direction of the inner wall of the channel with the effect of the drag force dominating regularly. Drag force orientated the particles to settle them to their balanced position. The position of some particles (15 microns and larger) in the inlet was randomly located near to the outer of the channel wall. In time, although it has a long way to reach equilibrium than the particles (15 microns and larger), which were randomly located near the inner wall at the inlet of the channel, all did the same movement. Therefore, all settled in the same location on the x-axis. It is observed that, if the particle has sufficient size and the flow conditions are suitable, the equilibrium positions will be the same on at least a particular axis regardless of the initial position of the particle. Figure 4.13, which is made by analyzing figure 4.11, shows the distribution of particles of different diameters along the channel. Figure 4.14 shows the particle intensity at the channel outlet in the width of the channel. When we analyzed figure 4.13 and 4.14, we observed that the particles with a diameter of one-micron were scattered randomly along the channel when they came to the outlet, they were far from reaching the equilibrium position. However, the particles with a diameter of 10, 8, 6, 3-microns were ordered from large to small, from left to right along the x-axis, respectively, in the outlet with the effect of Dean flow in time. Particles with a diameter of 25-microns and larger (white), although they have the

largest diameter, performed almost the same movement as particles with a diameter of 15 microns (green).

For this reason, we could not separate the particles representing white blood cells with a diameter of 15 microns from particles representing cancer cells with a diameter of 25 microns or larger. The 18 blood cells shown in figure 4.12 are seen as the cell with the highest density in figure 4.14. This density will prevent cancer cells from being seen and will decrease the efficiency of the simulated chip. Thus we can say that simulation of the low Reynolds number, which is 13.13, is not efficient to separate our targets. Thereof, we continued with the simulation by increasing the flow rate we use.

4.5. Spiral Channel (3 Turns, 177.885 mm, Re= 69.23)

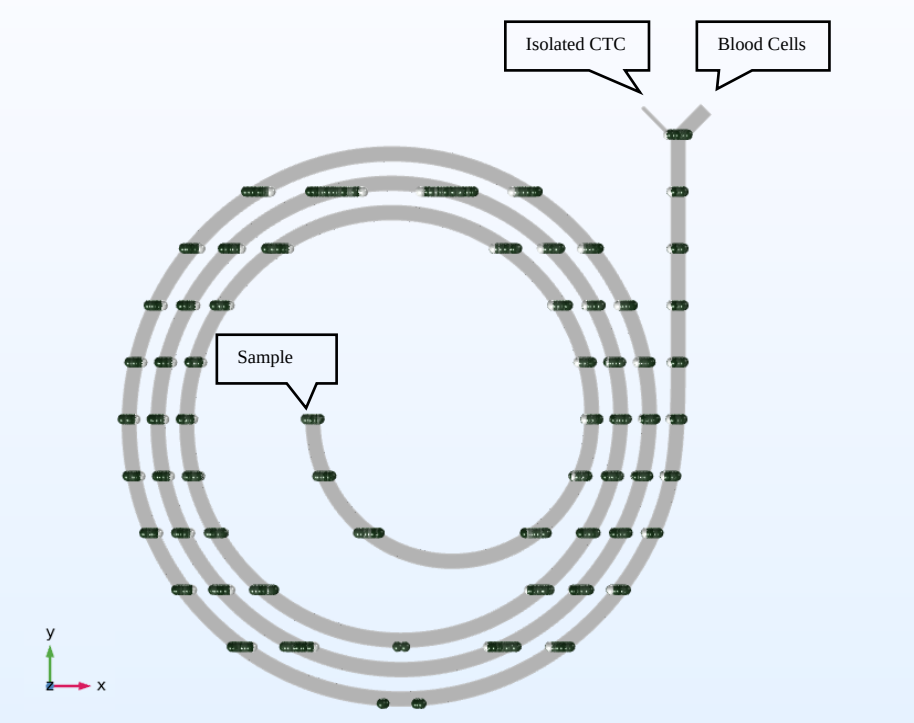

Figure 4.15: View of the particles from the top surface of the chip_8. The particles located on the cutting planes determined with 2000 μm intervals on the x-axis and y-axis, which represent the width and height of the channel, respectively. 11different sized particles, two particles for each different sized CTC, and 20 particles for each different sized blood cells (a total of 148 particles) were simulated. White particles represent the CTCs (40, 35, 30, 25 μm); dark green particles represent blood cells (15, 10, 8, 7, 6, 3, 1 μm). All particles were released into inlet, at the same time. Flow velocity for inlet, 0.3 m/s so flow rate for inlet, 1.35 ml/min. The simulated channel Reynolds number, 69.23.

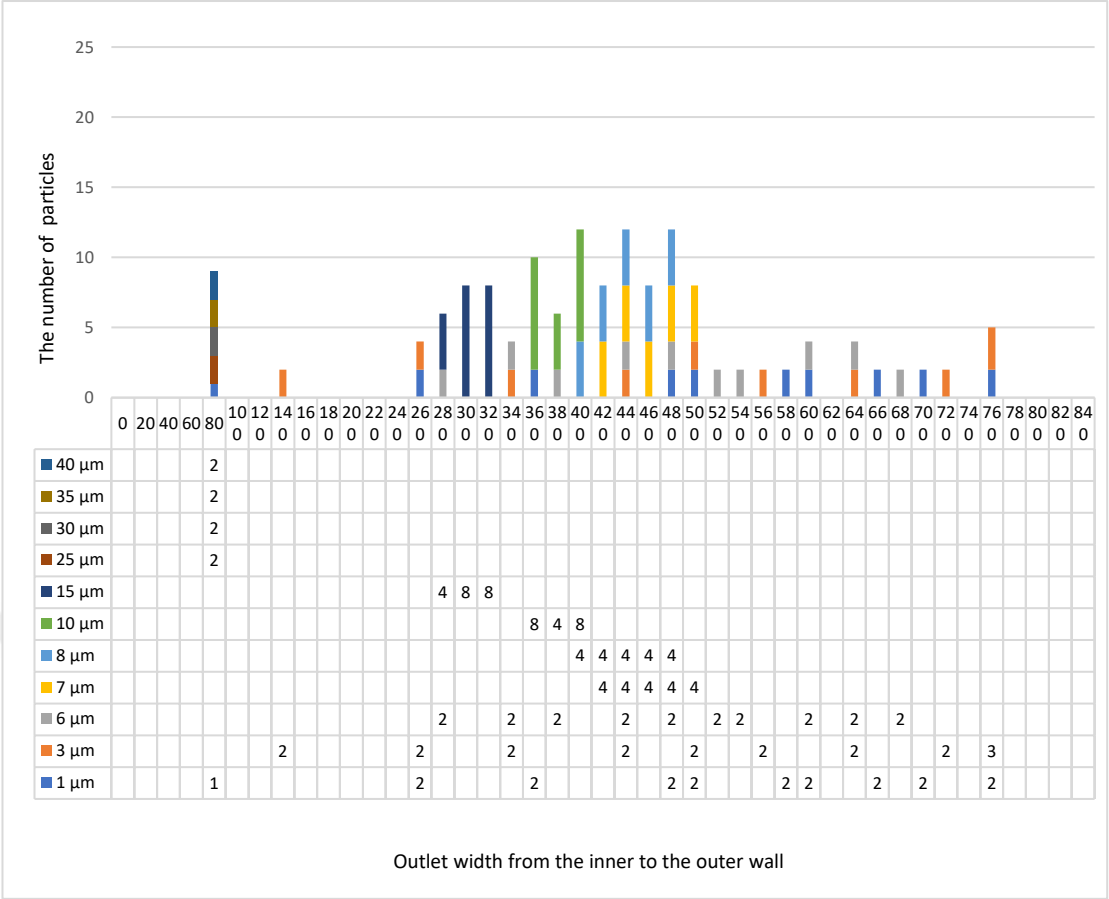

Figure 4.16: Particle distribution at the outlet in the width direction for the spiral channel, with Reynolds number 69.23.

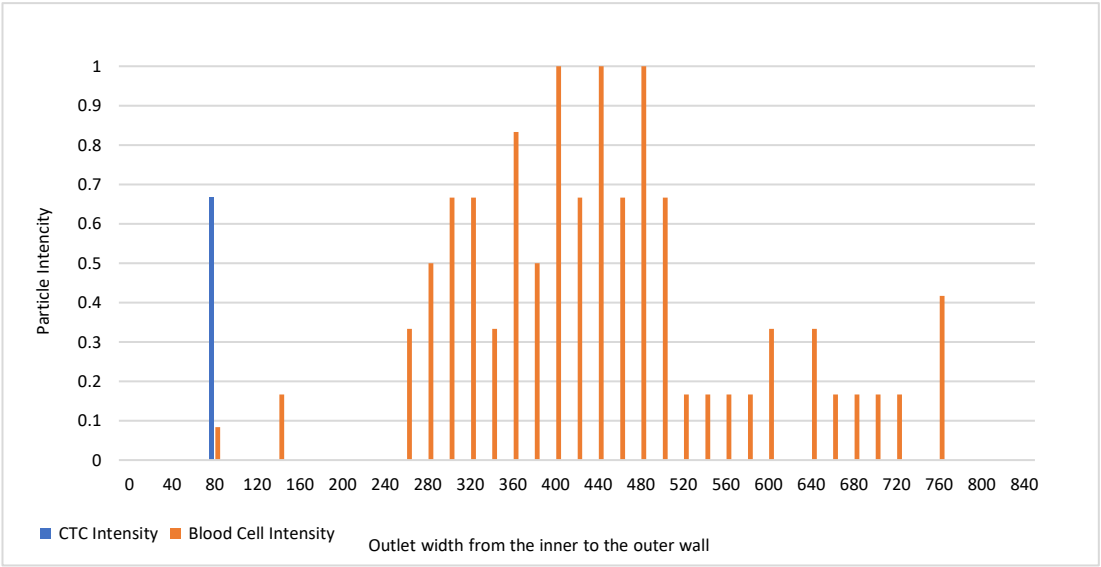

Figure 4.172: Column-scan is indicating the normalized distribution of CTCs and Blood cells at the outlet for the spiral channel, with Reynolds number 69.23.

In this simulation, we observed how the separation of particles would be when the channel's Reynolds number was 69.23 without sheath flow. The time we assigned to the program was 3 seconds. The particle number come out from outlets remained the same after the 1.6^{th} second. By analyzing these figure 4.15, indicating the movement of the particles on the top view of the channel with 2 mm interval cut-planes, we observed that the blood cells with a diameter of 15 microns and smaller turned to outlet_2 and came out. All CTCs came out of outlet_1by focusing, but also, two blood cells with a diameter of 1 micron came with CTCs to outlet_1. In this chip the used flow rate is 1.35 ml/min, we observe that the time it takes for the particles to cluster according to their size diameter, and the required channel length to particle focusing was decreased when compared with the chip_7.

Increasing the flow rate changed the focusing point of the most prominent white blood cells (green), allowing them to separate from CTCs. The particles with a diameter of 10, 8, 6, 3 microns were ordered from large to small as from left to right along the x-axis on the outlet. In this simulation, the particles of the same diameter increased the amount of clustering compared to the simulation of chip_7. Figure 4.16 shows the particle distribution at the channel outlet, and it helps us to observe all particles at the same time. Figure 4.17 shows the particle intensity. According to figure 4.16 and figure 4.17, even if blood cells with one and three microns in diameter, which are three in total, decrease their purity in the area where cancer cells are collected, they will not prevent the appearance of cancer cells.

4.6. Spiral Channel (3 Turns, 177.885 mm, Re= 108.46)

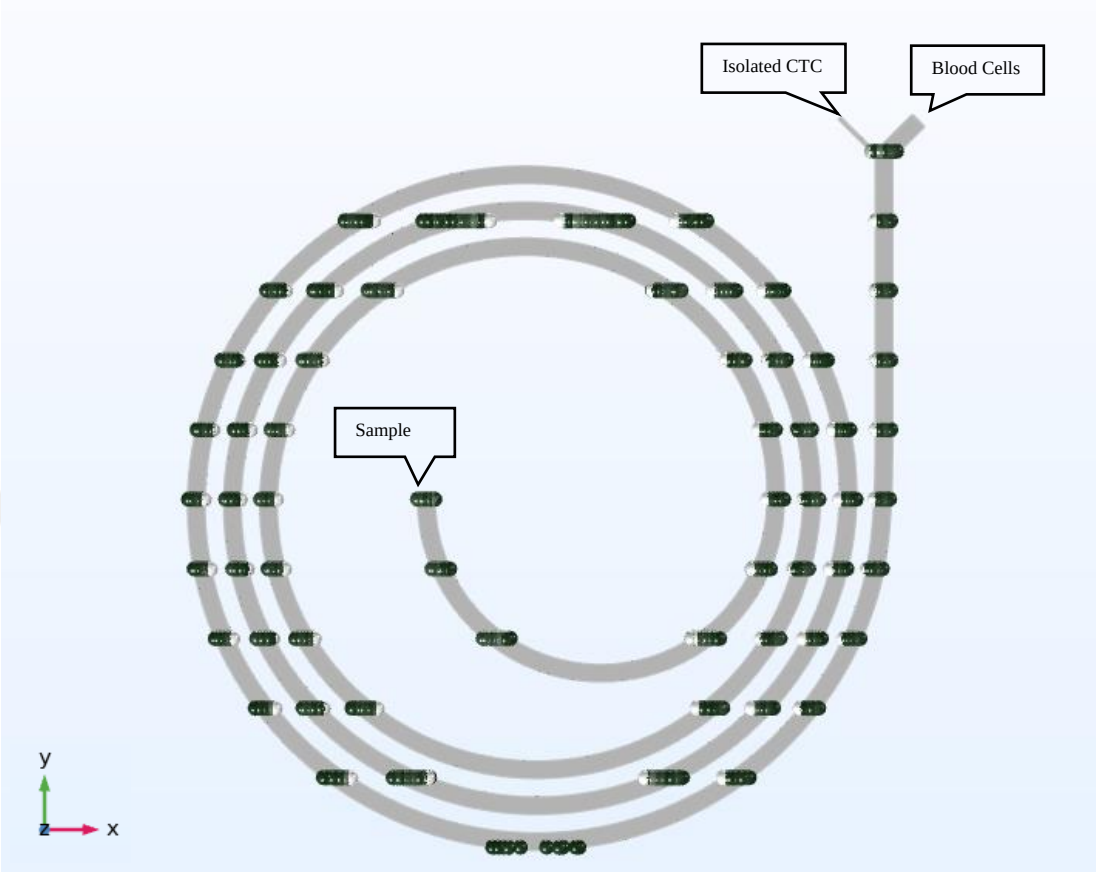

Figure 4.18: View of the particles from the top surface of the chip_9. The particles located on the cutting planes determined with 2000 μm intervals on the x-axis and y-axis, which represent the width and height of the channel, respectively.11different sized particles, two particles for each different sized CTC, and 20 particles for each different sized blood cells (a total of 148 particles) were simulated. White particles represent the CTCs (40, 35, 30, 25 μm); dark green particles represent blood cells (15, 10, 8, 7, 6, 3, 1 μm). The flow velocity for inlet, 0.47 m/s, so flow rate for inlet, 2.115 ml/min. The simulated channel Reynolds number, 108.46.

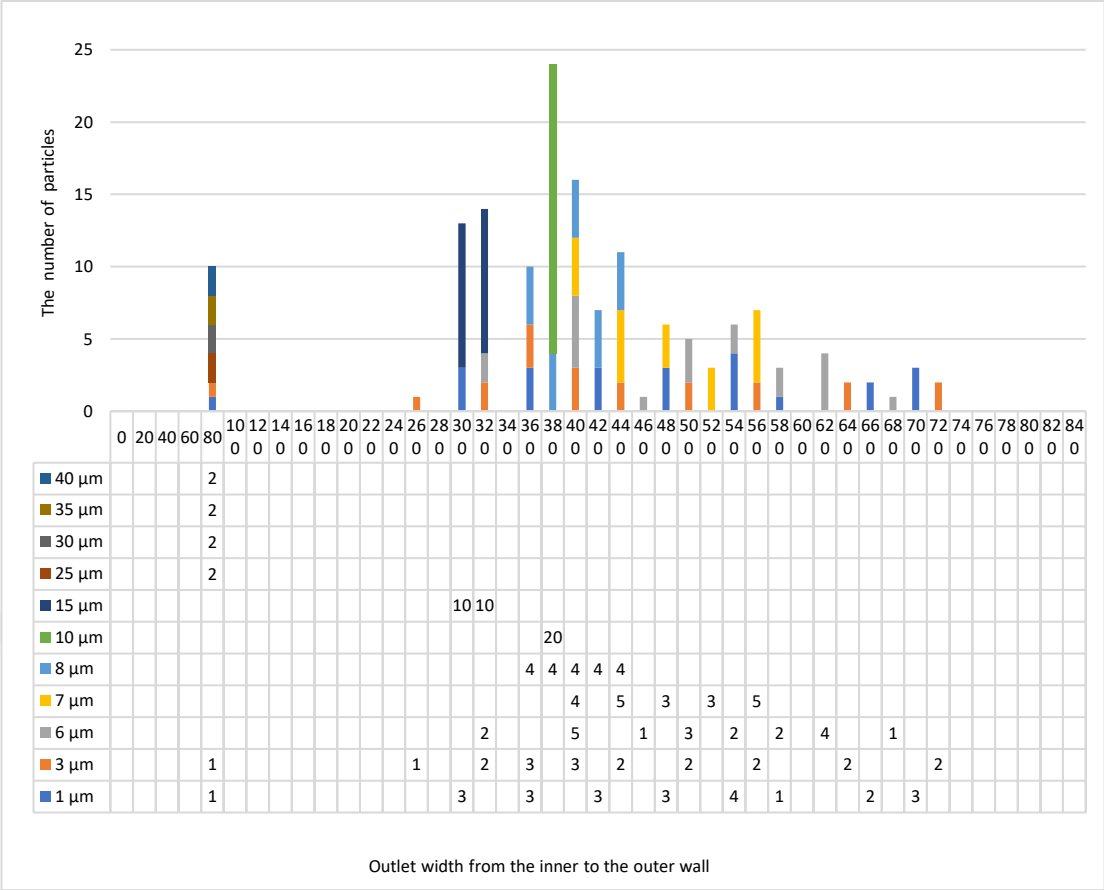

Figure 4.19: Particle distribution at the outlet in the width direction for the spiral channel, with Reynolds number 108.46

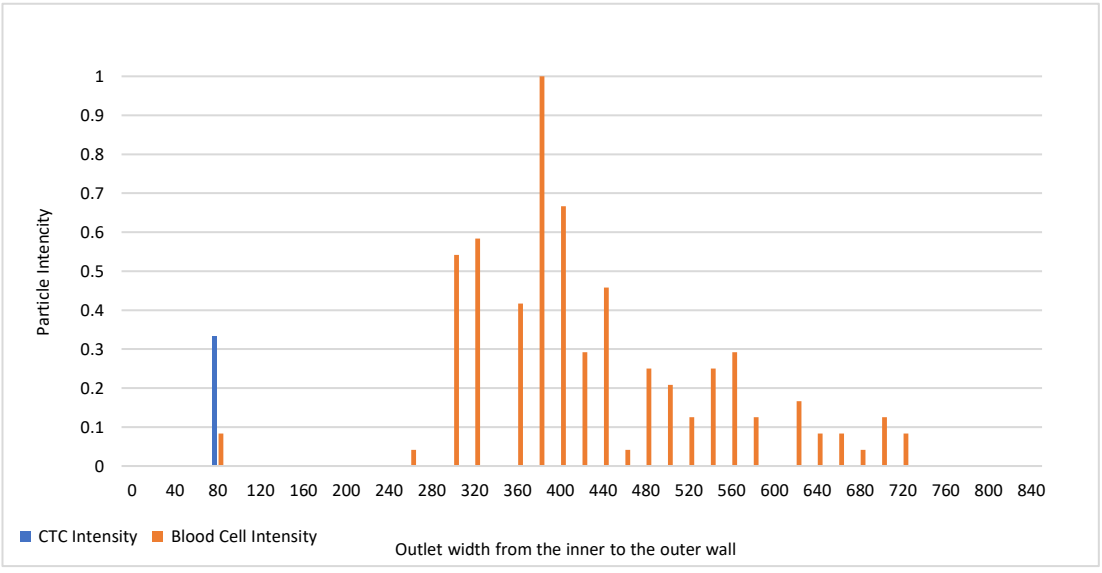

Figure 4.20: Column-scan is indicating the normalized distribution of CTCs and Blood cells at the outlet for the spiral channel, with Reynolds number 108.46.

This simulation was made to observe the effect of the Reynolds number, which is higher than others, on particle separation in channels without sheath flow. The channel length required for particle separation decreases when the Reynolds number is increased, as seen in previous simulations. However, in this simulation, although we increased the Reynolds number from 64.13 to 108.13, the reason for keeping the channel length constant is to leave the particles with the diameter of 1 and 3 microns for a longer time to ensure that these particles head towards the second outlet of the channel as shown in figure 4.18. The time we assigned to the program was 2.4 seconds. The particle number come out from outlets remained the same after the 0.94th second.

In the previous simulation, we observed that particles with a diameter of 40, 35, 30, and 25 microns focus on the x-axis on two parallel points when the inlet velocity is 0.3 m/s. However, in this simulation, we defined the inlet velocity to 0.47 m/s; these particles focused as scattered, as shown in figure 4.19. Also, the particles with a diameter of 15 microns were scattered in a particular area. Therefore, we can say that the Reynolds number approaching 110 reduces particle focusing and clustering. In all simulations without sheath flow, all particles except for 1-micron diameter particles were lined up on two lines along the x-axis due to the vertical channel cross-section.

In this simulation, we achieved our purpose and distinguished CTCs from blood cells except for some 1-micron particles. According to figure 4.20, even if blood cells with one micron in diameter, which are two in total, decrease their purity in the area where cancer cells are collected, they will not prevent the appearance of cancer cells.

To be compared all simulations with each other, the required channel length and simulation time for each chip, separation efficiency, and CTC and blood cell purity in the outlets of the chips were explained, respectively. The simulation pieces of information of each chip were given on the x-axis of the graphs as grouped. There were used six different chips. Three of them contain sheath flow (Chip_4, flow rate: 0.256, Re:13,13; Chip_5, flow rate: 0.765, Re: 39,23; Chip_6, flow rate: 2.115, Re: 108.46) other three (Chip_7, flow rate: 0.256, Re:13,13; Chip_8, flow rate:1.35, Re: 69,23; Chip_9, flow rate: 2.115, Re: 108.46) .

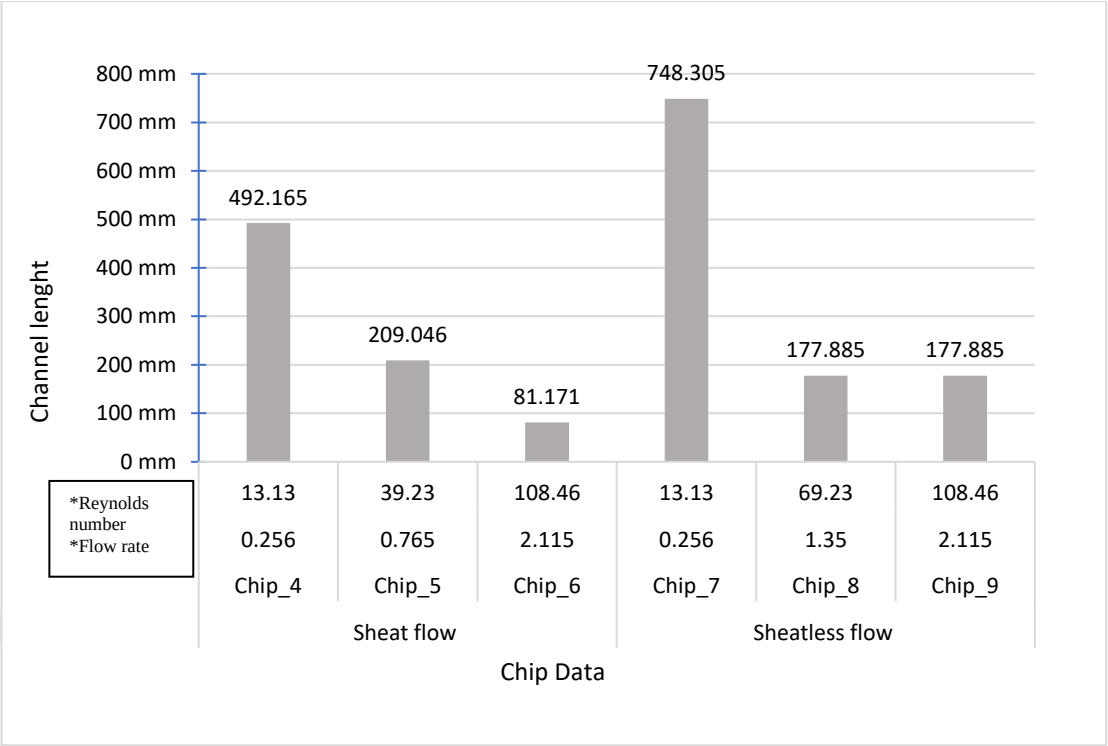

Figure 4.21: The figure shows the required channel length for each spiral chip.

Increasing the Reynolds number in the simulation resulted both in decreasing the channel length required for the particles to focus, as shown in figure 4.21. As can be seen on the graph, the channel lengths of the chip_8 and chip_9 have the same. If we kept the channel length in chip_9, half the length of the one given here, we were able to distinguish cancer cells. However, in such a case, some particles with a diameter of 1-micron came out of the outlet_1 with cancer cells.

In order to prevent this situation, we left the channel in the given length. Therefore, we directed some of the 1-micron diameter particles to outlet_2 together with the blood cells. Thus, we have increased the purity of isolated cancer cells. Since the drag force acting on particles with a diameter of 1 micron is quite small, it was insufficient to direct these particles alone. Particles with a diameter of 1-micron are the most affected by sheath flow pushing because of their small diameter. They could not resist the sheath flow and directed quickly.

The particles with a diameter of 1 micron are easily removed from the first outlet with the effect of sheath flow. Therefore, we did not need to increase the channel length

to separate them from cancer cells. Thus, in simulations involving sheath flow, the channel length required decreased as the channel's Reynolds number increased.

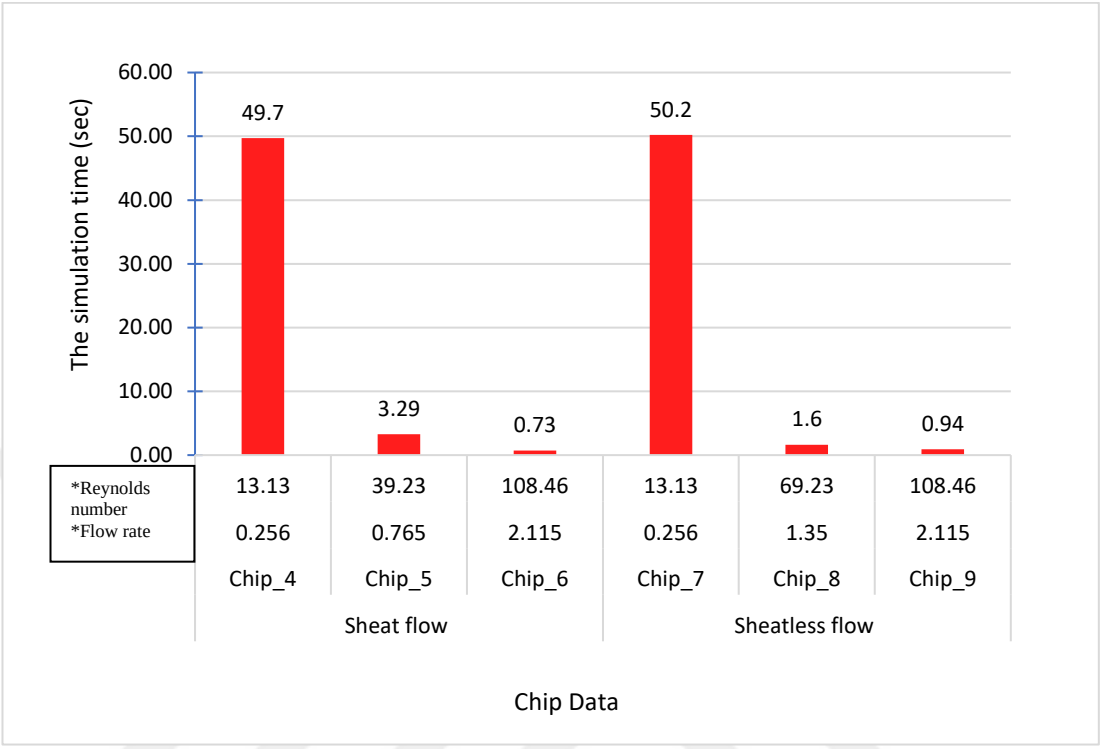

Figure 4.22: The figure shows the required time for particle separation.

As expected, the required time for separation decreased when the channel Reynolds number increased, and channel length decreased as shown in figure 4.22. Among six chips, the chip that performs the fastest simulation is chip_8 with 0.73 seconds. The slowest simulation is chip_7 with 50.2 seconds. There is no indication of whether sheath flow has any effect on the time taken for the simulation.

We calculated the separation efficiency of each chip and compared with each other to find the most productive chip. While finding the separation efficiency, we proportioned the CTCs emerging from the outlet_1 to the number of cancer cells injected at the inlet of the canal. Likewise, we proportioned the number of blood cells that appeared at outlet_1 to the number of cancer cells used at the inlet. Moreover, we subtracted the proportion of cancer cells from the proportion of blood cells.

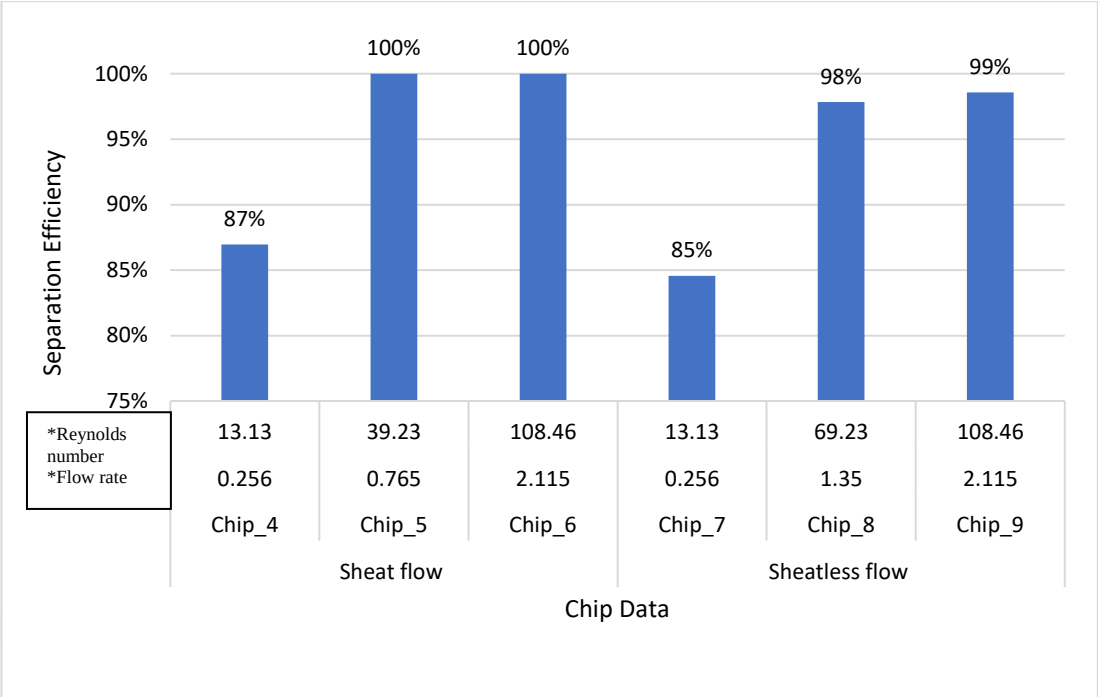

Figure 4.23: The figure shows the separation efficiency of each spiral chip.

To evaluate the results, we defined a separation efficiency for the separation of two species and applied to the measurements of the particle positions in the channel outlet dor each chip, as shown in figure 4.23. The separation efficiency is based on the maximum concentration achievable by both CTCs and blood cells in the channel. Since our goal is to distinguish CTCs, to calculate CTC separation efficiency of the simulations, firstly, we measured the ratio of cancer cells found at outlet 1 to the cancer cells collected from two outlets. Secondly, we measured the ratio of blood cells from outlet_1 to blood cells collected from two outlets. Since the aim was to find the separation efficiency of cancer cells, we found the separation efficiency by subtracting the ratio of blood cells from the ratio of CTCs.

When we looked at chip_4 and chip_7, 15-micron diameter particles moving with the 25-micron particles to the outlet_1 and decreased the separation efficiency. The use of low Reynolds in our simulations increased the focusing amount of the small particles. For this reason, the low Reynolds number is not recommended in order to separate our target cells. If we compare chip_4 and chip_7, we observe that Chip_4's efficiency is high in the field. In Chip_5 and Chip_6, we observe that no blood cells have been collected from outlet_1. This situation ensures that the purity is 100% in the

simulation on these chips. On the chip_8, together with the cancer cells, one is 1 micron in diameter, and 2 is 3 micron in diameter particles came out from outlet_1; On the chip_9, together with the cancer cells, one is 1 micron in diameter, and 1 is 3 micron in diameter came out to outlet_2. This situation decreased separation efficiency. However, in practice, these particles will not prevent the detection of CTCs because their diameter is tiny compared to cancer cells.

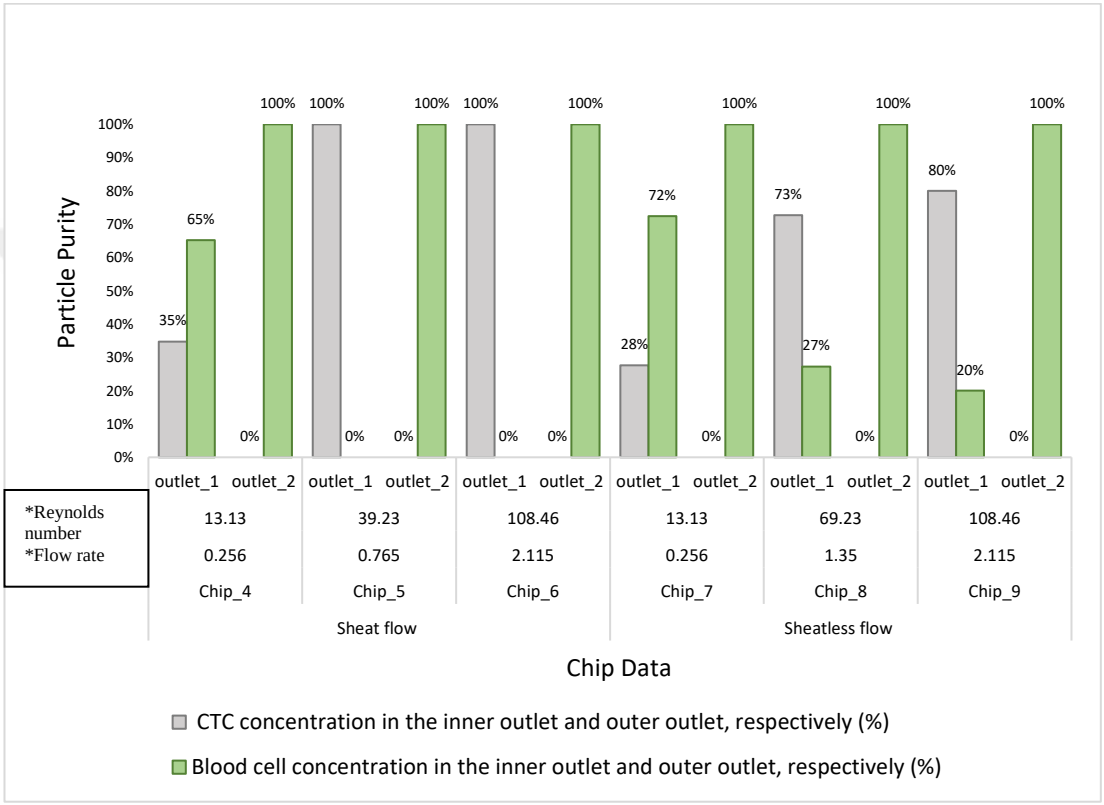

Figure 4.24: The figure shows the concentration of cell kinds collected at channel outlets for each chip, respectively.

As shown in figure 4.24, the particle collection purity of the chip_5 and chip_6 is 100%. That shows, these chips can use to the detection of CTCs. We observe that one and -micron diameter two or three blood cells in chip_8 and chip_9 reduce the purity of cancer cells with 8 in total in the outlet_1. However, this will not prevent the cancer cells from being seen due to the small diameter of the cells. Thus, these chips can also be used for cancer cell detection. The particles representing white blood cells with a diameter of 15 microns move together with the cells with a diameter of 25 microns in the chip_4 and chip_7. This situation has made the purity of the blood cells

at outlet_1 decreased, and the detection of cancer cells difficult. When we look at the outlet_2 of spiral simulations, we observe that the purity rates of blood cells are 100%. That is crucial for the detection of cancer cells in a person's blood because the loss of one cancer cell will cause the patient to be misdiagnosed.

In several chips to separate target particles, the same molecules, binding to targets, were used on the surface of the chip [Khalili et al., 2015], [Zhao et al., 2014],[Chen P., Huang Y.-Y., Bhave G., Hoshino K., 2017]. Especially anti-EpCAM antibody-coated micropillars were used because of most of the cancer cells bind EpCAM [Ahmed et al., 2017]. Therefore, it is highly selective, but since not all cancer cells have an affinity for the EpCAM molecule of the surface proteins when the target change binding molecules have to be changed to. Since we wanted to produce a chip with automation, we targeted a chip that separates the spiral channels and the target cells with inertial forces. That chip should be optimized for all CTCs. In some produced chips, it was aimed to separate the cells from each other by using filters [Cui et al., 2017], [Chen et al., 2017]. However, we did not use any filter in our chips due to the possibility of blockage in the filters.

Several types of spiral channel-shaped microdevices were designed, and particle trajectories were simulated in order to examine the influence of microchannel geometry on separation performance in both straight and spiral channels. According to the literature and mathematical calculations, when the particle size increases, the particle focusing ability increases under the influence of inertia forces. Therefore, we can say that larger particles focus in a shorter time than smaller particles.

The Dean drag force can separate particles that do not focus from those that are large enough to experience a significant inertial effect or vice versa. In this study, the separation of different particles from each other was observed using low Reynolds numbers. After usage of the effect of inertial forces in recent studies for particle tracing, there is a trend toward developing practical, single-use, user-independent analysis instruments in disease diagnosis.

In this thesis, a couple of devices was simulated by using COMSOL to observe the already existing microfluidic platforms, which use inertial forces to separate CTCs. Also, the platforms were developed and compared with each other according to their separation efficiency. While designing the geometry of the chips, specific parameters

were taken into consideration. For instance, the channel aspect ratio and vertical cross-sections of the channel affect the positioning of the particles along the channel [Di Carlo, 2009]. Many studies have been published concerning particle dynamics in straight and curved channels with circular and rectangular cross-sections, and attempts have been made at capturing the lift forces in mathematical expressions [Harouakaa et al., 2015], [Chen, 2018]. These expressions typically involve regression coefficients that depend on the velocity of the fluid and the sizes of the specific channel and particles.

Straight-rectangular-channel inertial microfluidics can be used to study particle migration dynamics directly because of its simple structure, and gradually form the basis of the other channel. However, since the length of the channel is long, it is not conducive to miniaturization or integration, which limits its further commercial applications. In this work, square and rectangular cross-section channels are used than particle movement is observed in those channels.

The results show that the CTCs and blood cells were successfully separated from each other using the spiral design. As the CTCs, which are our target cells, are more extensive than blood cells, we designed the geometry of the channel in such a way that the cells will be arranged in the channel in the order of size by using the principle that the inertial forces will affect cancer cells more than the blood cells and give a chance to occur the separation. By making the geometry of the vertical section of the channel rectangular, we have created a wider area for the arraying of cells. By making the channel's inlets closer to the center of the chip, we facilitated the introduction of cells into the channel in practice. We used a half-circular channel at the chip entrance to deliver the particles to the channel near the center of the chip. We used the Archimed spiral to design the central part of the channel. It provided great convenience in optimizing spiral channel geometry. It was the spiral channel that increased the effect of the drag force that provided particle separation.

In the simulations containing sheath flow, we determined the angle of the inlets with the y-axis as 30 degrees. If we had reduced the value of the angle, it would cause to reduce the effect of sheath flow so that it would be insufficient to direct cells. If we had increased the value of the angle, this would eliminate the discrimination of the cells, and also this would allow further mixing.

During the optimization, when we dropped the flow rate in the inlet, the particles required more extended channels to reach equilibrium positions. That means the drag force required for the particles to reach equilibrium had to be at a certain level. When we decreased the flow rate in a spiral channel where the channel length is constant, the drag force affecting the particles decreased as expected. Because of that reason, the particles came out of the channel before they reach the equilibrium position and separate from each other according to their size. When we decreased the flow rate, we increased the length of the channel and increased the duration of the drag force acting on the particles. As soon as the particles reached the distance to separate, we did not extend the length of the channel anymore.

In the simulations, we aimed to achieve the most realistic results, especially by selecting the random option as the entry location of the particles, and by defining 148 particles into the channel at the same time. We have kept some parameters like the cross-sectional area of the channel, inlets, and outlets for the simulations. However, other parameters were arranged and optimized, such as flow rate, channel length.

We produced a powerful method that could serve as a low-cost, technologically simple separation technique. We not only achieved the separation of particles but also analyzed the particle sorting and tracked the particle behaviors according to the flow changes too.

Until today, many studies have been conducted on particle tracking and separation [Rasooli, 2017]. However, comparative studies are still required to understand the mechanism. Thus, we tried to contribute to the shortcomings in the literature by comparing sheath flow simulations with sheathless flow simulations.

As shown, the proposed design is flexible and is capable of separating particulate mixtures over a wide dynamic range, and the separation process is based on the particle size. We predict it can be used a variety of environmental, medical, or manufacturing applications that involve rapid, low-cost, continuous separation of microparticles in real samples with a wide range of particle components.

5. CONCLUSION

Due to the importance of CTCs isolation and retrieval for early cancer diagnosis, we compared the microfluidic methods for CTCs isolation in the literature this thesis, fluid flow modeling, and particle tracing performed inside the microchannels. As the first part of the thesis, the simulation and modeling of particle focusing were carried out using inertial microfluidics for both straight and spiral microchannels. In inertial microfluidics, due to the presence of inertial lift forces at the lateral direction of the channel, randomly distributed particles at the inlet of the channel hold on to several equilibrium positions, which is known as the inertial migration in time.

The forces acting on the particles in a given simulation are proportional to the diameter of the particles. That means that large particles are subjected to greater inertial force. Therefore, it follows a parabolic streamline along the channel and reaches the equilibrium position quickly. However, since the inertial force acting on small particles in the same simulation is too small to move them in the vertical plane of the channel, the small particles follow almost linear streamlines. They need much longer channels and much more time to reach their balanced positions.

By using the particle tracing module in COMSOL multiphysics software, several simulations were conducted to observe particle motion in the straight channel and to separate different sized particles from each other in the spiral channel. We have investigated the effects of sheath flow, aspect ratio, flow rate, Reynolds numbers on cell capturing within microfluidic devices. This work provides several prototypes and useful guidelines for those designing and fabricating microfluidic devices for cell studies.

The straight channels are used to observe lateral migration of particles. The simulations of the straight channels, having different aspect ratios, were used to decide the spiral channel aspect ratio. The aspect ratio of the channel effect the focusing points of the particles in the outlet. The inertial forces effect was used to separate different sized particles without any external force. The aspect ratio has a significant effect on directing inertial forces. The straight channel simulations are the first step to defining the spiral channel aspect ratio. The Channel aspect ratio is optimized by using straight channels designing channel geometry.

The curved microchannel simulations, due to the introduction of channel curvature, secondary drag force effects will come into the account. The drag force on the lateral direction causes the velocity mismatches for the fluid elements in the vicinity. Therefore, Dean flow occurs, and the velocity of the fluid elements differentiates through the inner and outer walls of the channel. Dean flow changes the equilibrium positions of particle obtained in the straight channels. It has a significant role in size-based particle separation in this thesis. Under the inertial lift forces, the velocity with which the particles were observed to migrate to equilibrium positions increased with increasing particle diameter and increasing fluid flow rate. The particles reached their equilibrium positions in a shorter time with increasing velocity.

When the fluid's velocity is reduced, and the Reynolds number is approached to 1, the lift forces dominate the drag forces. The channel is perceived as close to the linear by the particles, albeit in a spiral shape. In such cases, the length of the channel required for separating the particles from each other increases. When the fluid's velocity is increased, and the Reynolds number is increased, drag forces dominate the lift forces. In such cases, it gets easy to separate the particles laterally. Thus, the length of the channel required for separating the particles from each other decreases.

Three straight channels, having different aspect ratios, were designed. Six different spiral channels were designed. Three of the spiral channels contain sheath flow; the other three do not. There different Reynolds numbers were used to observe the changing on the focusing streamline of particles. When the Reynolds number was closed to 120, particle focusing competency increased for more massive particles, representing CTCs. When the Reynolds number was closed to 10, particle focusing competency increased for less massive particles, representing blood cells. We have performed the excretion of one hundred percent cancer cells from blood cells.

In the study, eleven different sized neutrally buoyant spherical particles were used to represent the cells. That has been fairly helpful in accurately determining the length of the channel required for particle separation to occur. Using many pieces of different sizes in simulations was made to try to get the most realistic results by considering the cells in a blood sample. The simulations show the system would be clinically useful for preparative separation of large volumes of blood or emulsions in a compact format.

In this thesis, any external force was not used, but it is possible to separate particles by using electrical or magnetic forces. As future research for these topics, the chips can design again to detect a different kind of CTC, bacteria, or yeast in microscale, but also for several viruses in nanoscale. Recently by using visco-elastic non-Newtonian fluids, separation the nano-particles in microchannels has been succeeded. The made simulations can be used to predict the behavior of particles in microfluidic devices, which would aid in separating different sized particles.

REFERENCES

Ahmed M. G., Abate M. F., Song Y., Zhu Z., Yan F., Xu Y., Wang X., Li Q., Yang C., (2017), "Isolation, detection, and antigen-based profiling of circulating tumor cells using a size-dictated immunocapture chip.", Angewandte Chemie International Edition, 56(36), 10681–10685.

Al-Faqheri W., Thio T. H. G., Qasaimeh M. A., Dietzel A., Madou M., Al-Halhouli A., (2017), "Particle/cell separation on microfluidic platforms based on centrifugation effect: a review.", Microfluidics and Nanofluidics, 21(6), 1–23.

Antfolk M., Kim S. H., Koizumi S., Fujii T., Laurell T., (2017), "Label-free single-cell separation and imaging of cancer cells using an integrated microfluidic system.", Scientific Reports, 7, 46507.

Au S. H., Edd J., Haber D. A., Maheswaran S., Shannon L., Toner M., (2017), "Clusters of circulating tumor cells: a biophysical and technological perspective.", Current Opinion Biomedical Engineering, 3, 13-19.

Ault J. T., Chen K. K., Stone H. A., (2015), "Downstream decay of fully developed Dean flow.", Journal of Fluid Mechanics, 777, 219-244.

Bagchi P., Johnson P. C., Popel A. S., (2005), "Computational fluid dynamic simulation of aggregation of deformable cells in a shear flow.", Journal of Biomechanical Engineering, 127(7), 1070-1080.

Bhagat A. A. S., Kuntaegowdanahalli S. S., Papautsky I., (2008), "Continuous particle separation in spiral microchannels using Dean flows and differential migration.", Lab on a Chip, 8(11), 1906-1914.

Brody J. P., Yager P., Goldstein R. E., Austin R. H., (1996), "Biotechnology at low Reynolds numbers.", Biophysical Journal, 71(6), 3430-3441.

Bruus H., (2006), "Theoretical Microfluidics.", Second edition, Oxford: Oxford university press.

Burger R. Ducrée J., (2012), "Handling and analysis of cells and bioparticles on centrifugal microfluidic platforms.", Expert Review of Molecular Diagnostics, 12(4), 407-421.

Casavant B. P., Mosher R., Warrick J. W., Maccoux L. J., Berry S. M. F., Becker J. T., Chen V., Lang J., McNeel D., Beebe D. J., (2013), "A negative selection methodology using a microfluidic platform for the isolation and enumeration of circulating tumor cells.", Methods, 64(2), 137-143.

Che J., Yu V., Dhar M., Renier C., Matsumoto M., Heirich K., Garon E. B., Goldman J., Rao J., Sledge G. W., Pegram M. D., Sheth S., Jeffrey S. S., Kulkarni R. P., Sollier E., Carlo D. D., (2016), "Classification of large circulating tumor cells isolated with ultra-high throughput microfluidic vortex technology.", Oncotarget, 7(11), 12748–12760.

Chen H., (2018), "A triplet parallelizing spiral microfluidic chip for continuous separation of tumor cells.", Scientific Reports, 8(1), 1-8.

Chen H., Cao B., Sun B., Cao Y., Yang K., Lin Y. S., Chen H., (2017), “Highly-sensitive capture of circulating tumor cells using micro-ellipse filters.”, Scientific Reports, 7(1), 1-10.

Chen P., Huang Y. Y., Bhave G., Hoshino K., Zhang X., (2017), “Inkjet-print micromagnet array on glass slides for immunomagnetic enrichment of circulating tumor cells.”, Annals of Biomedical Engineering, 44(5), 1710-1720.

Convery N., Gadegaard N., (2019), “30 years of microfluidics.”, Micro and Nano Engineering, 2, 76-91.

Cui X., Guo W., Sun Y., Sun B., Hu S., Sun D., Lam R. H. W., (2017), “A microfluidic device for isolation and characterization of transendothelial migrating cancer cells.”, Biomicrofluidics, 11(1), 014105.

Dean L., (2005), Blood Groups and Red Cell Antigens, 2, Bethesda, Md, USA: NCBI.

Di Carlo D., Edd J. F., Humphry K. J., Stone H. A., Toner M., (2009), “Particle segregation and dynamics in confined flows.”, Physical Review Letters, 102(9), 094503.

Di Carlo D., Edd J. F., Irimia D., Tompkins R. G., Toner M., (2008), “Equilibrium separation and filtration of particles using differential inertial focusing.”, Analytical Chemistry, 80(6), 2204–2211.

Di Carlo D., Irimia D., Tompkins R. G., Toner M., (2007), “Continuous inertial focusing, ordering, and separation of particles in microchannels.”, Proceedings of the National Academy of Sciences, 104(48), 18892–18897.

Dong Y., Skelley A. M., Merdek K. D., Sprott K. M., Jiang C., Pierceall W. E., Lin J., Stocum J., Carney W. P., Smirnov D. A., (2013), “Microfluidics and circulating tumor cells.”, Journal of Molecular Diagnostics, 15(2), 149-157.

Ekanayake N. I. K., Berry J. D., Stickland A. D., Muir I. L., Dower S. K., Harvie D. J. E., (2018), “Lift and Drag forces on a particle near a wall at low Reynolds numbers.”, 21st Australasian Fluid Mechanics Conference, 1-4, Adelaide, Australia, December.

Fuchs B. B., Eatemadpour S., Martel-Foley J. M., Stott S., Toner M., Mylonakis E., (2019), “Rapid isolation and concentration of pathogenic fungi using inertial focusing on a chip-based platform.”, Frontiers in Cellular and Infection Microbiology, 9(27), 1-9.

Gossett D. R., Carlo D. D., (2009), “Particle focusing mechanisms in curving confined flows.”, Analytical Chemistry, 81(20), 8459-8465.

Gou Y., Jia Y., Wang P., Sun C., (2018), “Progress of inertial microfluidics in principle and application.”, Sensors, 18(6), 1-26.

Gupta G. P., Massagué J., (2006), “Cancer Metastasis: Building a Framework.”, Cell, 127(4), 679–695.

Han X., Feng Y., Cao Q., Li L., (2015), “Three-dimensional analysis and enhancement of continuous magnetic separation of particles in microfluidics.”, Microfluidics and Nanofluidics, 18, 1209-1220.

Harouakaa R., Kang Z., Zheng S., Cao L., (2015), “Circulating tumor cells: advances in isolation and analysis, and challenges for clinical applications.”, Pharmacology & Therapeutics, 141(2), 209-221

Hong, Y., Fang, F., Zhang, Q, (2016), “Circulating tumor cell clusters: What we know and what we expect.”, International Journal of Oncology, 49(6), 2206-2216.

Hou H. W., Warkiani M. E., Khoo B. L., Li Z. R., Soo R. A., Tan D. S. W., Lim W. T., Han J., Bhagat A. A. S., Lim C. T., (2013), “Isolation and retrieval of circulating tumor cells using centrifugal forces.”, Scientific Reports, 3, 1259.

Hur S. C., Tse H. T. K., Di Carlo D., (2010), “Sheathless inertial cell ordering for extreme throughput flow cytometry.”, Lab on a Chip, 10(3), 274-280.

Jiang X., Wong K. H. K., Khankhel A. H., Zeinali M., Reategui E., Phillips M. J., Luo X., Aceto N., Fachin F., Hoang A. N., Kim W., Jensen A. E., Sequist L. V., Maheswaran S., Haber D. A., Stott S. L., Toner M., (2018), “Microfluidic isolation of platelet-covered circulating tumor cells.”, Lab on a Chip, 17(20), 3498–3503.

Karabacak N. M., Spuhler P. S., Fachin F., Lim E. J., Pai, V., Ozkumur E., Martel J. M., Kojic N., Smith K., Chen P., Yang J., Hwang H., Morgan B., Trautwein J., Barber T., Stott S. L., Maheswaran S., Kapur R., Haber D. A., Toner M., (2014). “Microfluidic, marker-free isolation of circulating tumor cells from blood samples.”, Nature Protocols, 9(3), 694-710.

Karnis A, Goldsmith H, Mason S., (1966), “The flow of suspensions through tubes: V. Inertial effects.”, Canadian Journal of Chemical Engineering, 44(4), 181-193.

Khademhosseini A., Yeh J., Eng G., Karp J., Kaji H., Borenstein J., Farokhzad O. C., Langer R., (2005), “Cell docking inside microwells within reversibly sealed microfluidic channels for fabricating multiphenotype cell arrays.”, Lab on a Chip, 5(12), 1380–1386.

Khalili A. A., Ahmad M. R., (2015), “A Review of cell adhesion studies for biomedical and biological applications.”, International Journal of Molecular Sciences, 16(8), 18149-18184.

Khoo B. L., Warkiani M. E., Tan D. S. W., Bhagat A. A. S., Irwin D., Lau D. P., Lim A. S. T., Lim K. H., Krisna S. S., Lim W. T., Yap Y. S., Lee S. C., Soo R. A., Han J., Lim C. T., (2014), “Clinical validation of an ultra high-throughput spiral microfluidics for the detection and enrichment of viable circulating tumor cells.”, PLoS ONE, 9(7), e99409.

Kuntaegowdanahalli S. S., Bhagat A. A. S. Kumar G., Papautsky I., (2009), “Inertial microfluidics for continuous particle separation in spiral microchannels.”, Lab on a Chip, 9(20), 2973-2980.

Lim E. J., Ober T. J., Edd J. F., Mckinley H., Toner M., (2012), “Visualization of microscale particle focusing in diluted and whole blood using particle trajectory analysis.”, Lab on a Chip, 12(12), 2199-2210.

Liu C., Xue C., Sun J., Hu G., (2016), “A generalized formula for inertial lift on a sphere in microchannels.”, Lab on a Chip, 16(5), 884-892.

Martel J. M., Toner M., (2014), “Inertial focusing in microfluidics.”, Annual Review of Biomedical Engineering, 16, 371-396.

Norouzi M., Sedaghat M. H., Shahmardan M. M., (2014), “An analytical solution for viscoelastic Dean flow in curved pipes with elliptical cross section.”, Journal of Non-Newtonian Fluid Mechanics, 204, 62-71.

Page K., Graham E. A., (2008), “Cancer and forensic microsatellites.”, Forensic Science, Medicine, and Pathology, 4(1), 60-66.

Papanastasiou T. C., Georgiou G. C., Alexandrou. A. N., (2000), “Viscous fluid flow.”, CRC Press.

Park J. M., Kim M. S., Moon H. S., Yoo C. E., Park D., Kim Y. J., Han K.Y., Lee J. Y., Oh J. H., Kim S. S., Park W. Y., Lee W.Y., Hun N., (2014), “Fully automated circulating tumor cell isolation platform with large-volume capacity based on lab-on-a-disc.” Analytical Chemistry, 86(8), 3735-3742.

Park J. S., Song, S. H., Jung, H. I., (2009), “Continuous focusing of microparticles using inertial lift force and vorticity via multi-orifice microfluidic channels.” Lab on a Chip, 9(7), 939-948.

Parrott C., (2017), “Computational fluid dynamics (CFD) simulation of microfluidic focusing in a low-cost flow cytometer.”, Thesis of Honors Baccalaureate of Science, Oregon State University.

Pnueli D., Gutfinger C., Fichman M., (1997), “Shear induced lift in the motion of small particles in rotating flows.”, Journal of Aerosol Science, 28(8), 1507-1516.

Purcell E. M., (1977), “Life at low Reynolds number.”, American Journal of Physics, 45(1), 3-11.

Qin D., Xia Y., Rogers J.A., Jackman R.J., Zhao XM., Whitesides G.M., (1998), “Microfabrication, Microstructures and Microsystems.”, In Microsystem Technology in Chemistry and Life Science,194, 1-20.

Quake S. R., Squires T. M., (2005), “Microfluidics: Fluid physics at the nanoliter scale.”, Reviews of Modern Physics, 77(3), 977–1026.

Rasooli R., (2017), “Modeling of inertial particle flow and entry gas flow in micro-channels.”, Master’s Thesis, Bilkent University.

Reynolds, O., (1883), “Iii. An experimental investigation of the circumstances which determine whether the motion of water shall be direct or sinuous, and of the law of resistance in parallel channels.”, Philosophical Transactions of the Royal Society, 35(224-226), 84-99.

Saffman P. G., (1965), “The lift on a small sphere in a slow shear flow.”, Journal of Fluid Mechanics, 22(2), 385-400.

Salar S., Madou M. J., Kulinsky L., (2013), “Centrifugal microfluidics: characteristics & possibilities.”, Microfluidics and Microscale Transport Processes, 149-186.

Sarioglu A. F., Aceto N., Kojic N., Donaldson M. C., Hamza B., Engstrom A., Zhu H., Sundaresan T. K., Miyamoto D. T., Luo X., Bardia A., Wittner B.S., Ramaswamy S., Shioda T., Ting D. T., Stott S. L., Kapur R., Maheswaran S., Haber D. A., Toner M., (2016), “A microfluidic device for label-free, physical capture of circulating tumor cell-clusters.”, Nature Methods, 12(7), 685-691.

Segré G., Silberberg A, (1962), “Behaviour of macroscopic rigid spheres in Poiseuille flow: Part 2. Experimental results and interpretation.”, Journal of Fluid Mechanics, 14(1), 115-135.

Smith S., Mager, D., Perebikovsky A., Shamloo E., Kinahan D., Mishra R., Delgado S. M.T., Kido H., Saha S. Ducrêe J., Madou M., Land K., Korvink J.G., (2016), “CD-based microfluidics for primary care in extreme point-of-care settings.”, Micromachines, 7(2), 1-32.

Stokes, G. G., (1850), “On the effect of the internal friction of fluids on the motion of pendulums”, 9(8), Cambridge: Pitt Press.

Segré G., Silberberg A., (1961), “Radial Particle Displacements in Poiseuille Flow of Suspensions.”, Nature, 189(4760), 209-210.

Stone H. A., (2000), “Philip Saffman and viscous flow theory.”, Journal of Fluid Mechanics, 409, 165-183.

Sun J., Li, M., Liu C., Zhang Y., Liu D., Liu W., Hu G., Jiang X., (2012), “Double spiral microchannel for label-free tumor cell separation and enrichment.”, Lab on a Chip, 12(20), 3952-3960.

Thomas A. M., Fang J., Feng J., Bolotnov I. A., (2015), “Estimation of Shear-Induced Lift Force in Laminar and Turbulent Flows.”, Nuclear Technology, 190(3), 274-291.

Vona G., Sabile A., Louha M., Sitruk V., Romana S., Franco D., Schütze K., Capron F., Franco D., Pazzagli M., Vekemans M., Lacour B., Brêchot C., Brêchot P. P., (2000), “Isolation by size of epithelial tumor cells: a new method for the immunomorphological and molecular characterization of circulating tumor cells.”, American Journal of Pathology, 156(1), 57-63.

Warkiani M. E., Khoo, B. L., Wu, L., Tay, A. K. a. P., Bhagat, A. A. S., Han, J., Lim, C. T, (2016), “Ultra-fast, label-free isolation of circulating tumor cells from blood using spiral microfluidics.”, Nature Protocols, 11(1), 134-148.

Warkiani M. E., Tay A. K. P., Guan G., Han J., (2015), “Membrane-less microfiltration using inertial microfluidics.”, Scientific Reports, 5, 11018.

Winer M. H., Ahmadi A., Cheung K. C., (2014), “Application of a three-dimensional (3D) particle tracking method to microfluidic particle focusing.”, Lab on a Chip, 14(8), 1443-1451.

Yamada M., Nakashima M., and Seki M., (2004), “Pinched flow fractionation: continuous size separation of particles utilizing a laminar flow profile in a pinched microchannel.”, Analytical chemistry, 76(18), 5465–5471.

Yan S., (2016), “Tunable hydrophoresis for bio-particle focusing and separation using dielectrophoresis-assisted and magnetophoresis-assisted hybrid techniques.”, PhD Thesis, University of Wollongong.

Yoo C. E., Park J. M., Moon H. S., Joung J. G., Son D. S., Jeon H. J., Kim Y. J., Han K. Y., Sun J. M., Park K., Park D., Park W.Y., (2016), “Vertical magnetic separation of circulating tumor cells for somatic genomic-alteration analysis in lung cancer patients.”, Scientific Reports, 6(1), 1-11.

Zeng L., Najjar F., Balachandar S., Fischer P., (2009), “Forces on a finite-sized particle located close to a wall in a linear shear flow.”, Physics of Fluids, 21(3), 033302.

Zhang J., Yan S., Yuan D., Alici G., Nguyen N. T., Warkiani, M., E., Li, W., (2016), “Fundamentals and applications of inertial microfluidics: A review.”, Lab on a Chip, 16(1), 10-34.

Zhao L., Lu Y.-T., Li F., Wu K., Hou S., Yu J., Shen Q., Wu D., (2014), “High-purity prostate circulating tumor cell isolation by a polymer nanofiber-embedded microchip for whole exome sequencing.”, Advanced Materials, 25(21), 2897-2902.

Zhou J., Papautsky I. (2013), “Fundamentals of inertial focusing in microchannels.”, Lab on a Chip, 13(6), 1121-1132.

Zhou M., Zheng H., Wang Z., Li R., Liu X., Zhang W., Wang Z., Li H., Wei Z., Hu Z. (2017), “Precisely enumerating circulating tumor cells utilizing a multi-functional microfluidic chip and unique image interpretation algorithm.”, Theranostics, 7(19), 4710-4721.

BIOGRAPHY

Cigdem Boz was born in 1998 in Osmaniye. She completed his undergraduate education in Molecular Biology and Genetics at Gebze Technical University in 2017. She worked in the private sector for six months, and then she started her master's degree in Biotechnology Institute at Gebze Technical University in 2018. She has been doing modeling studies on the development of a microfluidic chip to separate circulating tumor cells from human blood under the supervision of Asst. Prof. Muhammed Enes Oruc.